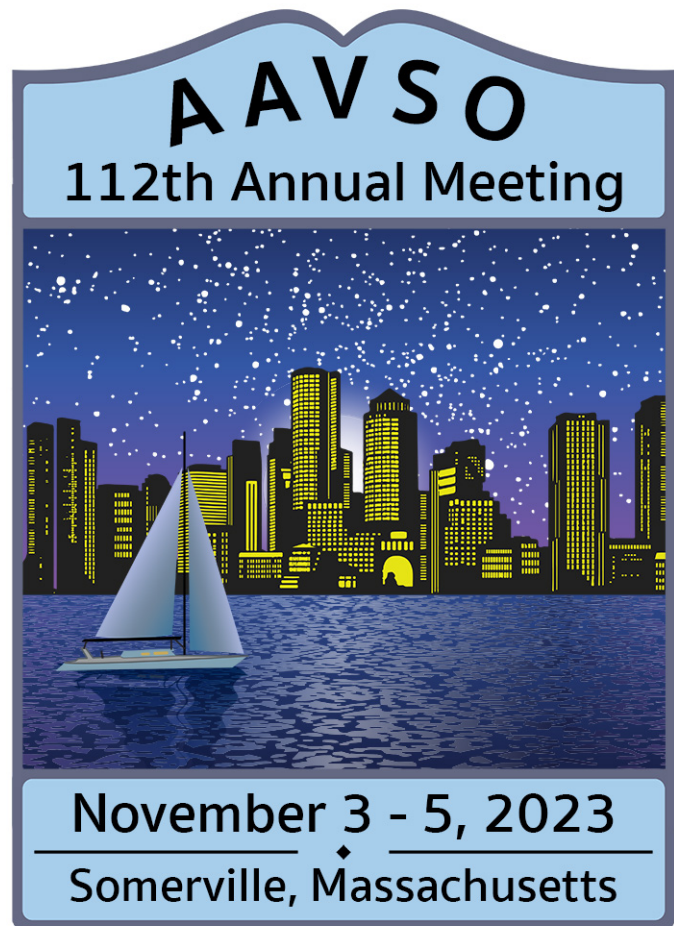


Proceedings of
the 112th Annual
Meeting of

The American
Association of
Variable Star
Observers



December 2023

ISBN 978-1-939538-68-0



Proceedings of the AAVSO 112th Annual Meeting

Editor

Joyce A. Guzik

Los Alamos National Laboratory

Los Alamos, NM 87545, USA

Disclaimer

The acceptance of a paper for the Proceedings of the American Association of Variable Star Observers does not imply nor should it be inferred as an endorsement by the AAVSO of any product, service, method, or results mentioned in the paper. The opinions expressed are those of the authors and may not reflect those of the AAVSO, its members, or meeting sponsors.



© 2024 The American Association of Variable Star Observers. All rights reserved.

The American Association of Variable Star Observers
185 Alewife Brook Parkway, Suite 410, Cambridge, MA 02138, USA

Proceedings of the AAVSO 112th Annual Meeting

Editor's Note

This collection of articles was submitted as optional conference proceedings papers by participants of the 112th Annual AAVSO meeting held November 3-5, 2023, at the Row Hotel in Somerville, Massachusetts.

Seventeen articles were received, representing invited keynote, contributed oral, and poster presentations. These articles have remarkable variety of content and are not necessarily the type of articles that would be found in standard astrophysical research journals.

These articles have been edited/curated, but not peer reviewed. Extended abstracts were reviewed by a committee with members Joyce Guzik (chair), Tom Maccarone, Sebastián Otero, and Elizabeth Waagen before being accepted for presentation at the meeting.

The full meeting schedule with links to abstracts can be found at <https://www.aavso.org/112>.



*AAVSO 112th Annual Meeting Group
Photo Credit: Robert Stephens*

Proceedings of the AAVSO 112th Annual Meeting

Table of Contents

Evidence of CO Destruction in Classical Cepheid CP Cephei <i>Scott G. Call, Eric G. Hintz, Steve Ardern, Victoria Scowcroft, Timothy D. Morrell</i>	7
Data Quality Task Force Synopsis <i>Matt Craig and Mark Munkacsy</i>	11
Nights on Fire: The Extent of Smoke over North America in Summer 2023 <i>Matthew Craig</i>	27
Spectroscopy of “Be” Stars Exhibiting Rapid Variability: A Preliminary Report <i>Harry R. (Rick) Diz, N. de Hilster, J. B. Desrosiers, S. Diaz Lopez, M. Di Lazzaro, J. Elias Cantalapiedra, G. Gebhard, M. Larsson, J. Martin, G. Piehler</i>	32
Abrupt Periodic Pulsation Resumptions in Deneb <i>Joyce A. Guzik, Helmut A. Abt, Jason Jackiewicz, Brian Kloppenborg</i>	38
Finding Cool Companions to Pulsating Variable Stars with Infrared Spectroscopy <i>Eric G. Hintz, Scott G. Call, Timothy D. Morrell</i>	48
Using Photometric Imaging to Observe Variable Sources and Confirm Exoplanet Candidates <i>Hafsa Jamil, Michael Joner, Oliver Hancock</i>	56

Proceedings of the AAVSO 112th Annual Meeting

Cooperative Observing at a Modest-Sized Observatory <i>Michael D. Joner, Denzil E. Watts IV, Seneca H. Bahr, Oliver Hancock, Michael W. Holland, Hafsa Jamil, Eden Saxton, Malaya Williams-Jones</i>	68
Blame it on Aquila: Fictional and Factual Novae <i>Kristine Larsen</i>	85
Modelling Pulsating Stars <i>Philip Masding and Robin Leadbeater</i>	92
Period Change Updates for δ Scuti Variable DY Her <i>Abigale Moen, Matthew Craig, Emily Watson, Tanner Weyer</i>	102
Developing Algorithms to Determine an Asteroid's Physical Properties and the Success of Deflection Missions <i>Arushi Nath</i>	109
“Long Secondary Period (LSP) Stars” and the LSP Phenomenon <i>John Percy, Mayank H. Shenoy, Sandra Zhitkova</i>	127
Variable Stars in the Cepheus Flare Region <i>Michael Poxon</i>	133
Imaging Stars with the CHARA Array <i>Gail H. Schaefer</i>	139
Analysis of the Blazhko Effect in the Star EY UMa <i>Emily Watson, Dr. Matthew Craig, Tanner Weyer, Abigale Moen</i>	146

Proceedings of the AAVSO 112th Annual Meeting

An Unfortunately Constant Star Field

152

*Tanner Weyer, Dr. Matthew Craig, Mara DeRung,
Emily Watson, Abigale Moen*

Evidence of CO Destruction in Classical Cepheid CP Cephei

Scott G. Call¹, Eric G. Hintz¹, Steve Ardern², Victoria Scowcroft²,
and Timothy D. Morrell¹

¹Brigham Young University, Department of Physics & Astronomy, Provo, Utah, 84602, USA;
scall93@student.byu.edu

²University of Bath, Department of Physics, Claverton Down, Bath, BA2 7AY, UK

Subject Keywords

Techniques: spectroscopic; stars: variable: Cepheids; infrared: stars; stars: individual (CP Cep)

Abstract

Cepheid variables play a crucial role in the bottom rung of the distance ladder, which defines distance measurements in astronomy. Therefore, any uncertainties in Cepheid measurements have the potential to propagate upwards in the distance ladder, affecting higher-level measurements such as the Hubble constant.

Metallicity is expected to affect the sensitivity of the period-luminosity relation. Recently, carbon monoxide (CO) has been observed in a few classical Cepheids. The CO forms in these atmospheres near minimum light and subsequently is destroyed as temperatures rise. This behavior leads to changes in the near and mid-infrared wavelengths corresponding to CO and will influence the period-luminosity relation.

We conducted observations of the classical Cepheid, CP Cep, utilizing the ARC 3.5m telescope at Apache Point Observatory and the near-infrared spectrograph, *TripleSpec*. The initial observations detected strong CO absorption bands, while follow-up observations on the subsequent night revealed a reduction in CO absorption, suggesting the destruction of CO molecules. Exploring how metallicity factors into period-luminosity relations for Cepheids may enhance the precision of distance measurements and mitigate the discrepancy of Hubble constant measurements.

1. Introduction

The “distance ladders” are the paths by which distances are measured in the known universe. They begin with nearby pulsating stars such as RR Lyrae or Cepheid type, which have relations between period and luminosity. Henrietta Leavitt originally found this relationship for Cepheid variables, and the Leavitt Law has been used as the Population I distance ladder bottom rung since (Leavitt & Pickering 1912). Understanding these objects is crucial to making sure uncertainties in distance measurements are not propagated up the ladder.

Recently, carbon monoxide (CO) has been shown to change in the supergiant Cepheid atmospheres as the star pulsates. This was first reported by Marengo et al. (2010), where *Spitzer* observations of Cepheids at single phases showed large scatter in the 4.5 μm filter due to a CO absorption feature. Scowcroft et al. (2016) later presented mid-infrared photometry from *Warm Spitzer* for many Cepheids over full periods, which confirmed that CO changed with pulsation but only affected the 4.5 μm filter bandpass. More recently, Hamer et al. (2023) detected CO in the radio regime for a few Cepheids, although only at single phase points.

The CO forms in the extended atmospheres when the temperatures are cool and is subsequently destroyed as the star compresses and heats up. The change in opacity greatly affects measurements at 4.5 μm , but the effects in other parts of the electromagnetic spectrum have not been studied. In addition to features in the radio and mid-infrared, there is a CO feature present in the near-infrared (NIR) on the edge of what is known as the *K*-band. This research focuses on that feature for one Cepheid.

CP Cephei (hereafter CP Cep) is a classical Cepheid variable with a *V* magnitude of 10.58. It has a period of 17.867 days, and is known as a bump Cepheid where there is a small bump on the ascending portion of the light curve in *V*. We chose CP Cep as a potential candidate to see CO due to Hamer et al. (2023) observing CO in the radio.

2. Observations and Results

2.1 Observations

NIR spectral observations were taken using the Astrophysical Research Consortium (ARC) 3.5-m telescope at Apache Point Observatory in New Mexico. The NIR spectrograph, *TripleSpec*, was used to obtain spectra between 0.95-2.46 μm at a resolution $R=3500$ (Wilson et al. 2004). CP Cep was observed on July 4th, 5th, and August 27th (UTC) using this system. Exposure times were either 25 or 30 seconds, with the star being dithered on the slit between two positions. This dithering allows for the subtraction of emission lines and thermal background due to Earth's atmosphere. A nearby standard star was also observed at similar airmass for calibration and correction of atmospheric absorption.

Sky conditions for each night were clear or mostly clear, with the possibility of thin, high clouds that may reduce the quality of the data. The context of the observations is shown in Figure 1. The first observation was just after the bump on the ascending portion of the phased light curve (in *V*), the second was more on the ascending part toward maximum, and the third observation was very close in phase to the first night.

Reduction of the NIR spectra was performed using a modified version of *Spextool*, the details of which are found in Cushing et al. (2004) and Vacca et al. (2003). This package includes tools for spectral extraction and correction of atmospheric effects.

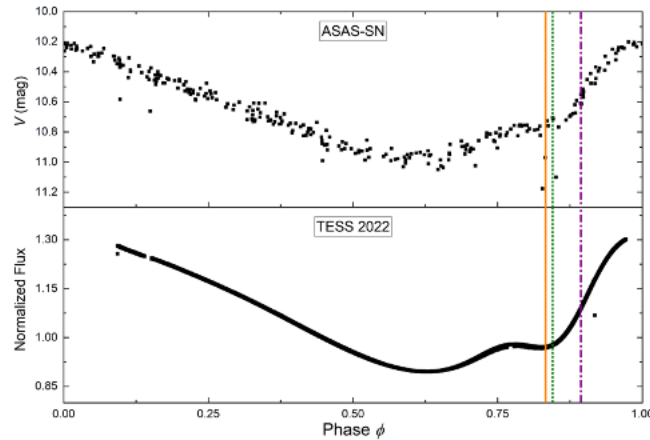


Figure 1. Phased light curves for CP Cep from ASAS-SN and TESS. Observations are shown as the vertical lines with July 4th – orange solid, July 5th – purple dashed-dot, and August 27th – green dot.

2.2 Results

The CO feature that is the focus of this research is found in the K filter bandpass at about $2.3\ \mu\text{m}$. Molecular band heads are different than atomic absorption lines in that they represent hundreds of absorption lines corresponding to energy transitions in the form of rotations and vibrations. This CO feature represents energy transitions of two, therefore the four strong band heads are the 2-0, 3-1, 4-2, and 5-3, which can be seen in Figure 2. Additional band heads exist (i.e. 7-5), but strong atmospheric contamination makes them difficult to distinguish.

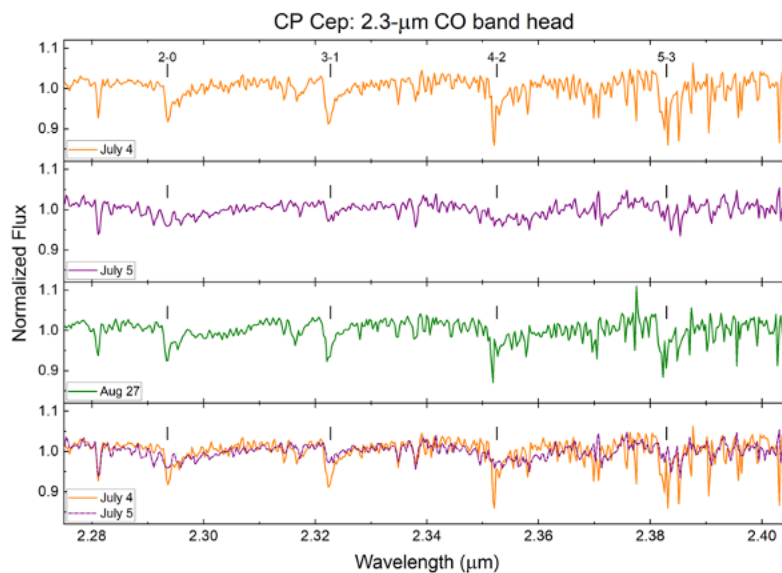


Figure 2. Normalized spectra for CP Cep for the region where CO absorption occurs. Transitions are labeled in the top panel.

Figure 2 shows the decrease in strength of the CO from July 4th to July 5th and the similar strength of August 27th to the 4th. We found equivalent widths of the 3-1 transition because it appears to be the cleanest in our dataset. The July 5th equivalent width was about half that of the July 4th, which confirms that more CO has been destroyed as the temperature of the star increased. The August 27th equivalent width was almost the same as July 4th but was over three periods later which suggests that this feature is in the star atmosphere and varies with pulsation.

3. Conclusions

We have demonstrated using spectroscopy that CO in the atmospheres of classical Cepheids varies with pulsation, confirming the results of photometric studies. We plan on continuing this research by determining the effect this changing opacity has on filter magnitudes. In addition to CP Cep, we plan to expand this to other Cepheids – specifically exploring longer and shorter periods to see if spectral observations match the theoretical predictions and photometric observations.

Acknowledgements

This paper includes data collected by the TESS mission, which are publicly available from the Mikulski Archive for Space Telescopes (MAST). Based on observations obtained with the Apache Point Observatory 3.5-meter telescope, which is owned and operated by the Astrophysical Research Consortium. We also acknowledge the support of the Department of Physics & Astronomy of Brigham Young University.

References

- Cushing, M. C., Vacca, W. D., & Rayner, J. T. 2004, *PASP*, 116, 362
Hamer, S. L., Ardern, S., Scowcroft, V. 2023, arXiv e-prints, arXiv:2302.14075
Leavitt, H. S. & Pickering, E. C. 1912, *Harvard College Observatory Circular*, 173, 1
Marengo, M., Evans, N. R., Barmby, P., Bono, G., Welch, D. L., Romaniello, M. 2010, *ApJ*, 759, 146
Scowcroft, V., Seibert, M., Freedman, W. L., Beaton, R. L., Madore, B. F., Monson, A. J., Rich, J. A., Rigby, J. R. 2016, *MNRAS*, 459, 1170
Vacca, W. D., Cushing, M. C., & Rayner, J.T. 2003, *PASP*, 115, 389
Wilson, J. C., et al. 2004, *SPIE*, 5492, 1295

Data Quality Task Force Synopsis

Matt Craig¹, PhD; and Mark Munkacsy²

¹Department of Physics and Astronomy, Minnesota State University Moorhead;

mcraig@mnstate.edu

²Portsmouth, RI; Mark_Munkacsy@alum.mit.edu

Subject Keywords

AAVSO International Database; Photometry, CCD; Photometry, CMOS; Statistical measures of quality

Abstract

The Data Quality Task Force (DQTF) was an ad-hoc AAVSO committee chartered to assess the issues that affect AAVSO data quality, quantify the fraction of data affected, and provide recommendations for improvement. The AAVSO holds all observer stellar brightness measurements in the AAVSO International Database (AID). The DQTF analyzed samples of CCD and CMOS data from the AID, and found discrepant data, missing data fields, and data values inconsistent with AAVSO reporting instructions. However, only a few researchers have complained about AID data quality. Nevertheless, the DQTF recommends a strategy built upon six straightforward ways for observers to improve the quality of their submissions.

1. Introduction

This is a summary of the final report of the AAVSO Data Quality Task Force (DQTF), formed in November 2022 to evaluate the current quality of the AAVSO International Database (AID), and if appropriate, to recommend changes to improve the quality of the data in the AID.

The DQTF encountered two primary challenges:

1. There is no baseline set of metrics gathered from the AID from which changes in quality can be measured; further, there is no general consensus on the algorithms that can be used to measure quality, given what is currently archived in the AID.
2. There is no established threshold level of quality to distinguish between acceptable AID data and unacceptable data. Instead, knowledgeable photometrists have compared levels of quality that can be achieved by experienced observers using today's equipment and techniques to what is found in the AID's historical record – and found that there is significant room for improvement in the AID.

Even casual examination of AID data using the AAVSO Light Curve Generator will quickly identify discrepant data, and there have been anecdotal reports of researchers expressing frustration with the quality of the AAVSO's data. Both of these have triggered a concern that the AAVSO's

reputation is potentially at risk unless the AAVSO is proactive in understanding the quality of the AID and taking action to improve or preserve that quality.

The DQTF elected to focus on stellar photometric data obtained using CCD and CMOS detectors. These data are where the greatest number of new and inexperienced observers have been contributing data and where casual sampling has suggested that there is the most opportunity for improvement.

1.1 DQTF Membership

Task force members included:

- Arne Henden
- Bert Pablo
- Brian Kloppenborg
- Ed Wiley
- Ken Menzies
- George Silvis
- Matt Craig
- Mark Munkacsy
- Tom Calderwood
- Gordon Myers

1.2 Data Quality Definition

Data Quality uses statistical measures to determine how well the data achieves some objective. Our data objective is to precisely, consistently, and accurately measure the variation in a star's brightness over time. The most common and applicable statistical characteristics and measures used to quantify Data Quality include:

- **Repeatability:** Assess how well an individual observer can repeatedly measure a star's brightness in a short period of time. This measure of repeatability is usually referred to as 'precision' (random error) and is normally reported as standard deviation (square root of variance) of the sample mean of several repetitive measurements.
- **Consistency:** Determine the level of agreement between measurements of a given star from multiple observers over the same, specific interval of time. Each observer will likely use slightly different equipment and methods: scope, camera, filter, sky conditions, software, calibration, and selection of comparison stars. Each of these factors may lead to differences (bias/systematic error) in the measured brightness of the target. These differences are typically larger than the precision reported by each individual observer. However, this is not always true, especially when the star is very faint.
- **Accuracy:** Assess how well a measurement agrees with the known true brightness of the star (generally difficult to assess for a variable star, but much better defined for constant stars used as photometric standards). Accuracy is related to consistency in the sense that we hope that all measured magnitudes reported by multiple observers agree with each other and also agree with the known 'true' magnitude.
- **Completeness:** Assess how much data for every portion of a star's period (light curve) is missing. Obviously, our data is never (and never will be) 100% complete; we have both a

day/night cycle and an annual cycle which prevent 24/7 observation of most stars. We also lack sufficient observers to fill in all our target light curves.

2. Current State

During its 112-year history, AAVSO has undertaken a few efforts to ensure data quality. The largest effort was the AAVSO Data Validation Project¹ executed in 2002. In the years since, the number of data points in the AID has risen dramatically, fueled largely by the rise in popularity of image-based photometry with associated software that automates much of the analysis and report generation process.

Although casual review of AAVSO light curves will quickly reveal discrepant points (primarily after 2006), few researchers have reported complaints about AAVSO data quality. Sampling of the AID was done by members of the DQTF during preparation of this report.

Some examples of these findings and known quality issues are listed in the following subsections.

2.1 Betelgeuse

During the “great dimming event” of 2019-2020, many observers contributed UBVRi data for this bright star. The resulting light curve shows numerous data quality problems (Figure 1).

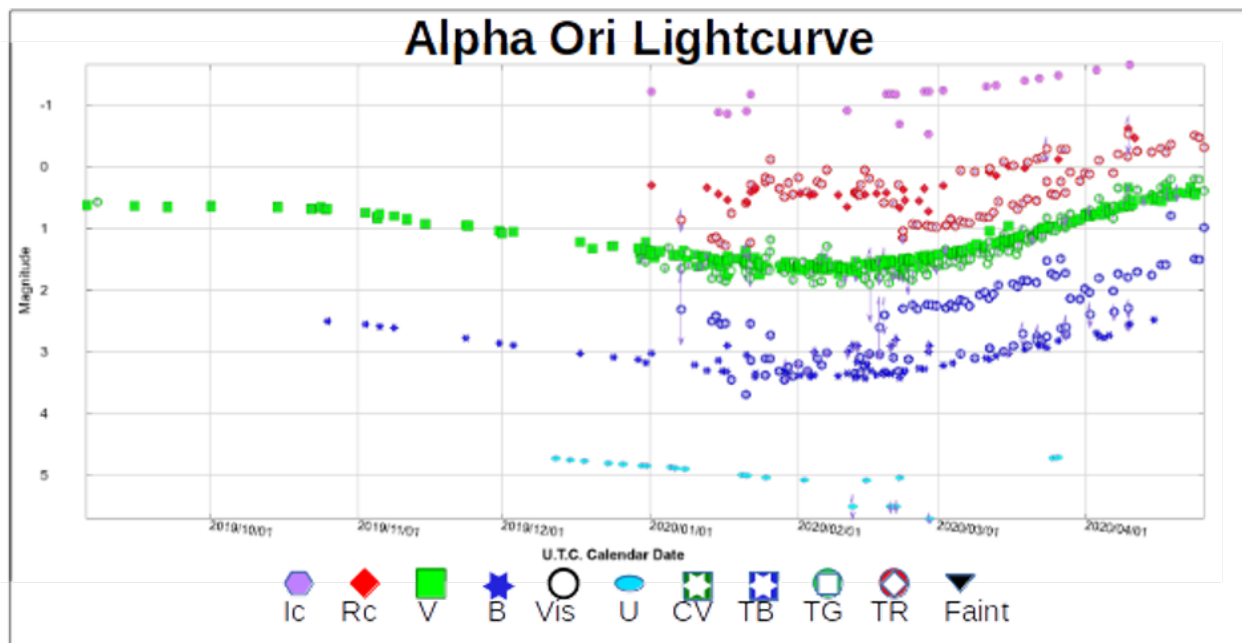


Figure 1. Light curves for Betelgeuse from AAVSO database.

¹ Malatesta, *The AAVSO Data Validation Project*, JAAVSO Vol 34, 2006, p 238.

Notice, in particular, the almost 1-magnitude offset between Johnson B data and B data extracted from the blue channel of tri-color cameras (e.g., DSLR) (TB). Notice similar issues with red channel data (Rc and TR). There are also clearly discrepant values for U and I bands. (Most error bars in this diagram and the two succeeding diagrams are too small to see.)

2.2 VV Cep

Figure 2 shows data from two different observers for VV Cep, a complex binary system:

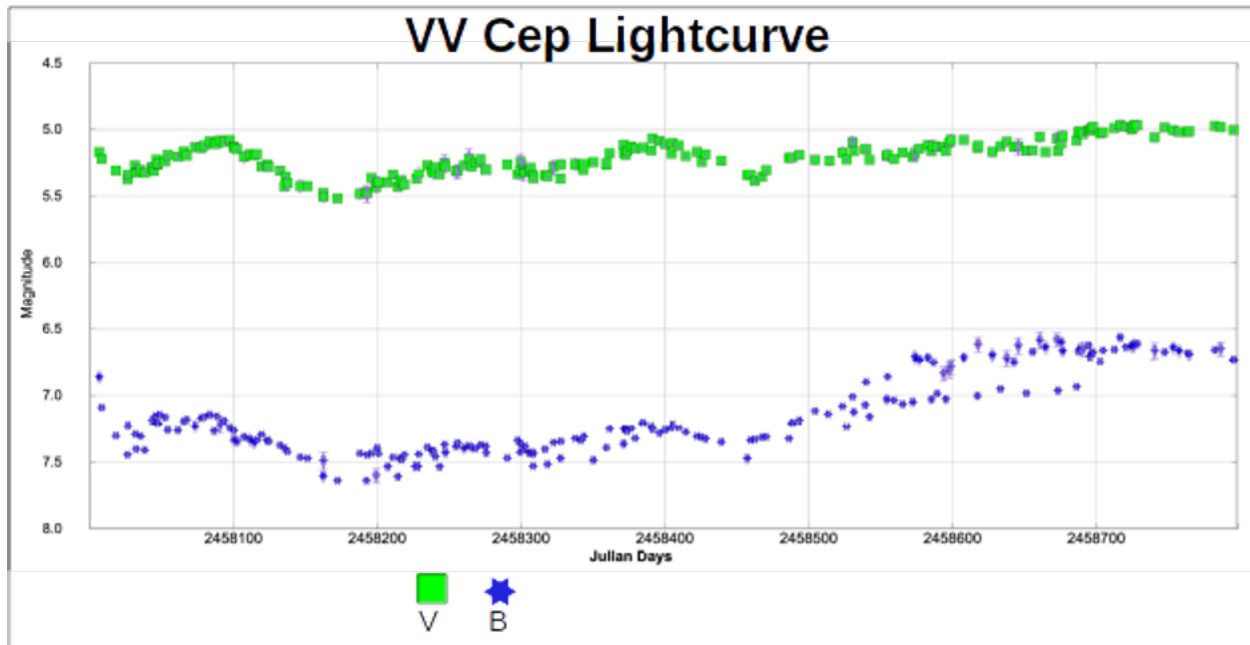


Figure 2. Data from two different observers for VV Cep from AAVSO database.

Although data from the two observers fits well for Johnson V, there is a clear systematic offset between the two observers between JD 2458500 and 2458700, where two distinct, parallel curves are visible. Another instance with a smaller offset between the two observers is visible from 2458150 through 2458400.

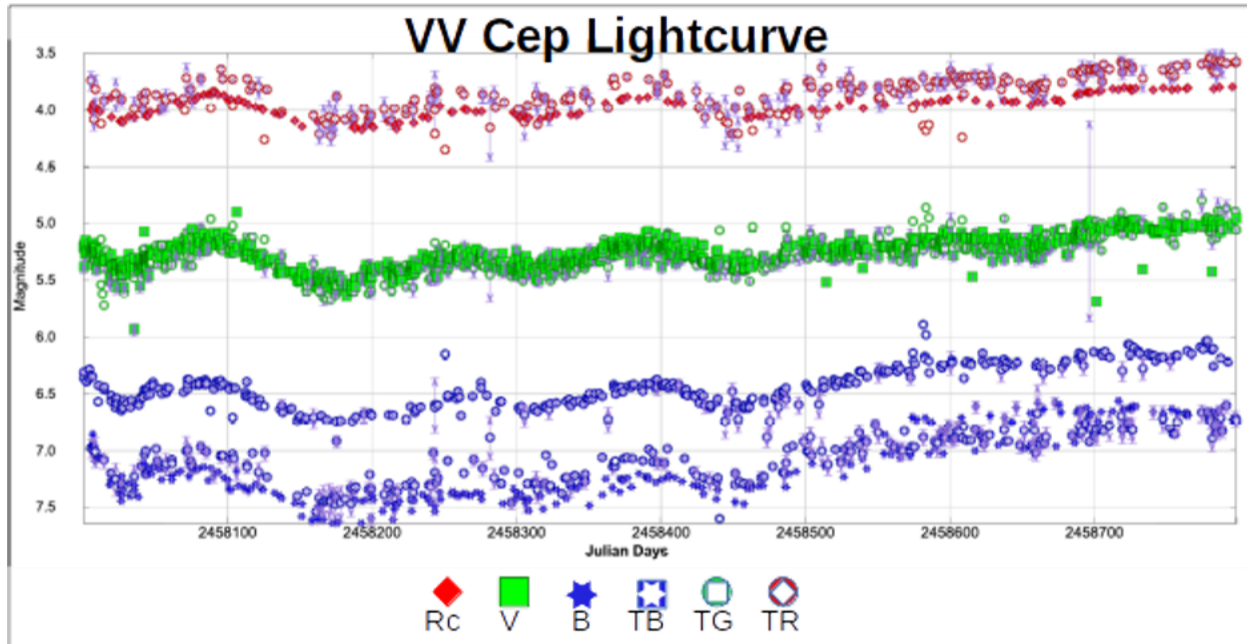


Figure 3. VV Cep CCD/CMOS data from all observers from the AAVSO database for the same period as in Figure 2.

Figure 3 shows CCD/CMOS data from all observers for the same period. Here the data from the prior graph is visible in a broader context. Several things are notable from this light curve:

- Throughout the entire time period, there is approximately a 0.2 magnitude offset between the Cousins red data (Rc) and the tri-color red data (TR), with the TR data running consistently brighter than Rc.
- There are, effectively, three blue curves: one is tri-color blue that starts around magnitude 6.5, consistently about 0.5 magnitude brighter than the other two blue curves, one of which is Johnson blue, while the other is *another* tri-color blue. Over some timespans, the bottom two blue curves consistently show the Johnson blue somewhat fainter than the tri-color blue, but beyond about JD 2458500, the prior clear offset between the two has gone away, and the scatter of the two curves is intermingled.

One of the findings in this report is that TG and V data *can* be reliably intermingled, while the pairs Rc/TR and B/TB should *not* be intermingled.

2.3 Missing and Discrepant Data Fields

A sample of AID data from 10 program stars (W And, Y And, RR And, S Pav, W Per, T UMa, YZ Cnc, RS Boo, BP Tau, and R Leo) was checked for consistency against AAVSO submission guidance. These checks were performed on 41,151 CCD/CMOS/DSLR observations, providing the following insights:

- Airmass: 10% of the sample was missing the airmass field. 1% had an excessively high airmass.
- Transformed: 90% of the sample had not been transformed
- Chart: 1% of the sample had a missing or invalid AAVSO chart ID
- Check Star: 11% of the sample had no check star listed or the check star listed was not on the chart. 93% of the sample provided insufficient information to perform a check star magnitude verification.
- Cadence: 5% of the observations of long-period variables in the sample were reported with an inappropriate cadence (a time series performed during a single evening)

3. Recommended Strategy

The DQTF identified six broad strategic elements to address quality improvement in the AID:

1. Establish metrics and a monitoring program to provide long-term insight into the quality of the AID.
2. Strengthen quality checks performed at the time of observation submission. Some of these checks (flaggings) would be advisory to the observer, and some checks would be used as the basis for blocking the submission of some non-compliant observations. These improvements will affect the submission process, the data reporting format (and its associated documentation), and possibly the data structure of the AID itself.
3. Provide observers with stronger feedback on the quality of their observations. This quantitative assessment of photometry quality goes beyond flagging the compliance issues checked during the submission process. This feedback will provide measures of consistency with other observers, giving observers a way to measure their own progress toward improving the quality of their work.
4. Improve the overall level of observer knowledge through education, improved best practices directives, explanations of how to use the feedback from the prior strategic element, and the availability of additional tools to support individual observer's quality assessment and improvement.
5. Emphasize quality over quantity by modifying existing observer award incentives (and AAVSO culture) that sometimes encourages observers to value quantity over quality.
6. Improve the packaging and screening of data provided by the AAVSO to researchers, in part to create clear expectations of the quality that researchers can expect from the data and to control the release of AID data that has already been flagged as problematic.

AAVSO Quality Strategy

1. Measure & monitor
2. Quality check at submission
3. Strong observer feedback
4. Education to build knowledge
5. Value quality over quantity
6. Better-informed end users

Each of these six strategic elements is discussed in more detail (with specific recommendations) in the next sections. The recommendations are summarized in Section 4, where each recommendation is also given an implementation priority. The Final Report of the DQTF contains

27 specific recommendations. Some of those recommendations are contained in this synopsis – all are provided in the Final Report.

3.1 Establish Metrics and a Monitoring Program

The first strategic element is the creation of a metrics and monitoring program that periodically generates numeric measures of the quality of the AID. The only way to know if any of the recommended quality-related changes actually do improve the quality of the AID is to measure and monitor AID quality.

Four metrics are recommended:

- A **consistency** metric: This metric (or collection of metrics) measures how well the measurements in the AID align with each other. An actual measurement of consistency requires establishing a community consensus on the "true" magnitude of the target star. (Because of the difficulty in establishing a community consensus for some stars, only a subset of stars in the AID would be included in this metric.) Once we know this community consensus, then we can measure the difference between each AID measurement and the community consensus. With a set of differences, we can define several different numbers to summarize the differences, including the variance of the differences (and associated standard deviation) and the histogram of the differences.
- A **discrepancy** rate metric: During the creation of the community consensus, some discrepant measurements will stand out as inconsistent with the emerging consensus. (Depending on how the community consensus is calculated, the discrepant measurements may be excluded from the consensus calculation.) Once an observation has been flagged as discrepant for purposes of collecting metrics, that observation should probably not contribute to the consistency metric. Instead, a discrepancy metric can be used to summarize the number of discrepant observations (measured and reported as the number of discrepant measurements per 1,000 AID entries).
- A **compliance** metric: This metric measures how well observers are following rules and guidance regarding the preparation of their reports and the processes they use in their photometry. There is a series of proposed tests that would be run on each CCD/CMOS observation in the AID. The metric is the fraction of individual tests that pass.
- A **check star** metric: The AID contains information on the check stars used with each observation. Provided that values for all the associated fields in the report (described in Appendix A) have been provided, it is possible to compare the observer's photometric magnitude for the check star against the check star's standard magnitude in the AAVSO sequence. The difference between the two is a residual error; the set of all residual check star errors would be summarized by the check star metric, most likely as the rms value of the residual error.

3.2 Strengthen Quality Checks at Time of Data Submission

The previous section addressed the metrics and monitoring program: ways to measure the quality of what is contained in the AID. *This* section addresses the second strategic element: checks performed when observations are submitted (via WebObs). Checks performed during submission potentially serve four purposes:

- They provide an opportunity to absolutely block submission of observations that are clearly flawed, preventing observations with obvious quality problems from entering the AID.
- They provide an opportunity to flag questionable observations to force the observer to take a second look at suspicious submissions. Messages, for example, that say, “This observation has an unusually large uncertainty, is it correct?” give the observer an opportunity to check for typographical or transcription errors and to correct those errors before the observation enters the AID.
- They provide an opportunity to provide the observer with educational feedback. A quality check that has failed, if described to the observer in plain language, could well be the result of the observer not recognizing the relationship between fields in the submission or not recognizing best practices applicable to this particular kind of observation.
- They provide an opportunity to show the operator the current light curve for this target star, prompting the operator to see where this new observation fits against other observers’ reports on the star. We intentionally encourage observers to check their observations for consistency with observations from other observers.

The DQTF recommends the application of acceptance criteria for all data submitted to the AID. Failures should be brought to the observer’s attention prior to acceptance of the observations. The observer should be given the option to either forcibly submit the data in its current form or modify the submission. Failures of certain checks should be absolute, with the observer not given the option to forcibly submit. Full implementation of some acceptance tests may require modifications to the AAVSO Extended File Format (AEFF). The resulting AEFF changes may require changes to the AID table structure.

Since most observers submit AEFF files that have been prepared by software tools, any change to the AEFF format will involve coordination of matching changes in both AAVSO software and third-party software. For this reason, this recommendation may need to be implemented in phases spread over a significant amount of time. This will allow coordination (and synchronization) of AAVSO and third-party software changes with the new acceptance checks.

3.3 Provide Stronger Feedback

The third strategic element focuses on communicating back to our observers. There are several different ways (and times) that the AAVSO can reinforce the things that individual observers are doing well and to point out things the observer might not be aware of. The DQTF recommends multiple feedback mechanisms for our observers:

- Immediate flagging of observations with suspect data per Section 3.2 during the submission process.
- Create observing campaigns specifically designed to make it easier for observers to compare their results against the work of others.
- Periodic reporting of observer-specific metrics
- Certification
- Improved tools for observers to delete previously submitted data

A relatively inexpensive way to provide useful feedback to many observers simultaneously is through observing campaigns specifically tailored to offer an opportunity for observers to measure constant stars with well-known magnitudes. Although this has always been possible using Landolt standard fields, the AAVSO has neither emphasized their use nor collected observers' measured values in a recurring, organized way for long-term trend analysis and feedback.

The DQTF believes that specifically calling out short-term (but recurring) observing campaigns on some of these fields will benefit both participating observers and the AAVSO itself.

3.4 Improve Observer Knowledge

One finding of the DQTF is that AID quality can be degraded when observers take techniques that work well for some targets and apply them inappropriately to other targets. For instance, there are techniques that are important for imaging bright stars (to reduce the risk of saturation-related nonlinearity and scintillation noise) that will degrade the quality of photometry performed on faint cataclysmic variables during quiescence.

The DQTF recommends that the AAVSO provide multiple education opportunities for observers to understand photometric best practices, how measurements are used by researchers, and the importance of matching observing technique to each star's "observing profile."

The existing CCD/CMOS and DSLR Guides are large documents. The DQTF recommends augmenting these guides with smaller "Best Practices" guides that can serve as gateways to the more complete documents.

As observers work to improve their photometry, a natural way for observers to split the problem into smaller chunks is to organize the pipeline into two parts: the acquisition of calibrated photometric images and the process of measuring flux on each image set and translating that flux into standard magnitudes. By providing observers with controlled synthetic images, observers can test and troubleshoot the two halves of the process separately.

As an additional benefit, synthetic images can be an essential tool as the AAVSO works with in-house and third-party software providers. By running these synthetic images through the different toolchains, anomalies can be identified quickly.

The DQTF acknowledges the investment that the AAVSO has already made in its CHOICE courses supporting photometry and the challenge of finding qualified instructors to enable more students to benefit from this superb training. The DQTF encourages the AAVSO to do more. In particular, there is the potential for synergy between the AAVSO's courses and the certification program recommended below; professional certification programs in other fields often include both a classroom component and a hands-on, skills demonstration component. Encouraging observer certification may create a renewed demand for student participation in AAVSO courses.

Greater use of recorded videos might reduce the barrier to entry for new observers. While not as detailed as a CHOICE course would be, they could provide a free introduction to some of the topics covered in more detail in CHOICE courses.

Consider creating how-to webinars that describe Best Practices for different types of variable star imaging. These might provide topics for individual Section presentations.

Some assessment of observer submissions cannot be performed by examining submissions in isolation, but instead requires looking at *each* submission as *part of a set* of observations gathered by multiple observers both before and after the time of this particular submission. In addition, by examining an observer's submissions over an extended period (one or two months), trends may be visible that are hard to discern by looking at observations one at a time.

For these two reasons, the DQTF finds value in a periodic feedback cycle that aggregates all of an observer's submissions over some extended period:

AAVSO observers form a diverse population, with experience ranging from professionally trained photometrists to beginners with no prior photometry experience. A certification program can help observers perform self-assessment of their photometric skills, identifying weaknesses that they can then address as part of self-improvement. The DQTF very much wants to avoid introducing an onerous process (or something excessively bureaucratic); the word "certification" may itself be too strong.

The certification program would recognize participation in quality-focused observing campaigns, requiring that observers demonstrate particular skills (e.g., transformation) and accomplishments (e.g., measurements falling within some threshold of a star's reference magnitude). The certification program could require periodic recertification, perhaps on a 5-year cycle. The certification program could include recognizing specialization (e.g., exoplanet transits, stars of extreme color, bright stars). And the certification program perhaps doesn't use the word "certification" at all, instead using words connoting a finer-grained progression from novice to expert photometrist.

3.5 Quality Over Quantity

The fifth strategic element calls for rethinking the existing AAVSO Observer Awards, which today are based exclusively on the number of measurements submitted to the AID. Several of the

AAVSO best practices call for observers to perform the same imaging multiple times, combining the results into a single averaged measurement submitted to the AID. For many (but not all) observing profiles, the submission of a single, averaged data point is more useful to a researcher than submission of the multiple raw measurements that were used to create the aggregated point. However, current Observer Awards provide a counter-incentive to this best practice.

Although the DQTF did consider recommending that the AAVSO *replace* the existing Observer Awards, our final recommendation recognizes that the existing award structure is steeped in AAVSO history and culture, and it may be preferable to *supplement* the existing awards rather than replace them. A prime objective is to reward high-quality photometry. Even a Lifetime Data Quality Award may be considered. It might include consideration of data quality parameters, transformation of magnitudes, completion of Choice Courses, participation in Campaigns, and participation in the Certification Program.

3.6 Improve the Packaging and Screening of Data for Researchers

The final strategic element addresses the community of researchers that download and use data from the AID to support their research. Currently, researchers requesting AAVSO data are provided with two things: a file containing the requested data and a file describing the format of the data. The DQTF noted that researchers are not being provided with any explanation of how AID data quality is managed, what kinds of quality checks have already been performed on the data, what levels of precision and accuracy can be expected, or how to interpret some of the more complex values (e.g., interpretation of check star magnitude).

4. Consolidated List of Recommendations

ID	DQTF Final Report Section	Topic	Recommendation	Priority	Effort
a	3.1	Metrics & Monitoring	Establish metrics and a monitoring program that periodically extracts a set of measures from the AID for determining overall trends (changes) in the quality of the AID.	High	High
b	3.1.1	Metrics	Gather 4 metrics to measure consistency, discrepant observation rates, submission compliance with guidelines, and check star magnitude match to standards.	Medium	High

ID	DQTF Final Report Section	Topic	Recommendation	Priority	Effort
c	3.1.1.1	Metrics & observing sections	Involve the observing sections in the metrics monitoring program, since some of the compliance checks will be dependent on the observing profiles and because establishing community consensus will be different for the different sections.	Medium	Low
d	3.1.2	Collection cadence	Metrics measurement to be performed on an annual cycle.	Medium	High
e	3.2	Data submission acceptance checks	Institute the application of acceptance criteria for all data submitted to the AID per the following table. Failures should be brought to the observer's attention prior to acceptance of the observations. The observer should be given the option to either forcibly submit the data in its current form or modify the submission. Failures of certain checks (if indicated in the table) should be absolute, with the observer not given the option to forcibly submit.	High	High
f	3.3.1	Observing campaigns	Provide both dedicated "quality check" observing campaigns as well as opportunistic quality check exercises that are add-ons to existing pop-up observing campaigns.	Low	Low
g	3.3.2	Observation Deletion	Improve the online tools that allow observers to delete selected observations that they previously submitted.	Low	Low
h	3.4	Education	AAVSO to provide multiple education opportunities for observers to understand photometric best practices, how measurements are used by	Medium	High

ID	DQTF Final Report Section	Topic	Recommendation	Priority	Effort
			researchers, and the importance of matching observing technique to each star's "observing profile."		
i	3.4.1	Best practices	Create a series of "Best Practices" documents that summarize key processes and procedures that help ensure quality data is submitted to the AID; existing AAVSO guides (e.g., the AAVSO Guide to CCD/CMOS Photometry) should be updated to contain the same best practices and to serve as references to the Best Practices documents.	High	Low
j	3.4.2	Synthetic images	Create and distribute a set of synthetic star images together with values of "truth" for the magnitudes of each star in the synthetic images. Distribute these images widely, including to observers and to the community of third-party photometric software developers and vendors.	High	High
k	3.4.3	Training courses	(1) Explore ways that the existing CHOICE courses in photometry can be extended and expanded. (2) Re-activate/Add a measurement uncertainty course. (3) Create and provide webinars related to Best Practices for different types of variables.	Medium	Low
l	3.4.4.1	Feedback during submission	Provide the results of submission checks back to the observer in a form that educates the observer.	High	High
m	3.4.4.2	Post-submission feedback	Provide feedback to observers that aggregates their submissions over a period of several months.	Medium	High

ID	DQTF Final Report Section	Topic	Recommendation	Priority	Effort
n	3.4.5	Certification	Create an observer certification program for CCD/CMOS observers with both a theoretical (book learning) element as well as a skill demonstration element.	Low	High
o	3.5	Observer awards	AAVSO to supplement the existing observer recognition awards (based on the number of measurements submitted) with another recognition program that removes the incentive to provide high-cadence measurements just for the sake of recognition.	Low	Low
p	3.6	Data for researchers	Expand the use of the existing “validation” flag in the AID so that it can be used to indicate to researchers which data meets the standards the AAVSO sets for completeness of submission and precision/accuracy. Consider what AVSpec is already doing.	Low	High
q	3.6	Download filtering	Consider adding filtering tools to the existing AID data download tools to allow a researcher to get, for example, only transformed data or only data with a specific comparison star.	Low	High
r	4.1	Third-party software	Provide test/synthetic images and ask software vendors to demonstrate compliance and capabilities using these images.	Medium	High
s	4.2	Observing profiles	AAVSO to formalize an “Observing Profile Dictionary” that identifies a set of observing profiles, eventually to include best practices and quantitative quality measures specific to each profile (including cadence, exposure time, filter, accuracy, and SNR recommendations).	Low	High

ID	DQTF Final Report Section	Topic	Recommendation	Priority	Effort
t	4.3	Color Systems	Provide clear direction to observers to avoid trying to transform magnitudes made with one filter system into a different filter system. For example, do not attempt to transform a sloan g' magnitude into a Johnson V magnitude. (The one possible exception is the transformation from tricolor TG into V.) Further, explain how observers should be reporting their transformation coefficients.	Medium	Low
u	4.3	Transformations whenever possible	Provide clear direction to observers that color transformations should be done whenever possible and that two-color transformations are strongly preferred over single-filter transformation. (However, this does not supersede other recommendations associated w/tricolor cameras.)	High	Low
v	4.3	Single-Filter Transformation	Once the needed background investigation is finished, create a procedure that describes how to do single filter transformations, and create a supporting database of mean (B-V) colors on targets that are recommended for single-filter observers. Ensure that the procedure explains how observers should be reporting their transformation coefficients and assumed mean color.	Medium	High
w	4.4	Extinction	Provide observers with a strong recommendation to include extinction corrections in their photometry processing pipeline. Add material covering this to existing AAVSO guides and courses.	Low	Low

ID	DQTF Final Report Section	Topic	Recommendation	Priority	Effort
x	4.4	Ensembles	Provide observers with a strong recommendation to incorporate comparison star ensembles into their photometry methodology and make associated changes to the AEFF to capture associated data as part of the measurement record.	Medium	High
y	4.5	Tri-color cameras	Perform more detailed investigation of tri-color cameras. In particular, the investigation should determine limits of their accuracy, usability of red and blue channels, intrinsic image processing performed on even images stored as “raw,” and consistency between cameras within and between manufacturers.	Medium	High
z	4.6	Citizen science lessons learned	Talk with citizen science researchers before rolling out a quality feedback program to find effective ways to give feedback in a constructive, non-condescending way.	Medium	Low
aa	Appendix A	AEFF Specification	Provide a stronger specification/description of the AEFF format that includes references to the submission checks performed by WebObs, to preferences in some multi-purpose fields (e.g., a preference for AUID in the CNAME and KNAME fields), and to conventions used in fields (e.g., airmass is relative to local zenith airmass, not to sea level zenith airmass).	Medium	Low

Nights on Fire: The Extent of Smoke over North America in Summer 2023

Matthew Craig

Department of Physics and Astronomy, Minnesota State University Moorhead, 1104 7th Ave S,
Moorhead, MN 56560, USA; mcraig@mnstate.edu

Subject Keywords

Photometry, CCD

Abstract

The increasing frequency and extent of forest fires in North America has led to increasingly frequent smoke cover on nights which would otherwise have been clear. The talk presented at the 112th AAVSO meeting, and summarized in this paper, aims to illustrate the extent of the problem by sharing an animation of the satellite-determined extent of smoke over North America from April 1, 2023 through September 2023. Much of the continental US had at least light smoke cover for a substantial portion of the summer, and there are locations which had smoke cover the entire summer. The reddening this causes is apparent to the eye on a sunny day; the effects of this reddening on starlight should be investigated systematically.

1. Introduction

The skies over Moorhead, Minnesota seemed unusually smoky this past summer. On virtually every cloud-free day sunlight appeared more yellow than usual. On many cloud-free days, direct sunlight was not visible at all because the layer of smoke over the region was too thick. The extinction and reddening apparent to the naked eye during the daytime will also affect the light of other stars at night.

This paper documents the frequency of smoky nights in summer 2023 in Moorhead, Minnesota and puts the primary source of that smoke, Canadian wildfires, into perspective. The basis for concluding that the unusually extensive fires this summer are partially attributable to human-caused climate change will be briefly discussed. A tool is provided to allow others to build a similar visualization at their location.

2. Methods

The US National Oceanic and Atmospheric Administration (NOAA) generates daily a map of the extent of smoke over North America. Smoke extents are mapped by an individual reviewing images collected by satellite over the course of the day. These maps are available freely for download in a standard GIS format from NOAA¹ using the settings shown in Fig. 1. Map

¹ <https://www.ospo.noaa.gov/Products/land/hms.html#data>

availability begins in 2003. NOAA classifies the smoke density as light, medium, or heavy, and explicitly warns that the maps are not quantitative measurements of smoke particle concentration².

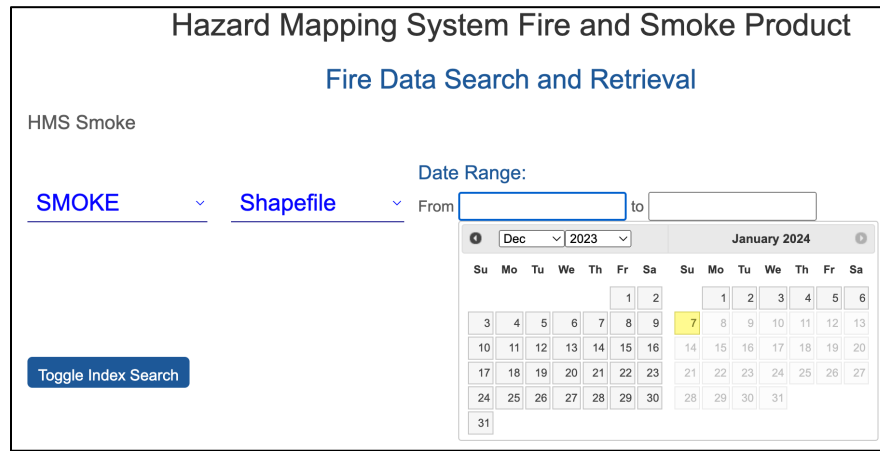


Figure 1. Settings to obtain smoke extent shape maps from NOAA. After selecting a range of dates, a list of files will be presented for download. Screenshot obtained Jan 7, 2024.

Maps from Apr 1, 2023 through Nov 1, 2023 were retrieved using a script³ written in Python. Animations of the smoke extents were generated in a Jupyter notebook (Kluyver 2016) using ipyleaflet⁴.

In addition to generating maps, a cumulative count of the number of smoky and clear nights since Apr 1, 2023 was calculated. Since the smoke information is generated by visual inspection of satellite images taken in visible wavelengths, extents are only available during the daytime. A night counted as smoky if Moorhead, MN fell within the extent of the smoke areas on that day. While this approach might overcount smoky nights if, for example, there was smoke in the morning that cleared later in the day, in practice it should have no significant effect on the counts for this past summer. Every day over the summer had detectable smoke overhead so it seems a relatively safe assumption that it was also smoky overnight.

3. Results

Maps of smoke extent on a few nights representative of summer 2023 are in Fig. 2; the full animation is available online. Extensive smoke started in May, earlier than it has in the past. The first date shown in Fig. 2 was the first day with smoke overhead that was visually obvious from Moorhead. The next date, May 14, was the beginning of 131 straight days of smoke cover. The next smoke-free day was Sep 23, 2023.

² <https://www.ospo.noaa.gov/Products/land/hms.html#about>

³ The code used to download the data, generate the animation shown during the talk, and generate the plots in this article is available here unless otherwise noted: <https://github.com/mwcraig/smoky-skies>

⁴ <https://ipyleaflet.readthedocs.io/>

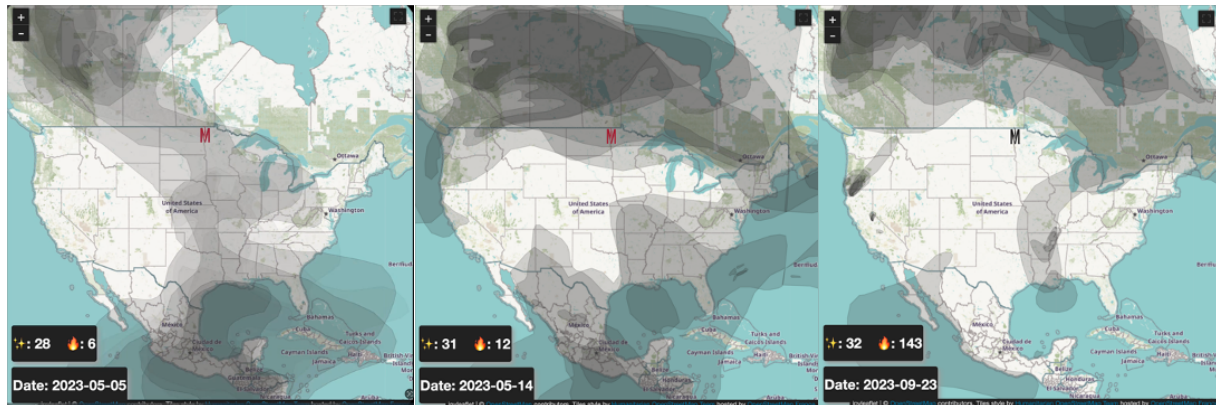


Figure 2. Maps of smoke extent on a few days from 2023. The “flaming M” marks the position of Minnesota State University Moorhead and is colored red on days with smoke and black on days without smoke. On each date, the cumulative clear nights since Apr 1, 2023 is marked with “⚡” and the number of cumulative smoky nights is marked with “🔥”. The full animation is available at https://youtube.com/shorts/8_7MbZYqS70.

The cumulative number of smoky and clear nights is shown in Fig. 3. The appearance of smoke in April and May is fairly unusual for the area. Smoke dense enough to affect sunlight has not been observed by the author at that time of year in the past. Smoke was not completely absent until sometime in Oct, 2023, unusually late in the year.

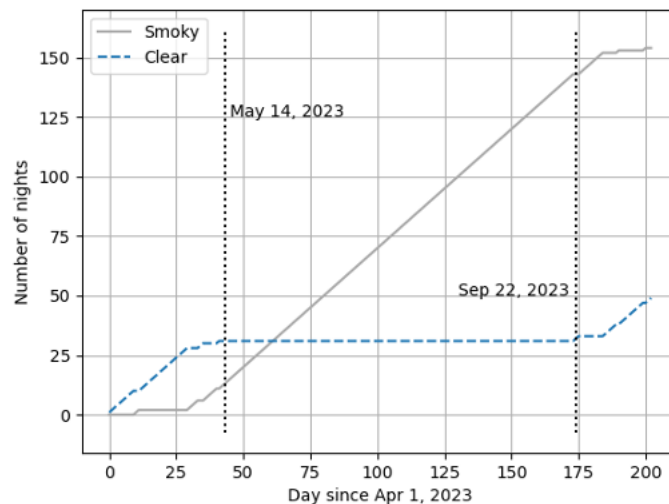


Figure 3. Cumulative number of clear and smoky nights since Apr 1, 2023. The beginning and end of a stretch of 131 straight days of smoke are marked by the vertical lines.

4. Discussion

While it is clear from the animated maps of the extent of the smoke that almost all of it was from fires in Canada, the stretch of continuous smoke cover indicated in Fig. 3 offers another clue. Figure 4 shows a graph of the cumulative hectares of land burned in Canada for a few years,

including 2023. The fires started in Canada in May, earlier than in past years, and continued to burn new land into October, later than in past years.

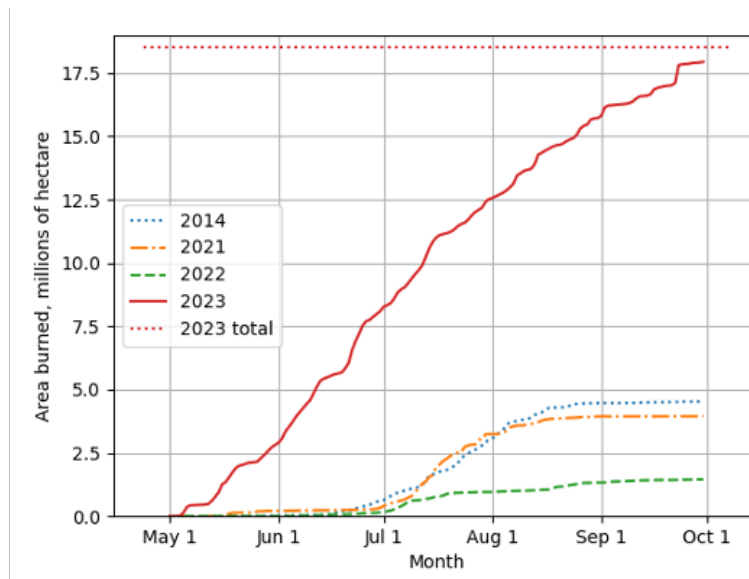


Figure 4. Cumulative area burned in Canada, shown for several years⁵. Data for 2023 is included through Sep 30, 2023, for consistency with the data available from prior years. The horizontal line indicates the area burned by the end of 2023.

A few things stand out in Fig. 4. The fire season started far earlier than in other years and continued. Fires continued to consume new land, almost without pause, through September. While fires began as early as May in prior years, the conclusion from Fig. 4 is that those were isolated fires, since the number of burned hectares remained constant in those years until roughly the beginning of July. In the past, there appear to have been few, if any, large fires after the beginning of September. The area burned in 2023 was exceptionally large. Fires consumed more than twice the area consumed in any other year going back to 1983, as shown in Fig. 5.

One of the underlying causes of the extensive fires this year is almost certainly human-caused climate change. Globally, the warmest year in the past several thousand years was 2023. A careful study of a subset of the fires in Canada, those that burned in Quebec, estimates that human-caused climate change increased the likelihood of an event of this magnitude by at least a factor of 2 (Barnes, 2023). Under current climatological conditions, the expected return time, i.e., the time until another event this extreme, is roughly 20 years. The expected return time in a world without greenhouse gases emitted by humans is hundreds to thousands of years, depending on fire weather index used to calculate the probability.

⁵ Data is from the Canadian Wildfire Information System
<https://cwfis.cfs.nrcan.gc.ca/maps/fm3?type=arpt&year=2023>

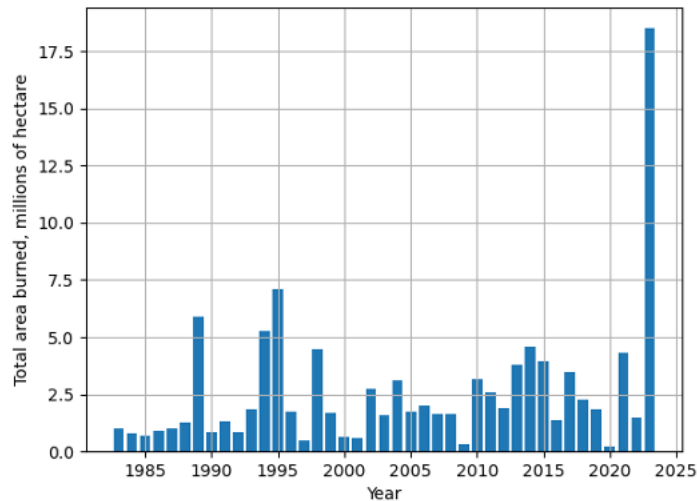


Figure 5. Area burned by wildfires in Canada⁶. The area burned last year far exceeds that burned in prior years.

5. Conclusions

Overhead smoke is likely to be a regular occurrence in North America over the summer for several years. Although the Canadian wildfire season was exceptional enough that is unlikely to recur for a couple of decades, 2023 was also unusual because of the absence of large wildfires in the western US. The assumption that extensive smoke is likely to be a regular feature of North American observing seems fairly safe. The smoke cover is often thick enough to visibly redden and dim sunlight and presumably affects observations made by AAVSO observers. While a careful study of the magnitude of the impact would be helpful, in the short run it is another reason to be careful in the selection of comparison stars and the apply color corrections.

References

- Barnes, C., Boulanger, Y., Keeping, T., et al. 2023, Climate change more than doubled the likelihood of extreme fire weather conditions in Eastern Canada, Grantham Institute for Climate Change, <https://doi.org/10.25561/105981>
- Kluyver, T., Ragan-Kelley, B., Pèrez, F., et al. 2016, Jupyter Notebooks -- a publishing format for reproducible computational workflows, in Positioning and Power in Academic Publishing: Players, Agents and Agendas, IOS Press, pp. 87 – 90, <https://doi.org/10.3233/978-1-61499-649-1-87>

⁶ Data from the Canadian Interagency Forest Fire Center, Inc., <https://ciffc.net/statistics>

Spectroscopy of “Be” Stars Exhibiting Rapid Variability: A Preliminary Report

*Diz, H. R. *, de Hilster, N., Desrosiers, J. B., Diaz Lopez, S., Di Lazzaro, M., Elias Cantalapiedra, J., Gebhard, G., Larsson, M., Martin, J., Piehler, G.*

*Corresponding author: hrickdiz@gmail.com

Subject Keywords

Be stars; omicron Andromedae; spectroscopy

Abstract

This is a preliminary report on a spectroscopic study by a group of amateur astronomers of a small group of Be stars in order to document rapid variability in spectral profile features. Be stars are non-super giant stars of spectral Type B that exhibit or have previously been observed to exhibit emission lines in their spectra. The stars selected for study have been previously reported in the literature to have short term photometric and spectroscopic variability. Being amateur astronomers, our backyard telescopes are small, ranging in aperture from 200 mm to 500 mm. Some in our group are using the LHiresIII spectroscope, but many of us are using DIY spectroscopes made with a 3D printer. Spread over seven time zones, we coordinate our observations so as to obtain as many exposures of a single target as possible. Exposures, typically ranging from 300 to 600 seconds, are not stacked, but rather are processed individually to yield a fine time resolution. Using mostly freeware such as specINTI and BASS, we are able to convert raw images to 1D profiles. Early results, presented here for the Be shell star omicron Andromedae (oAnd), suggest that there is rapid variation in the features of the H α line and the He I line at 6678Å. There also appears to be variation on a longer scale, i.e., 30 to 40 days, of the intensity of the V and R wings of the H α line, and the V/R ratio. As oAnd is a ‘shell’ star, there is a central absorption H α line, and the depth of that line also is observed to vary, as is, to a lesser degree the helium line at 6678Å. As this is a preliminary report, it is premature to provide statistical evidence to support any assertions of periodicity, and it is too early to suggest the implications of these line profile variations. We expect to conclude the study in the spring of 2024 and report final results at that time.

1. Introduction

A number of Be stars have been reported in the literature to have rapid variation in their spectral profiles as well as in their luminance (Briot et al. 2002, Percy 1986). A group of American, Canadian, and European amateur spectroscopists have teamed up to study this rapid variability. “Rapid” is defined here as variation on the scale of minutes to hours. Our goal is to document this spectral line profile variability in a select group of these variable stars, and to infer what we can about the stars’ behavior and structure from these spectroscopic features.

Be stars are hot spectral Type B non-Super Giant stars that have or have had Balmer emission lines in their spectra. They apparently have a circumstellar disk and rotate at a very high rate producing broad spectral lines. Depending on our line of sight relative to the orientation of the disk, we see various shapes in the spectral profile (Figure 1, after Rivinius et al. 2013).

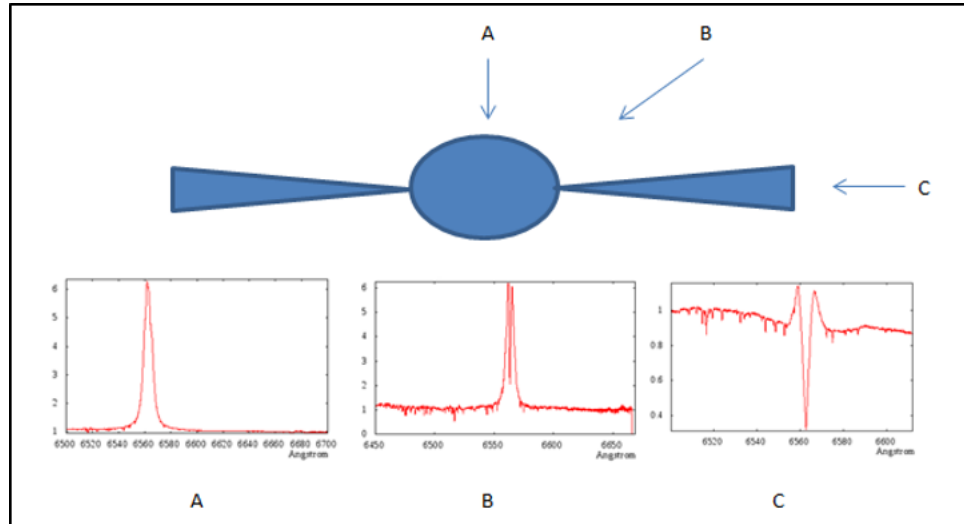


Figure 1. Schematic representation of a rapid rotating Be star with a circumstellar disk, along with typical spectral profiles of the $H\alpha$ region, as viewed from various perspectives. After Rivinius et al 2013.

“Be shell” stars are those that have a sharp central absorption feature in the core of the $H\alpha$ emission line, as shown in Figure 1B and C. The origin of the circumstellar disk is not well understood. It is hypothesized to consist of material (mostly hydrogen) that was lost from the surface of the star, rather than material gained from some external source (Porter & Rivinius 2003). Notice the presence of ‘wings’ in Figure 1C. The shape of the $H\alpha$ emission wings and the deep central absorption feature of shell stars is related to the optical thickness and kinematics of the disk (Rivinius et al 2006).

2. Methods

The project began in early September 2023 and will conclude by the end of spring 2024 when the nights become short in the northern hemisphere. Our first step was to select candidate stars viewable from the northern hemisphere, brighter than magnitude 6.5, and that were reported by Percy (1987) as being probable or possible rapid variables (Table 1). Each member of the study team was assigned to a star and was asked to collect as many observations of that star as possible. Once it was determined that variability was observed, all members of the team were asked to capture observations of that target. Since our team members are located in various time zones in Europe and North America, with a bit of luck with the weather, the exposures collected by a member of the team in the East will be supplemented not only by others in their region but also to the west, thus ‘virtually’ extending the night, and creating a lengthy time series of exposures.

Table 1. Targeted northern Be stars reported to have rapid variability, brighter than magnitude 6.5, and higher than 30° during the fall and/or winter. Shaded blocks containing Y indicate the star is visible that month in the eastern United States at latitude 31° N.

Name	V		Sep	Oct	Nov	Dec	Jan	Feb	Mar
	mag	Type							
gam Cas	2.47	B0IVpe	Y	Y	Y	Y	Y	Y	
bet Cep	3.22	B2IIIev	Y	Y	Y	Y			
59 Cyg	4.74	B1.5Vnne	Y	Y	Y	Y			
omi And	3.63	B6IIIpe	Y	Y	Y	Y	Y		
12 Vul	4.90	B2.5Ve	Y	Y	Y				
25 Cyg	5.10	B3IVe	Y	Y	Y	Y			
omi Cas	4.48	B5IIIe	Y	Y	Y	Y	Y	Y	
60 Cyg	5.40	B1Ve	Y	Y	Y	Y			
omi Aqr	4.70	B7IVe	Y	Y	Y	Y			
zet Tau	3.03	B2IVe				Y	Y	Y	Y
ome Ori	4.57	B2IIIe			Y	Y	Y	Y	Y
psi Per	4.31	B5Ve			Y	Y	Y	Y	Y
lam Eri	4.25	B2IVne				Y	Y	Y	Y
11 Cam	5.03	B2.5Ve			Y	Y	Y	Y	Y
48 Per	4.00	B3Ve				Y	Y	Y	Y

Our telescopes range in aperture from 8” to 20”, some with 3D printed DIY spectroscopes equipped with cooled CCD and CMOS astronomical cameras. Exposure times are determined by each observer based on the requirements of their system. However, typical exposure times are in the range of 300 to 600 seconds, with a goal of achieving a signal-to-noise ratio in the final 1D profile of 50 or greater.

Spectra are processed by a collection of software. Initial processing is accomplished with ‘specINTI’ by Buil and Desnoux (http://www.astrosurf.com/solex/specinti1_en.html). Processing by specINTI includes darks, flats, bias, and wavelength calibrations, noise reduction, atmospheric opacity adjustment, continuum rectification and normalization, and cropping. The software creates 1D profiles for each exposure separately as well as a stacked 1D profile for the batch. The profiles are then imported into the BASS Project software, by Paraskeva (<https://uk.groups.yahoo.com/neo/groups/astrobodger/links/all>). The wavelength calibrations of the profiles are confirmed and/or corrected and the profiles are scaled consistently. Figure 2 provides an example of a spectral profiles as displayed in BASS of the Be shell star omicron Andromedae in the region of the H α line extending to the Helium 6678 line, which is considerably broadened, reflecting the rapid rotation of the star. Prominent are telluric lines in the vicinity of the H α line. The profiles also display the two wings of the H α line separated by the deep central absorption feature. The continuum is rectified and normalized to 1.0. The top profile in Figure 2 illustrates a condition in which the R wing is more intense than the V wing. This was not always the case, as illustrated in the bottom profile from October 28, when the V wing was more intense. These are single ten-minute exposures.

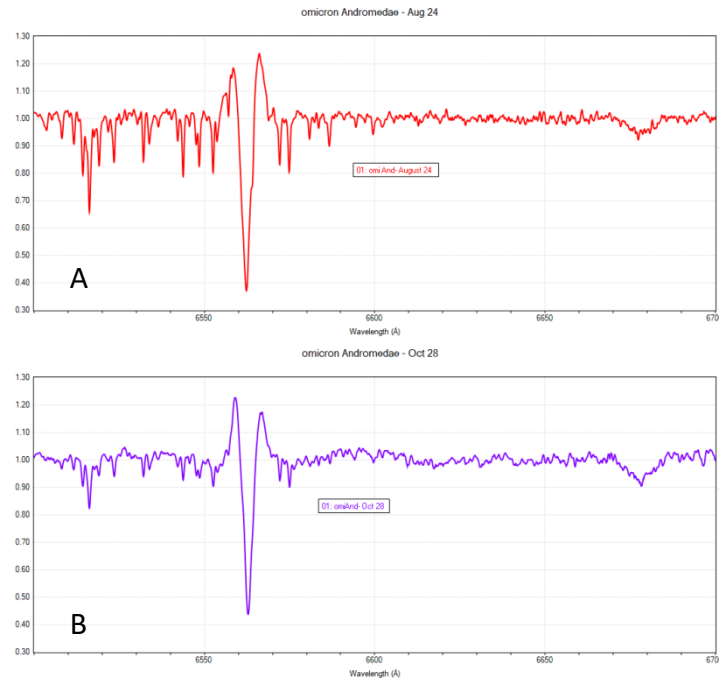


Figure 2. Calibrated spectra of the Be ‘shell’ star omicron Andromedae. Profile A shown in red is an example from August 28 when the R wing was more intense than the V wing; in profile B from October 28 the V wing was more intense.

The BASS measurement tool was used to convert important features of the H α line and the He I 6678 line to data values. In the case of a shell star as shown in Figure 2, the peak intensity of the V and R wings of the H α line, the minimum intensity of the central depression, and the minimum intensity of the He 6678 line were measured relative to the rectified continuum (normalized to 1.0). The values were then transferred into a spreadsheet for analysis.

Once sufficient data is accumulated, period analysis will be conducted using the proprietary software Peranso by Vanmunster (<https://www.cbabelgium.com/peranso/>). The software provides a collection of light curve and period analysis tools such as Lomb-Scargle, CLEANest, ANOVA, PDM and others.

3. Preliminary Results

We began collecting data in late August and will continue to collect data into the spring of 2024. Presented in this preliminary report are data from observations of the Be shell star omicron Andromedae (a multi-star system) whose profile is shown in Figure 2. Initial results indicate that variation does occur on a very short time frame as also reported by Briot et al. (2002). For example, observations on the night of September 25 (Figure 3) suggest a pattern of variation during the session. There is a general downward trend in the relative intensity of the V wing while the R wing maintains a relatively constant value. Thus, the V/R ratio decreases over the course of the session. The statistical significance of these patterns is yet to be determined.

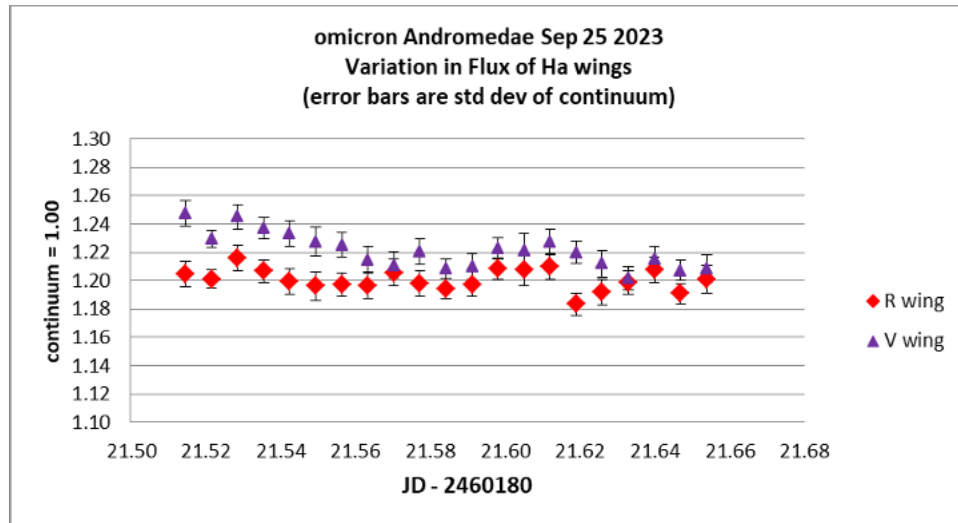


Figure 3. The relative intensity of the V and R wings of the H α line during the night of September 25, 2023. Each data point represents a ten-minute exposure; exposures follow one after another with no break. Error bars are one standard deviation of the continuum.

Variation was also observed over a longer time frame. Presented in Figure 4 is the set of observations of the H α wings from late August to early November, 2023. There appears to be a somewhat sinusoidal pattern with a possible period of about 30 to 40 days.

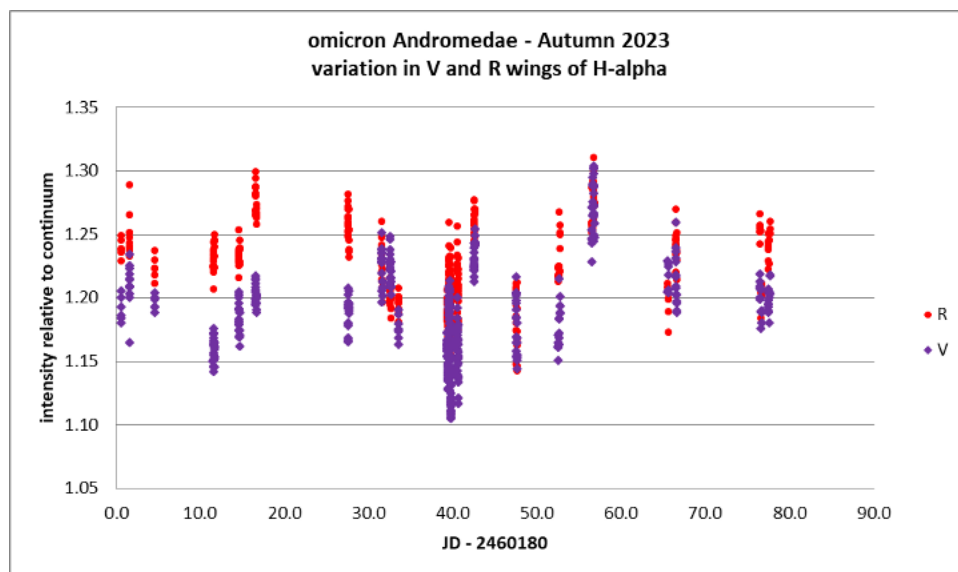


Figure 4. Observations of the relative intensity of the V and R wings of the H α line. Each data point represents an individual exposure varying in duration from four minutes to ten minutes.

Notice also that the V/R ratio changes over time, with the V wing usually less intense than R, but with occasional reversal. This relationship is shown more clearly in Figure 5 in which the V/R ratio is plotted. Gaps in the data make interpretation difficult.

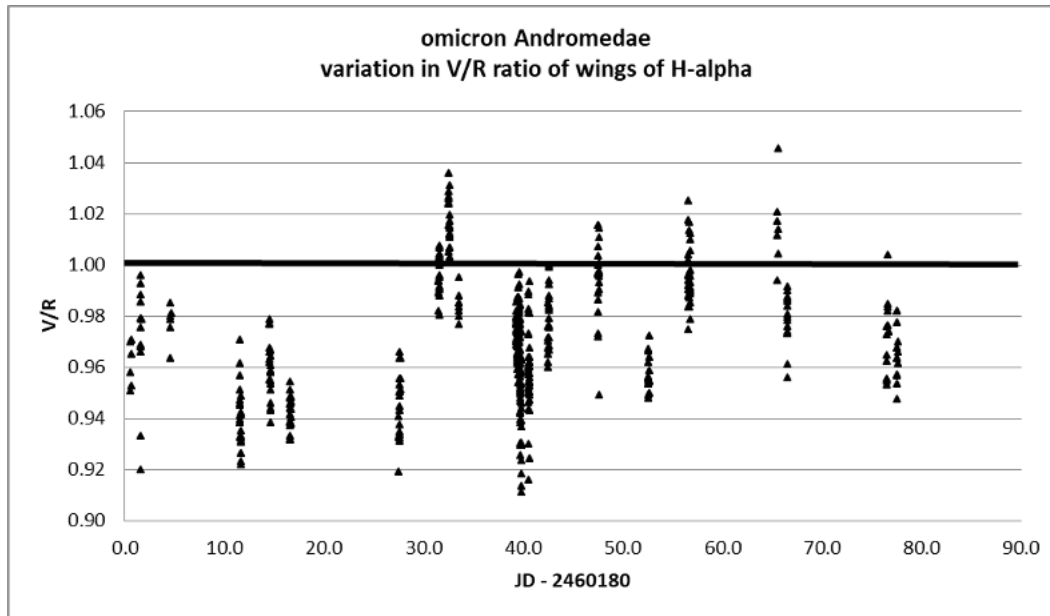


Figure 5. V/R ratio of the wings of the $H\alpha$ line during the fall, 2023, for omicron Andromedae.

A more complete presentation of results will appear in our final report to be submitted for publication once all data has been collected and analyzed. That analysis will include variation in the features of the $H\alpha$ line as well as the Helium 6678 line and period estimations.

4. Conclusions

It is too soon to draw conclusions, especially about the cause of the variation. We only can say that it is encouraging and gratifying that amateurs with small telescopes, and in some cases using DIY spectroscopes, can do legitimate science ... literally in their own backyards. More data will be collected, and additional Be stars will be targeted before we are through.

References

- Briot, D., Chauville, J., and Guerrero, G. 2002, in ASP Conference Series, Vol. 259. pp. 250-251.
- Percy, J. 1986. *Observations of Rapid Variability in Be Stars* in Physics of Be Stars, 92nd Colloquium of the IAU, Boulder, CO August 1986, Cambridge Univ. Press.
- Porter, J. and Rivinius, T. 2003, PASP, 115, 1153
- Rivinius, T., Stefl, S., and Baade, D. 2006, A&A, 459, 137
- Rivinius, T., Carciofi, A., and Martayan, C. 2013, A&A Review, Vol. 21, no 69

Abrupt Periodic Pulsation Resumptions in Deneb

Joyce A. Guzik¹, Helmut A. Abt², Jason Jackiewicz³, and Brian Kloppenborg⁴

¹Los Alamos National Laboratory, Los Alamos, NM 87545; joy@lanl.gov

²Kitt Peak National Observatory, Box 26732, Tucson, AZ 85712

³New Mexico State U., Las Cruces, NM 88003

⁴AAVSO, 185 Alewife Brook Parkway, Suite 410, Cambridge, MA 02138

Subject Keywords

AAVSO International Database; Photometry, CCD; Radial Velocities, Alpha Cygni Variables; stars: individual (alpha Cyg)

Abstract

Deneb (α Cygni) is a bright (V magnitude 1.25) blue-white supergiant (spectral type A2 Ia) which shows variability in both radial velocity and photometric measurements. H. Abt reviewed radial velocity measurements by Paddock (1935) using the Lick observatory 36-inch telescope spectrograph during 1927-1935. Abt noticed resumptions of pulsations with a dominant quasi-period of around 12 days that occur at intervals of around 70 days, and damp out after a few cycles. These resumptions appear to happen at arbitrary phase. Perhaps another event like this was captured in a shorter series of radial velocity measurements by Abt in 1956. We examined subsequent radial velocity and photometric data available in the literature, along with photometric measurements by the TESS spacecraft and V-magnitude observations by AAVSO observers. We find some evidence for periodic resumptions of larger-amplitude pulsations in these data. However, longer contiguous data sets combined with more frequent sampling are needed to confirm this periodicity in resumption of pulsations, and to help answer many more questions about Deneb and the α Cygni variables.

1. Introduction

Despite being one of the brightest stars of the Northern Hemisphere sky (apparent visual magnitude 1.25), surprisingly little is known about Deneb (Diodati 2019). Deneb is the prototype of the α Cyg variables (Abt 1957, van Genderen et al. 1989), which show small-amplitude (~ 0.1 mag) irregular variations. Deneb varies in both radial velocity and brightness with dominant period around 12 days (Paddock 1935). Its effective temperature is 8500 K and spectral type A2 Ia (Schiller and Przybilla 2008). Deneb's current mass is estimated at about 20 solar masses. Deneb's mass-loss rate is 3×10^{-7} solar masses/year (Schiller and Przybilla 2008), 10 million times higher than that of the Sun, amounting to two Mercury masses per year.

The distance to Deneb is controversial (see, e.g., Diodati 2019, Byrd and Machholz 2023). Hipparcos parallaxes have large uncertainties, and instead the distance to Deneb of 2600 light years is based on the distance to stars in the Cygnus OB7 association, assuming that Deneb is a

member. Deneb's luminosity using this distance is around 200,000 solar luminosities (Schiller and Przybilla 2008). Note that a more definitive Gaia parallax for Deneb is unavailable (as yet) because Deneb is so bright that it would saturate Gaia's detectors (Byrd and Machholz 2023). Deneb's radius, based on its luminosity and temperature, is 200 solar radii. If Deneb were at the location of the Sun, its surface would nearly reach Earth's orbit, since the Earth-Sun distance is 212 solar radii.

Deneb's age and evolutionary state are also not known—it may be on its first crossing of H-R diagram on its way to becoming a red supergiant before reaching core helium-burning phase, or it may be on its way back toward the blue. According to Abt et al. (2023), there is evidence that α Cyg stars are on their first crossing of the HR diagram, because at least one such star (6 Cas) is a member of the Cas OB5 association (Bartaya et al. 1994). Gorlova et al. (2006) derived a young age of 4-6 Myr for that association. However, Saio et al. (2013) find, using stellar evolution and pulsation modeling, that α Cyg-like pulsations are excited only after the star has been a red supergiant. On the other hand, they note that the N/C and N/O abundance ratios for Deneb are more consistent with stars that have not yet reached the red supergiant stage.

Deneb's projected rotational velocity ($v \sin i$) is only around 20 km/sec, but interferometric measurements show 2% asymmetry in the disk, indicating that we could be observing Deneb close to pole-on (inclination 30° with respect to our line of sight), and that the rotation velocity could be as high as 35% of breakup (Aufdenberg et al. 2008). However, there are ambiguities in the data, and more work is required to confirm the fast-rotator interpretation (Chesneau et al. 2010).

Deneb is located among the Luminous Blue Variables in the H-R diagram (Humphreys and Davidson 1994), but doesn't show LBV outbursts, i.e., abrupt large mass ejections and excursions to the red in the H-R diagram that occur decades apart (see, e.g., Guzik and Lovekin 2012). Deneb's low amplitude variability, however, may have the same origin as LBV microvariations.

2. Radial Velocity Measurements

Abt et al. (2023) re-examined an extensive series of radial velocity measurements made by Paddock (1935; see also Lucy 1976) using the Mills three-prism spectrograph on the 36-inch Lick Observatory refractor from 1927 through 1935. Abt et al. notice that the radial velocities show abrupt resumptions of larger-amplitude pulsations which are uncorrelated with pulsation phase. They mark several instances where these events occur at points A, B, C, and D (Fig. 1).

Abt et al. (2023) also notice that the time interval between points A to B and between points B to C is around 70 days, and that the interval between C and D is a multiple of about 70 days (see Table 1). Another abrupt amplitude increase may have been observed by Abt in 1956 (Abt 1957), labeled as point E in Figure 2. The data around point E were taken 25 years later than the Paddock data, but are not inconsistent with a multiple of around 70 days.

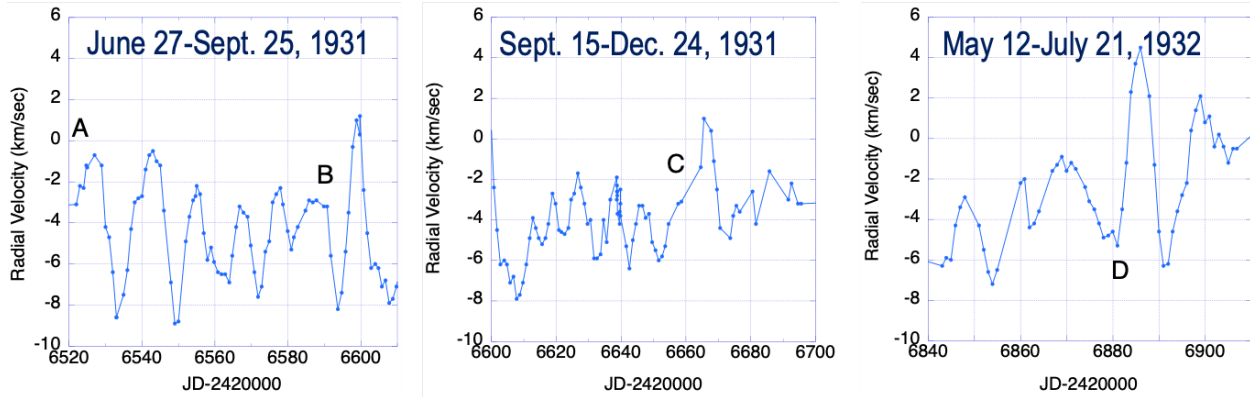


Figure 1. Deneb Radial velocity vs. Julian date from Paddock et al. (1935). Instances of abrupt resumption of larger amplitude pulsations are marked by letters A, B, C, and D.

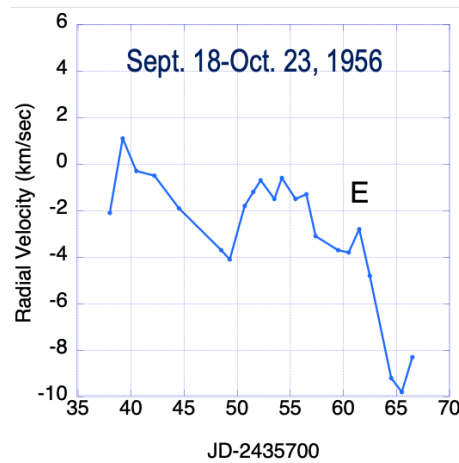


Figure 2. Deneb radial velocity vs. Julian Date from observations by Abt (1957). Another such resumption of larger amplitude pulsation may have occurred near the date labeled at E.

Table 1. Time intervals between radial velocity points A through E in Figures 1 and 2.

Point	Julian Date	Interval (days)	Possible Multiple
A	2426517 ± 5		
		75 ± 5	75 days x 1
B	2426592 ± 0.5		
		69 ± 4	69 days x 1
C	2426661 ± 3		
		220 ± 4	73 days x 3
D	2426881 ± 0.5		
		8866 ± 1	71 days x 125
E	2435747 ± 1		

3. Later Deneb Time-Series Data

The referee of Abt et al. (2023) requested that we examine more recent archival data in photometry and radial velocity to search for additional instances of abrupt pulsation

resumptions. The referee in particular suggested Transiting Exoplanet Survey Satellite (TESS, Ricker et al. 2015) data and Hipparcos spacecraft (van Leeuwen 1997) data. Our search also turned up additional ground-based observations.

Parthasarathy and Lambert (1987) observed Deneb using the 2.7-meter reflector and coude' spectrometer at McDonald Observatory between March 1, 1980 and November 26, 1982. Because Deneb is so bright they could conduct either daytime or night-time observations. The radial velocity measurements derived from these observations (Figure 3, 213 points) show a few possible large excursions. The A-B interval is 66 days. The B-C interval is 412 days = 6 x 69 days.

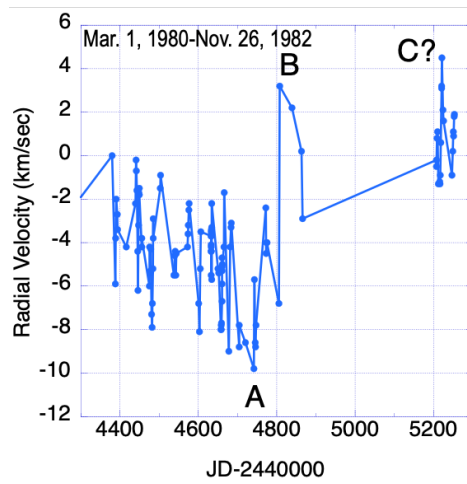


Figure 3. Deneb radial velocity vs. Julian Date from Parthasarathy and Lambert (1987).

The Hipparcos photometry is too sparse to identify abrupt brightness excursions. Data points exist for only 30 distinct days over four years, March 3, 1990 through February 23, 1993. However, Hipparcos spacecraft data were used to discover 32 α Cyg variables (Waelkens et al. 1998).

Richardson et al. (2011) present Deneb Strömrgren v-magnitude photometry and radial-velocity measurements from spectroscopic observations taken April 1997 through December 2001. The spectroscopy was done using a 1-meter telescope and echelle spectrograph at Ritter Observatory, and the photometry taken using the 0.75-meter Four College Automated Photoelectric Telescope (FCAPT). There are 368 photometry data points, and 281 radial-velocity data points. We plotted their data in Figure 4 and labeled the largest excursions from the mean magnitude and radial velocity by points A, B, C, and D. Point C seems to be near an excursion in both photometry and radial velocity. We find three nearly equal intervals between these events of 447-448 days. These intervals would not be inconsistent with six 75-day intervals or seven 64-day intervals. The data are too sparse to reliably identify or rule out pulsation resumption events between points A, B, C, and D.

Figure 5 zooms in on the Richardson et al. (2011) photometric data in Fall of 1998 and Fall of 1999 which have the most frequent coverage. The characteristic 12-day quasi-periodicity is evident in these light curves.

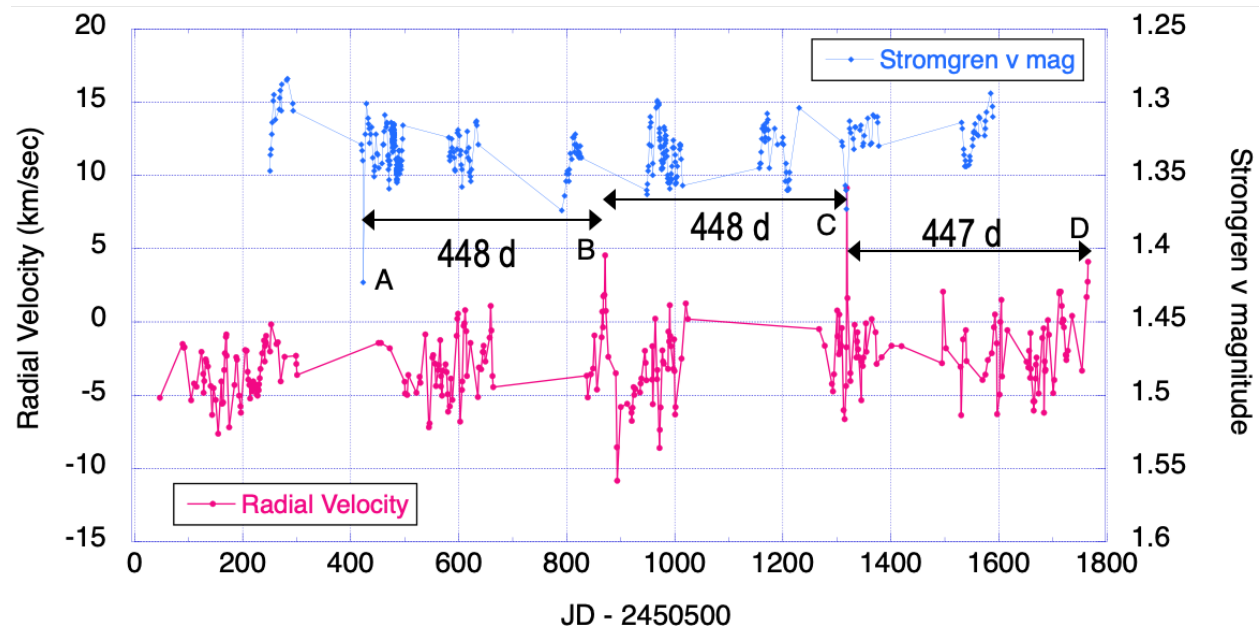


Figure 4. Deneb radial-velocity and photometry data from Richardson et al. (2011). Four large excursions were identified at A, B, C, and D, which are nearly equally spaced at 447-448 days.

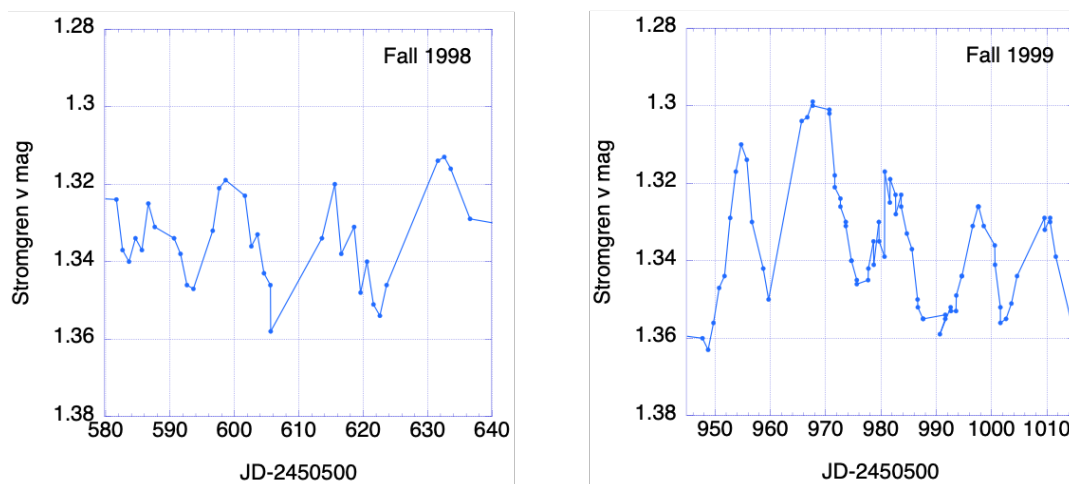


Figure 5. Zoom-in on Richardson et al. (2011) Deneb photometry from Fall 1998 and Fall 1999, showing variability with periodicity around 12 days.

The Mikulski Archive for Space Telescopes (MAST, <https://archive.stsci.edu>) contains High-Level Science Product (HLSP) light curves for Deneb in 2-minute cadence photometry taken during three 27-day sectors. After removing a few outlying points, we plotted the normalized Simple Aperture Photometry (SAP) flux measurements vs. time in Figure 6. Note that we did not use the Pre-Data Conditioned SAP fluxes, in which long-period trends, including some pulsations, have

been smoothed out. These observations show irregular pulsations during Sector 41 and resumption of higher amplitude pulsations with an approximate 12-day period during Sector 55, continuing into Sector 56.

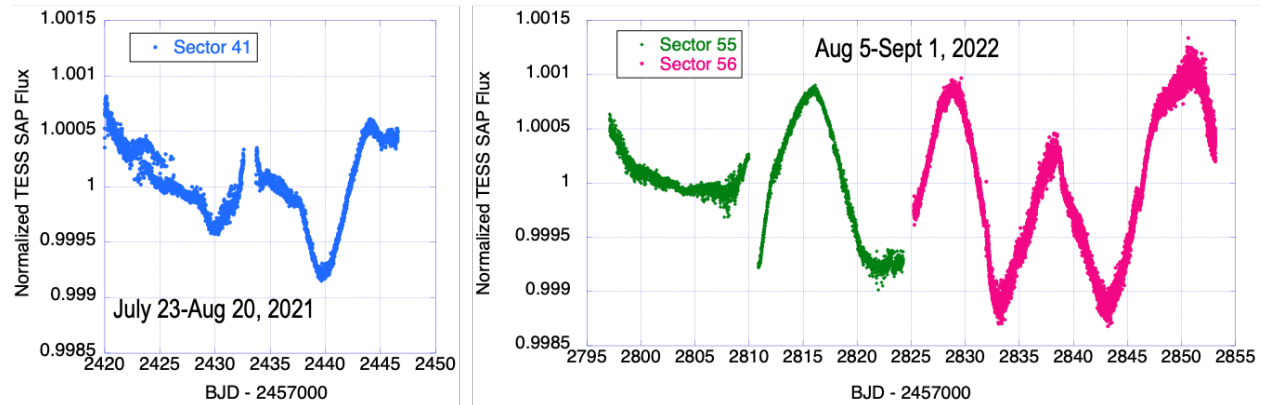


Figure 6. Deneb light curves from TESS data during Sectors 41, 55, and 56. Large-amplitude pulsations appear to resume during Sector 55 at around day 2810 after BJD 2457000.

4. Recent Deneb AAVSO Data

We also examined the American Association of Variable Stars International Database (AID, Kloppenborg 2023) for data on Deneb, and were pleased to find a recent extensive set of V-band photometry taken by ten different observers during the past two years, June 16, 2021–June 15, 2023, comprising 128 data points. The AAVSO observer codes are CTOA, FBA, FXJ, MPFA, BVE, DFR, BWU, GMV, GTIA, and WIG. Figure 7 shows V magnitude vs. time and Figure 8 zooms in on two time spans with the densest coverage, in which Deneb’s 12-day quasi-periodicity can be discerned. There appears to be at least one large excursion from mean magnitude around day 200 after JD-2459300, but the time-series coverage is a little too sparse to reliably identify the date of additional abrupt amplitude increases.

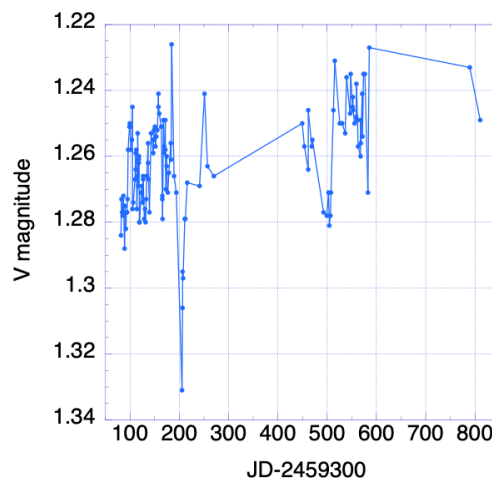


Figure 7. Deneb V magnitude vs. Julian Date from the AAVSO International Database (AID). These data were taken between June 16, 2021 and June 15, 2023.

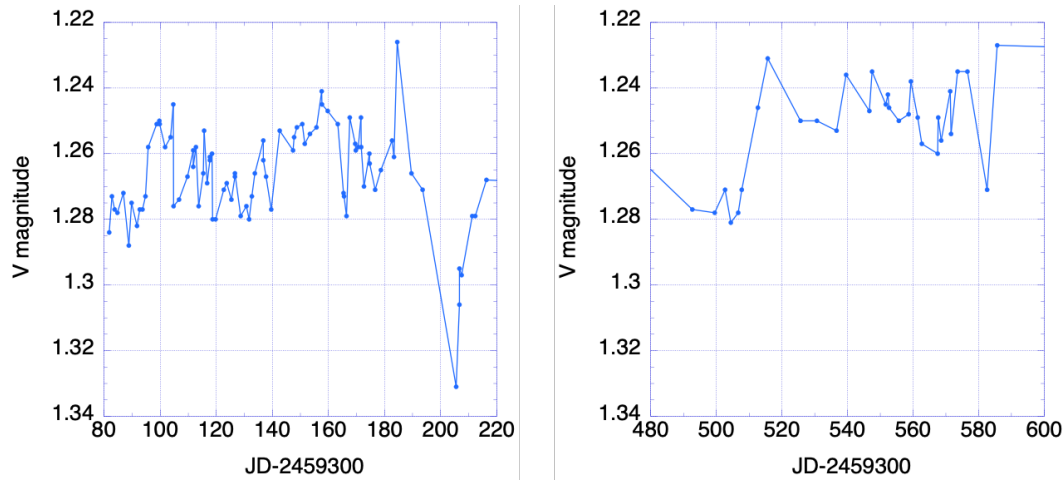


Figure 8. Zoom-in on portions of Deneb AID data showing some large excursions in brightness and approximate 12-day pulsation periods.

5. Conclusions

We have many questions about Deneb's variability that additional observations may help to answer: Can we confirm that pulsation resumptions occur at around 70-day intervals, and how precise are these intervals? Do these resumptions occur at an arbitrary phase in the 12-day dominant quasi-period? Do they occur at the same time in light curve and radial velocity data? Are there additional radial or non-radial pulsation modes with well-defined periods and amplitudes? Note that Lucy (1976) reports finding many periodicities in a Fourier analysis of the Paddock (1935) data, attributed to nonradial pulsations, but our analysis did not find any significant periods.

The available TESS time series is too short/discontinuous and the AAVSO ground-based photometry data points are a little too infrequent to answer these questions definitively. However, several additional 27-day sectors of TESS data, preferably contiguous, as well as AAVSO time series data with around one data point per night for several consecutive 70-day intervals may be possible to obtain. Perhaps multi-site observations of Deneb using the Bright Star Monitor network would be useful. Perhaps it is also possible for observers to measure radial velocities to within 1-2 km/sec with cadence around one data point per night using spectroscopy as did Paddock the early 1930s. It would also be worthwhile to investigate other α Cygni variables to see whether they show any similarities in behavior.

Deneb inspires many questions and challenges for stellar modeling:

- What is the evolutionary state of Deneb?
- What is the cause of its pulsations with quasi-period 12 days? Why 12 days?
- Why do the large-amplitude pulsations damp out and resume, perhaps every 70 days?
- Are there multiple pulsation modes occurring simultaneously?
- Does Deneb have properties in common with other α Cygni variables?

- What distinguishes Deneb from the Luminous Blue Variables in the same part of the H-R diagram?

6. Epilogue

During the question-and-answer session following our November 4 AAVSO Annual Meeting talk, AAVSO Director Brian Kloppenborg offered unpublished photometric data on Deneb from the Solar Mass Ejection Imager taken from 2003 through 2011 (see, e.g., Jackson et al. 2004, Clover et al. 2011). The spacecraft was in a Sun-synchronous polar orbit with a 102-minute period. While the spacecraft was designed to measure solar coronal mass ejections (CMEs), it also observed almost every bright ($V < 6$) star. It had three cameras equipped with non-linear optics that provided each camera with a 3×120 degree field-of-view of the sky.

After the meeting, Brian located these data for Deneb (Figures 9 and 10). These data require further processing to remove camera-to-camera zero-point offsets, angle-dependent flux loss, and other spacecraft-related noise and artifacts. The angle-dependent flux loss causes the ~ 100 -day curvature or changes in slope. The light-curve cadence is around 102 minutes (once per spacecraft orbit), and the time series is long enough that it may be definitive to answer some of our questions about Deneb. Developing a processing pipeline for the SMEI data will be valuable for other variable-star projects since SMEI collected light curves for around 6500 bright stars.

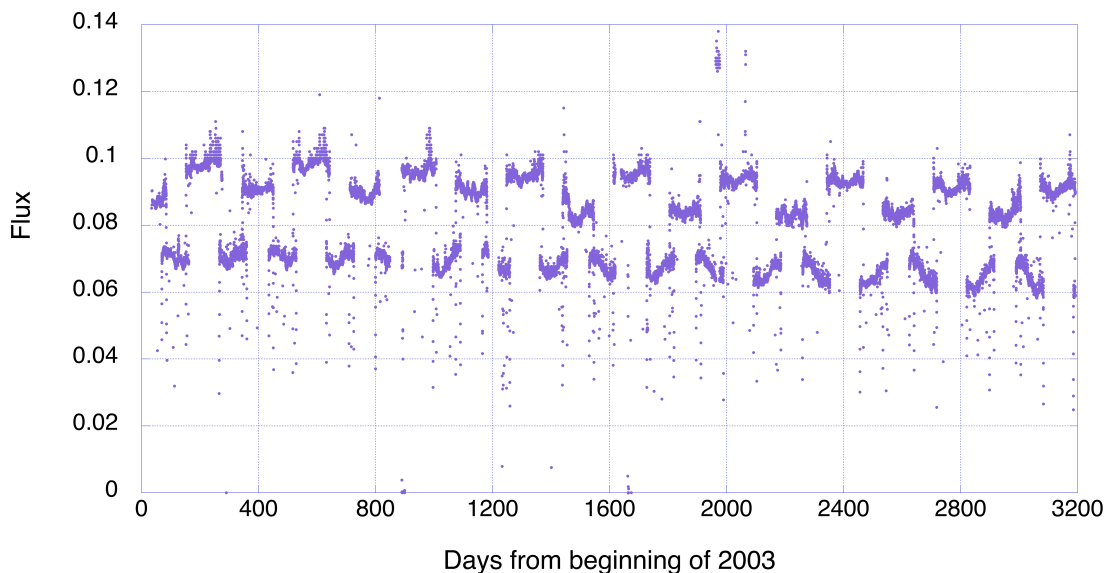


Figure 9. Deneb time-series uncorrected data from Solar Mass Ejection Imager (Kloppenborg, private communication).

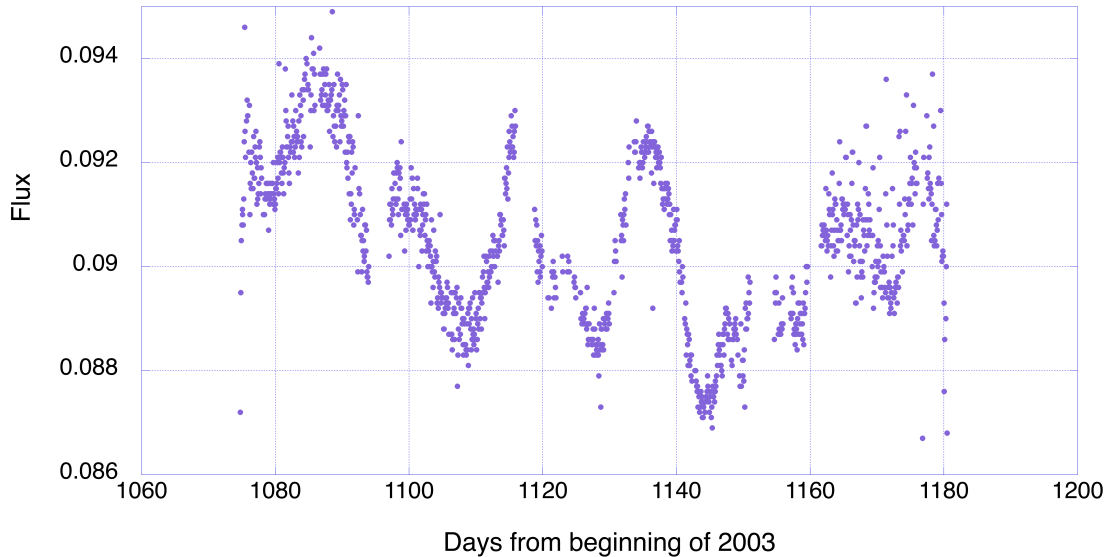


Figure 10. Zoom-in on portion of uncorrected Deneb data from Solar Mass Ejection Imager.

We found that there are 101 α Cygni variables listed in the AAVSO Variable Star Index (VSX, <https://www.aavso.org/vsx/>, Watson et al. 2006) database. These include several bright well-known stars, for example: Rigel and Saiph at the lower left and right corners of Orion; Alnilam, the star in the center of Orion’s belt; and Aludra, the star at the tail of Canis Major. This database will be a useful starting point for comparing Deneb to other α Cyg variables and motivating additional data searches and observations.

Acknowledgements

This research made use of data from the Mikulski Archive for Space Telescopes (MAST). We acknowledge with thanks the variable star observations from the AAVSO International Database contributed by observers worldwide and used in this research. We thank Jos de Bruijne from the ESA Hipparcos support center for obtaining α Cyg photometry from the Hipparcos archive. This collaboration was facilitated by a Los Alamos National Laboratory Center for Space and Earth Sciences grant XX8P ASF2. J.G. acknowledges support from Los Alamos National Laboratory, managed by Triad National Security, LLC for the U.S. DOE’s NNSA, Contract #89233218CNA000001. We thank John Dragon for carefully proofreading this manuscript.

References

- Abt, H.A. 1957, The Variability of Supergiants, *ApJ* 126, 138
- Abt, H.A., Guzik, J.A., and Jackiewicz, J. 2023, The Abrupt Resumptions of Pulsations in α Cygni (Deneb), *PASP*, <https://doi.org/10.1088/1538-3873/ad1118>
- Aufdenberg, J.P., et al. 2008, Limb Darkening: Getting Warmer, in *The Power of Optical/IR Interferometry: Recent Scientific Results and 2nd Generation Instrumentation*, ed. A. Richichi, F. Delplancke, F. Paresce, and A. Chelli, ESO Astrophysics Symposia, ISBN 978-3-540-74253-1. Springer, p. 71

- Bartaya, R.A., Chargeishvili, K.B., Chentsov, E. L., and Shkhagosheva. Z.U. 1994, Hypergiant 6 Cas and association Cas OB5, *Bull. Special Ap. Obs.*, 38, 103
- Byrd, D. and Machholz, D. 2023, <https://earthsky.org/tonight/deneb-how-do-astronomers-know-distances-to-stars/>
- Chesneau, O., et al. 2010, Time, spatial, and spectral resolution of the Ha line-formation region of Deneb and Rigel with the VEGA/CHARA interferometer, *A&A* 521, A5
- Clover, J.M., et al. 2011, Epsilon Aurigae light curve from the Solar Mass Ejection Imager, AAS Meeting Abstracts, *B.A.A.S.* 217, 257.02
- Diodati, M. 2019, <https://medium.com/amazing-science/deneb-a-supergiant-200-000-times-brighter-than-the-sun-36257f860f21>
- Gorlova, N., Lobel, A., Burgasser, A.J., et al. 2006, On the CO near-infrared band and the line splitting phenomenon in the yellow hypergiant ρ Cassiopeiae, *ApJ* 651, 1130
- Guzik, J. A. and Lovekin, C. C. 2012, Pulsations and Hydrodynamics of Luminous Blue Variable Stars, *Astron. Rev.*, 7, 3 (see also <https://arxiv.org/pdf/1402.0257.pdf>)
- Humphreys, R. and Davidson, K. 1994, The Luminous Blue Variables: Astrophysical Geysers, *PASP* 106, 1025-1051
- Jackson, B.V., et al. 2004, The Solar Mass-Ejection Imager (SMEI) Mission, *Sol. Phys.* 225, 177
- Kloppenborg, B.K. 2023, Observations from the AAVSO International Database, <https://www.aavso.org>
- Lucy, L.B. 1976, An Analysis of the Variable Radial Velocity of Alpha Cygni, *ApJ*, 206, 499
- Paddock, G.F. 1935, Spectrographic Observations of Alpha Cygni, *Lick Obs. Bull.* 17, No. 472, 99
- Parthasarathy, M. and Lambert, D.L. 1987, Alpha Cygni as a Radial Velocity Variable, *J. Astrophys. Astron.* 8, 51
- Richardson, N.D., Morrison, N.D., Kryukova, E.E., and Adelman, S.J. 2011, A five-year spectroscopic and photometric campaign on the prototypical α Cygni variable and A-type supergiant star Deneb, *AJ* 141, 17
- Ricker, G.R., et al. 2015, Transiting Exoplanet Survey Satellite, *Journal of Astronomical Telescopes, Instruments, and Systems*, Volume 1, id. 014003
- Saio, H., Georgy, C., and Meynet, G. 013, Evolution of blue supergiants and α Cygni variables: puzzling CNO surface abundances, *MNRAS* 433, 1246-1257
- Watson, C.L., Henden, A.A., and Price, A. 2006, The International Variable Star Index (VSX), Proceedings of the Society for Astronomical Sciences Annual Symposium, Vol. 25, p. 47 <https://ui.adsabs.harvard.edu/abs/2006SASS...25...47W>
- Waelkens, C., et al. 1998, Study of an unbiased sample of B stars observed with Hipparcos: the discovery of a large amount of new slowly pulsating B stars, *A&A* 330, 215
- van Leeuwen, F., et al. 1997, The HIPPARCOS mission: photometric data, *A&A* 323, L61–L64
- van Genderen, A.M., et al. 1989, Light variations of massive stars (alpha Cygni variables). IX., *A&A Supplement Series* 79, 263-282

Finding Cool Companions to Pulsating Variable Stars with Infrared Spectroscopy

Eric G. Hintz, Scott G. Call, and Timothy D. Morrell

Brigham Young University, Department of Physics & Astronomy, Provo, Utah, 84602, USA;
hintz@byu.edu

Subject Keywords

Techniques: spectroscopic; stars: variable: Cepheids; stars: variable: RR Lyrae; stars: variable: delta Scuti; infrared: stars; stars: individual (IO UMa, DQ Cep, HD 187615, HN Dra, V927 Her, IT Dra)

Abstract

It is well known that many stars are part of binary systems. Some of these are seen as eclipsing binaries. Others can be found in the residuals of an (O-C) diagram, or from shifts in the radial velocity of the primary star. In our current research efforts, we are using another method to look for cool companions around a wide variety of pulsating variables. This includes the stars of the instability strip such as δ Scuti, RR Lyrae and Cepheid variables, plus the hotter beta Cephei stars. The presence of nearby companion stars can have an impact on the pulsations seen in the primary star, so it is important to find these companions. Knowing the full nature of the systems provides a better overall model.

We use the ARC 3.5-m telescope of the Apache Point Observatory in New Mexico to obtain near-infrared spectroscopy of a large sample of pulsating stars. The *TripleSpec* camera is used to acquire simultaneous data in the J, H, and K bands. Stellar atmospheric models are then used to find the best fit to the full spectrum based on temperature, surface gravity, and metal content. The model is subtracted from the data and the remaining light examined. We will present preliminary results from the overall survey and show examples from systems with known companions.

1. Introduction

Pulsating variable stars have a long history of providing astrophysical significant information. Perhaps the most famous is the Leavitt Law (Leavitt & Pickering 1912) that provides the relation between the period of pulsation and the absolute brightness of the star. Therefore, these pulsating stars are distance indicators. This has been applied to finding the distance to nearby galaxies such as M31, with one of the first reported of Cepheids in M31 coming from Hubble (1925). The Cepheid variables have since become a major rung in the distance ladder that scales the entire Universe.

Beyond being used as distance indicators, pulsating variable stars can give us a look inside a star. While we cannot see past the photosphere of a star, the field of asteroseismology allows

astronomers to use measured pulsations to map the interior structure of the star. Lastly, we often say that we can't see a single star evolve; that the changes are too slow. However, monitoring the times of maximum light for a given star over many years can lead to evidence of slow subtle changes. This is often seen in an O-C (observed minus calculated) diagram.

In all these research areas there is an assumption that the star is a single star. In the case of the Leavitt Law the additional star would add light to the system and lead to a misinterpretation of the distance. If a star being examined with asteroseismology has a companion, there can be gravitational driven modes that would not normally be excited in the primary star. This would again lead to a misinterpretation of the data. For O-C research the presence of a companion will be seen in the form of a sinusoidal change in the O-C diagram.

Our current research program is using near-infrared (NIR) spectroscopy to study pulsating stars in the instability strip. Given that cool companion stars give off more NIR light than they give off light in the optical range, it is more likely to find light from a companion star in this range. Here we will present an example of the process of looking for these faint, cool companion stars.

2. Observations and Results

2.1 Observations

Observations and reductions in the NIR are a little more complex than observations in the optical range. The night sky is bright in the NIR due to the temperature of our atmosphere and must be subtracted to find the information about the astrophysical target hidden underneath. This requires special designs in the camera system, especially for spectroscopic observations.

Our data were obtained using the Astrophysical Research Consortium (ARC) 3.5-m telescope at the Apache Point Observatory near Cloudcroft, New Mexico. The spectroscopic observations of target and calibration stars were secured with the *TripleSpec* NIR camera system. The *TripleSpec* system has a wavelength coverage of 0.95-2.46 μm with a resolution of $R=3500$ (Wilson et al. 2004). This provides coverage of the photometric J, H, and K bands. Observations are done as AB pairs with the star shifting between two positions on the slit of the spectrograph. Dithering the observations in this way allows for the subtraction of atmospheric emission lines and thermal background. In addition to the target stars, we also obtain spectra for calibration stars of spectral type A0V near in time to the target and in airmass. This allows for flux calibration and, more importantly, correction for the transmission of the atmosphere.

Our overall observing program has generated data on 108 unique pulsating stars. Many targets have single observations, but for a small sample of targets the observations cover the entire pulsation cycle. The data set currently consists of 12 Cepheids, 76 δ Scuti, 2 γ Doradus, 4 RR Lyrae, 1 Long Period Variable, 4 only listed as pulsators, and 10 eclipsing binaries with pulsating components (8 δ Scuti, 1 RR Lyrae, 1 unknown).

2.2 Reduction Methods

Data from the *TripleSpec* instrument was reduced using the *Triplespectool*. This package is a modified version of *Spextool* and details can be found in Cushing et al. (2004) and Vacca et al. (2003). The primary function of this process is to take the *TripleSpec* images and reduce them to a one-dimensional spectrum. Using the two positions of spectrum along the slit a telluric absorption correction can be done to remove the glow of the night sky from the data of interest. In Figure 1 the white vertical lines are telluric lines or in other words from the Earth's atmosphere. The white horizontal lines are the spectra of the target DQ Cephei (DQ Cep) at the two positions along the slit. The telluric lines must be subtracted out but are used to provide a wavelength calibration for the spectrum. In the lower portion of Figure 1 the white and black lines are the positive and negative flux levels after subtraction of the atmospheric lines. The data is acquired over multiple orders that must be summed together to produce the final spectrum. In Figure 2 orders 3 to 7 are shown in alternating green and white. This is the spectrum of DQ Cep before atmospheric and flux calibration.

In the data acquisition process an AOV comparison star is selected which is close in airmass to the target object and should be taken close in time. AOV stars provide fairly simple spectra with mainly hydrogen absorption lines, which can be modeled out. The AOV spectrum can then be used to flux calibrate the target spectrum. The resultant spectrum is given in units of F_λ or $\text{ergs/sec/cm}^2/\text{\AA}$ as shown in Figure 3 for DQ Cep.

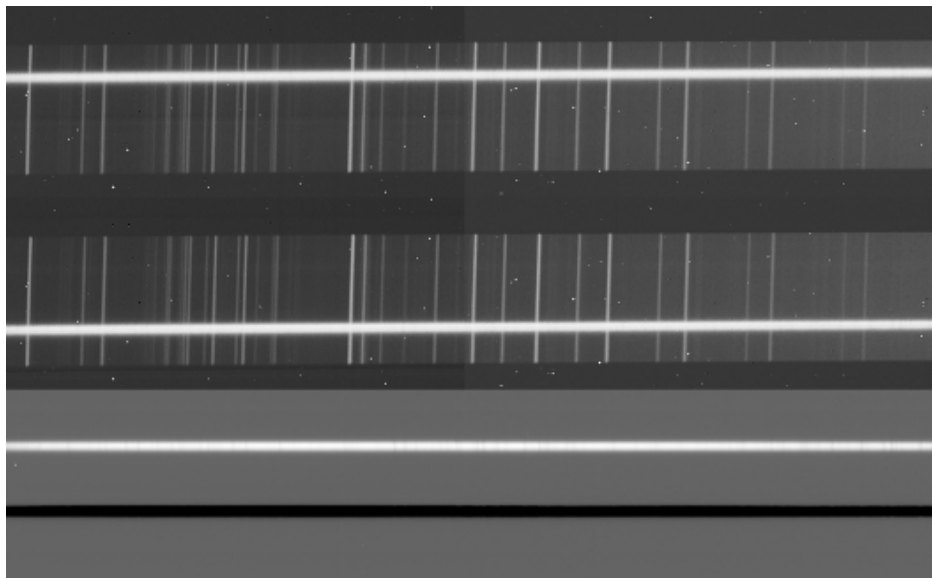


Figure 1. Raw Spectrum of DQ Cep. The top portion of the figure shows two spectra from two different positions along the slit. The lower portion of the figure shows the subtracted result with white being positive flux and black being negative flux.

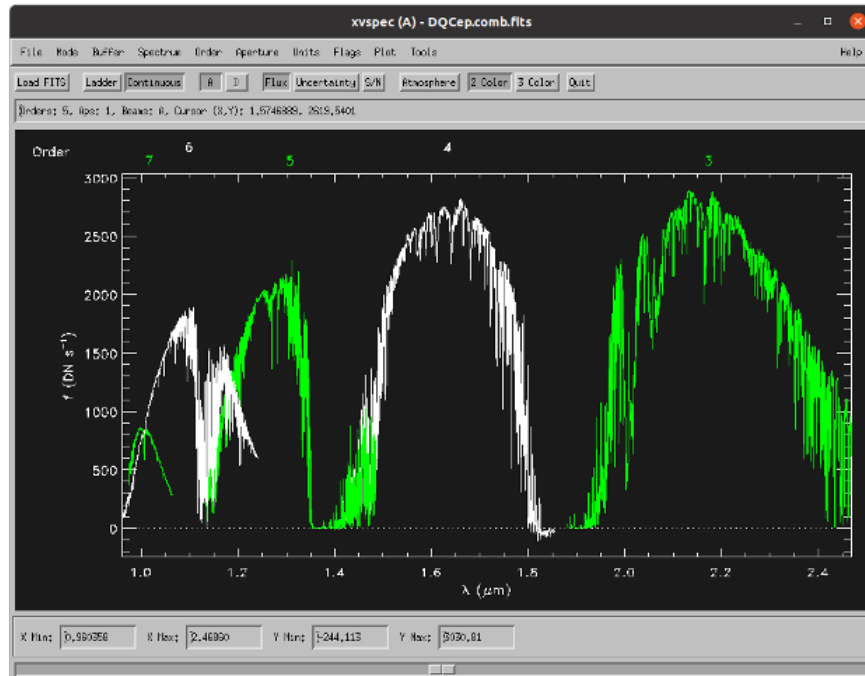


Figure 2. The data shown here is for DQ Cep before flux calibration and atmospheric correction. The alternating green and white area are different orders as labeled from 3 to 7 on the figure.

2.3 Results

To show the results for the different targets we include examples of different types of pulsating variables below. In each spectrum we note a number of features that each has in common. In Figure 3 we show the spectrum of DQ Cep which is a δ Scuti variable with a spectral type of F1 IV. Many of the features seen in DQ Cep are also seen in other targets that will be presented below. Each spectrum has three gaps that correspond to strong bands of water absorption in the Earth's atmosphere. The target data are unusable in these regions. On the left-hand portion of the spectrum are three deep absorption lines. These are three lines of the Hydrogen Paschen series that come from the $n=3$ energy level. In the region from $1.5 \mu\text{m}$ to $1.8 \mu\text{m}$ are a set of Hydrogen Brackett lines, related to the $n=4$ level. One additional Brackett line is in the right-side region at about $2.27 \mu\text{m}$. The overall shape of the curve is appropriate for a F1 spectral type.

In Figure 4 we show two additional examples of δ Scuti variables. V927 Herculis (V927 Her) on the top is a slightly cooler star than DQ Cep but the overall spectral structure isn't significantly different. On the bottom of Figure 4 is a spectrum of IT Draconis (IT Dra). IT Dra is much closer to the blue edge of the instability strip and shows strong Paschen lines. In Figure 5 we show the spectrum for the γ Doradus variable HD 817615 in the upper panel. This star is listed as an A3 star, which would be similar to IT Dra from Figure 4. In the lower panel of Figure 5 is the spectrum of HN Draconis (HN Dra). This is suspected of being an RR Lyrae star with a period of 0.9004 days. It also has a spectral type of F2.

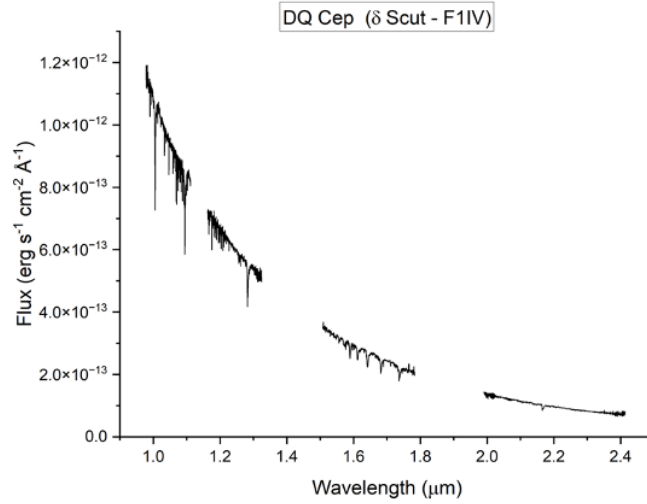


Figure 3. Spectrum of the δ Scuti variable DQ Cep in the NIR

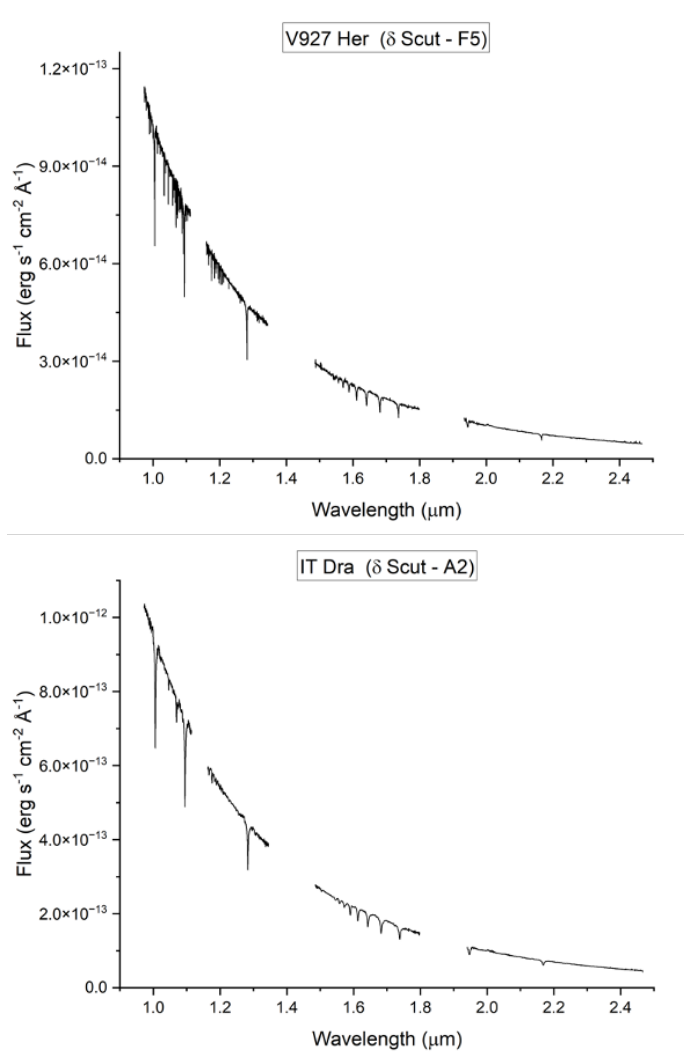


Figure 4. NIR Spectrum of V927 Her on the top and IT Dra on the bottom.

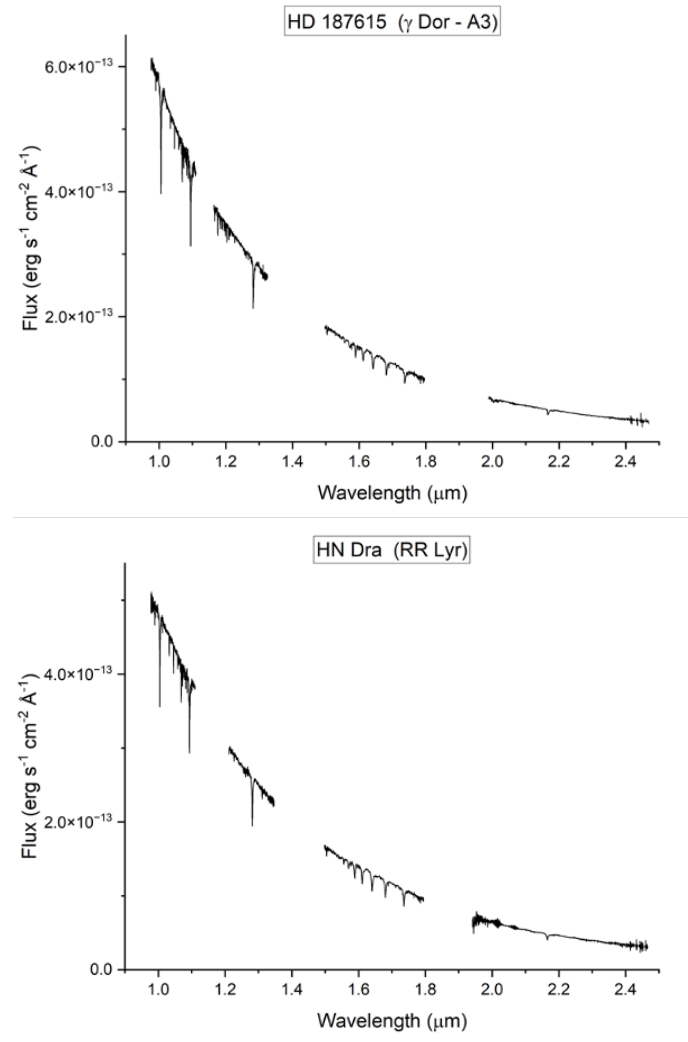


Figure 5. NIR Spectrum of the γ Doradus variable HD 187615 on the top and the RR Lyrae variable HN Dra on the bottom.

All stars discussed up to this point are reported as single stars and show no evidence of excess NIR light in the spectra. In Figure 6 we show the NIR spectrum of the eclipsing binary system IO UMa. Soydugen et al. (2013) report this system to have a primary star with a mass of $M_1 = 2.11 M_{\text{Solar}}$, a radius of $R_1 = 3.00 R_{\text{Solar}}$ and a temperature of 7800 K. The temperature implies a spectral type of roughly A3. The primary star is also pulsating with a frequency of 22.0148 d^{-1} . Models of the system from photometry and radial velocity measurements show the secondary star to be roughly a K4 star with $M_2 = 0.29 M_{\text{Solar}}$, $R_2 = 3.92 R_{\text{Solar}}$, and $T_2 = 4600 \text{ K}$. A quick look at Figure 6 might seem to be similar to IT Dra above. However, a careful examination will show that there is excess NIR light in this spectrum as shown in Figure 7.

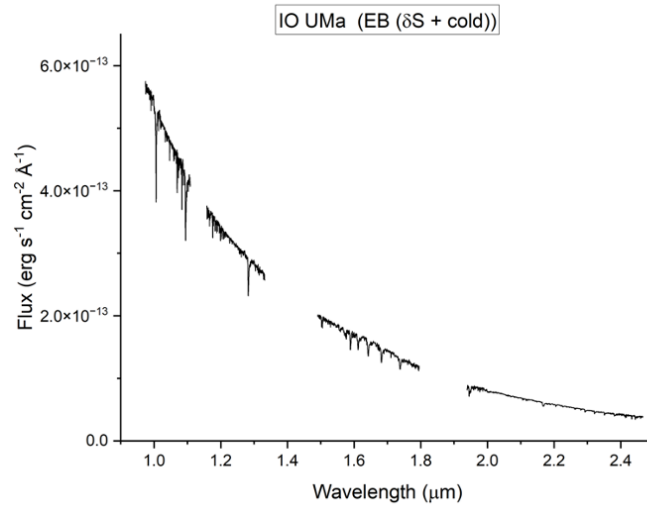


Figure 6. NIR Spectrum of the eclipsing binary system IO UMa.

In Figure 7 we show the spectrum of IO UMa along with two comparison stars HD 1662 and BE Lyncis (BE Lyn). These two stars are both A3 stars to match the model of Soydugen et al. (2013). While the spectra of HD 1662 and BE Lyn match each other with just an offset in their flux values, IO UMa clearly has a higher continuum level throughout most of the NIR region. Given the estimated surface temperature of the primary, 7800 K, we subtracted a spectrum generated by a stellar atmosphere model to obtain the residual spectrum found in Figure 8. This spectrum is in reasonable agreement with the estimated surface temperature of the secondary at 4600 K.

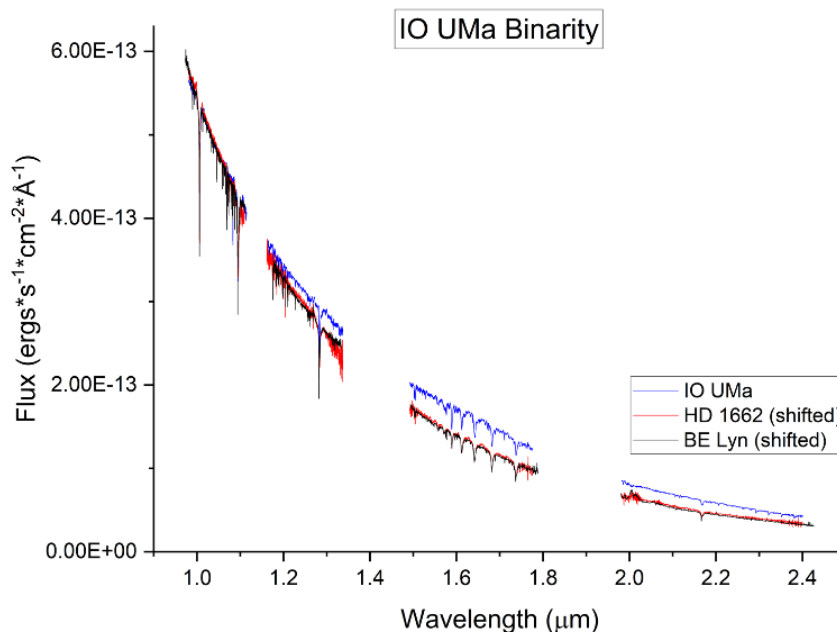


Figure 7. NIR Spectrum of the eclipsing binary system IO UMa compared to the A3 star HD 1662 and A3 star BE Lyn. The flux for the three stars was matched on the left-hand side of the graph. IO UMa clearly shows more light through the majority of the NIR region.

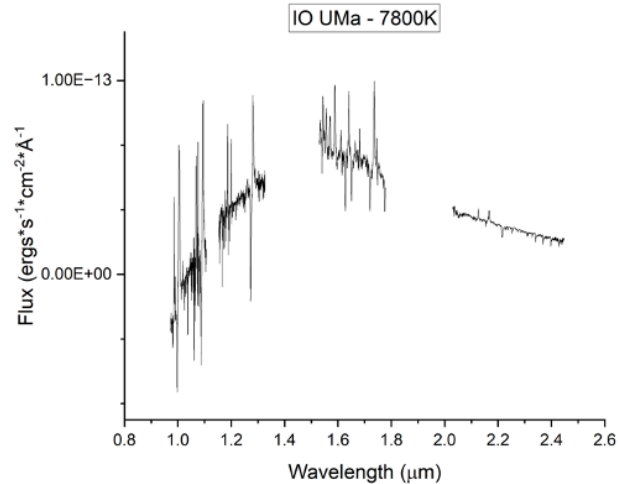


Figure 8. The residual spectrum of IO UMa after a 7800 K stellar atmosphere model was removed.

3. Conclusions

Here we have shown the application of NIR spectroscopy to the study of the pulsating variable stars of the instability strip. Using model atmospheres these spectra can be examined to determine surface temperature, surface gravity, and composition for these objects. In addition, the overall shape of the curve can be used to look for excess NIR light that might indicate the presence of a companion object.

In the case of IO UMa the residual spectrum after the removal of the primary star, confirms the model published by Soydugan et al. 2013. We are processing spectra from 9 additional systems with suspected cool companions to compare with photometrical determined models. These 10 systems are all eclipsing binary systems where there is clearly a companion. We will also be examining all our spectra to look for potential companions in systems that might not eclipse.

Acknowledgements

Based on observations obtained with the Apache Point Observatory 3.5-meter telescope, which is owned and operated by the Astrophysical Research Consortium. We also acknowledge the support of the Department of Physics & Astronomy of Brigham Young University.

References

- Cushing, M.C., Vacca, W.D., & Rayner, J.T. 2004, *PASP*, 116, 362
- Hubble, E. P. 1925, *The Observatory*, Vol. 48, 139.
- Leavitt, H. S. & E. C. Pickering. 1912, *Harvard College Observatory Circular*, 173, 1.
- Soydugan, F., Soydugan, E., Kanvermez, C., & Liako, A. 2013, *MNRAS*, 432, 3278.
- Vacca, W.D., Cushing, M.C., & Rayner, J.T. 2003, *PASP*, 115, 389
- Wilson et al. 2004, *SPIE*, 5492, 1295.

Using Photometric Imaging to Observe Variable Sources and Confirm Exoplanet Candidates

Hafsa Jamil¹, Michael Joner², and Oliver Hancock³

¹Rutgers, the State University of New Jersey, Department of Physics and Astronomy, 136 Frelinghuysen Road, Piscataway, NJ 08854-8019, USA; hij4@scarletmail.rutgers.edu

²Brigham Young University, Department of Physics and Astronomy, N283 ESC, Provo, UT 84602, USA; joner@byu.edu

³Brigham Young University, Department of Physics and Astronomy, N283 ESC, Provo, UT 84602, USA; oliver.t.hancock@gmail.com

Subject Keywords

Photometry, CCD; Exoplanet Transits; Calibration Frames

Abstract

Exoplanets have been studied by astronomers for numerous reasons, either to find habitable planets or to gain a broader understanding of the properties of planets. This paper will focus on experiences and skills acquired during a 10-week Research Experience for Undergraduates program at Brigham Young University (BYU) during the summer of 2023. New skills gained in this program included operating the different telescopes at the BYU West Mountain Observatory (WMO), learning about astronomical photometry (specifically transit photometry), planning observing sessions, selecting appropriate targets for different nights, processing the raw data frames, and using software such as AstrolmageJ (AIJ) to graph and evaluate transit candidates. Practice analysis was done using archival data of observed transits from previous projects at WMO. Potential exoplanet candidates were selected using TESS Input Catalog (TIC) from the Transiting Exoplanet Survey Satellite (TESS). Targets were selected based on the information on the TESS website, where it displays features of the potential targets such as transit depth, elevation, time of night, transit time, et cetera. These factors are important as they have to be viable for the team to observe them at WMO. Candidates identified were observed with the 0.91-m reflector telescope at WMO. Results are still ongoing, as more exoplanet candidates are being gathered. Multiple TIC candidates were ruled out if there wasn't a sufficient transit dip. Of the candidates that did transit, analysis was performed on them such as a chromaticity check. The anticipated analysis will help to identify false positives among the candidates and confirm the validity of the targets. Once this analysis is made, it can be concluded whether the targets collected are actual planets. This will not only make the transit method more viable for finding exoplanets, but it will also display how time series photometry can be applied to this type of research in the future.

1. Introduction

Photometry is the measurement of the light of any object. When applied to the astronomy field, it is used to measure and compare the luminosity of different types of celestial sources of light, such as exoplanets transiting their host stars, the nuclei of galaxies, and even smaller objects such as comets. A charge coupled device (CCD) is a microchip used to convert the light from the celestial target into an image. It does this by mapping out the high energy photons hitting the surface of the CCD, and the CCD then converts these photons to electron signals. From there, it will calculate the number of electrons to give the count. With the count, one can figure out all sorts of properties of our potential candidate, such as how much light it is generating. Usually this is done in a timely manner, with astronomers receiving multiple images of their targets for the night. For instance, when observing a transit, they would need to focus the telescope on that target for an hour or more so the image set can be captured for that specific target (Swanson, 2016). Astronomers can choose to focus on one target (perhaps when focusing on a galaxy), or multiple targets (when gathering exoplanet data sets). By the end of that interval, which can take more than a month and even years, the astronomers have gathered multiple data sets they can do photometry on.

When using this method with transiting exoplanets, there are a multitude of items to consider. There could be many red herrings that may cause a transit. Not all transit curves will be exoplanets, even if the data looks promising. When choosing exoplanet candidates, one must be mindful of the magnitude of the star. The higher the magnitude of the star, the dimmer it will be and the harder it will be to detect. It is also important to be mindful of the transit depth (which is essentially the size of the planet); if there is not much transit depth, then it is difficult to detect it on the transit graph. One must also be mindful of elevation and air mass. Elevations more than 30 degrees are ideal because then the telescope isn't observing through much of Earth's atmosphere, since at elevations less than 30 degrees, the telescope is observing through more atmosphere, which causes the stars to distort. This can cause any sort of model to break down and it becomes challenging to observe the targets. Once the targets are selected, the right ascension and declination can be put in the CCD program to begin observing.

1.1 False Positives: Exoplanets versus Eclipsing Binaries

When two stars orbit each other, and when the orbital plane is aligned with the line-of-sight to Earth, these systems are eclipsing binaries (EB) and they would cause a transit as one star blocks the light from the other star. There are many tests one could run to try to eliminate this red herring. One method that comes to mind is the chromaticity check. A planet does not emit any light as a star would. Astronomers use filters to allow certain wavelengths to pass through. For instance, the V band allows visible light to pass through. Throughout these different filters, if there is a different transit depth amount, then it likely fails the chromaticity check. This is because the stars are emitting two different colors, so when the smaller star transits the larger one, it will replace the light of the larger star with its own light. The difference in light will cause inconsistent transit depths since astronomers generate graphs with different light filters. Since a planet does

not give off light of its own, transits will be consistent across filters, and will pass the chromaticity check.

The shape of the graph is an interesting case; even though EBs usually cause a v shape, an exoplanet can cause it as well. Because of limb darkening, a star eclipsing another star can cause the light to drop at a steeper pace. This is what causes a sharp v shape light curve. This is typically a large drop in light that happens rather quickly, then it rises rapidly, marking the end of the transit. An exoplanet would decline the light straight away; however, the transit might be longer, cause light to decrease at a steadier pace. This results in a flat bottom graph, since a planet does not emit its own light (Deljookorani et al., 2020). Yet, this doesn't eliminate the possibility of an exoplanet when looking at transit curve graphs; it is possible that an exoplanet transited at the poles of the star rather than the center. This can also cause a v shaped graph since the exoplanet's transit is short and cause a steep decline in the target star's light. Because of this, it is important to be mindful of the shape of the graph; generally, graphs with flat bottoms are more favorable towards being an exoplanet candidate (Figure 1).

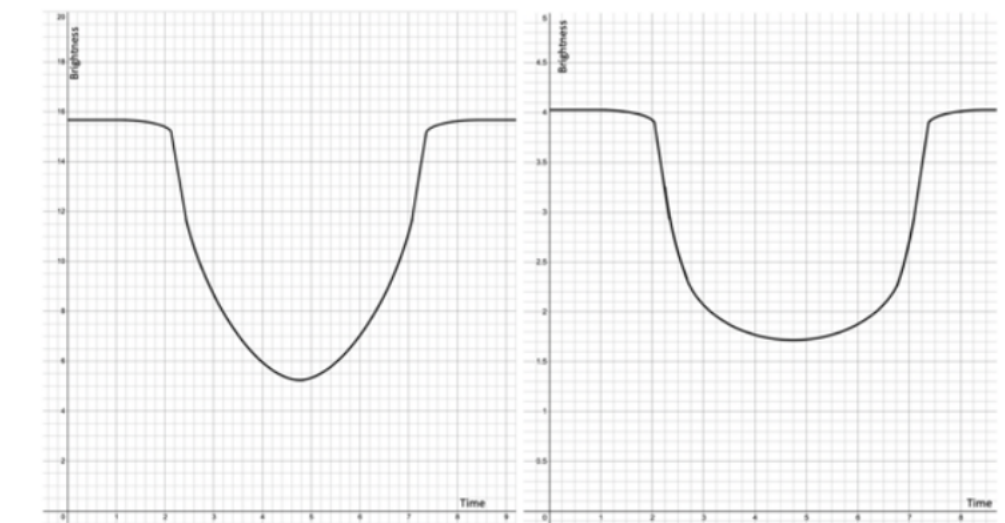


Figure 1. On the left, is the v shaped graph, in which the target candidate was ruled as an eclipsing binary. On the right is the bucket shaped, flat bottom transit graph. This could potentially be an exoplanet (Deljookorani et al., 2020).

2. Methods

All target observing was done at WMO, home to the 0.91-meter reflector telescope as well as the 0.32-meter reflector telescope. All exoplanet candidates were observed through the 0.91-meter telescope (Figure 2). The team at WMO followed an extensive step by step process on how to set up and close the telescopes for each observing night. All data received in the telescope is projected on the computers in the control room. From there, the images from CCD autopilot can be viewed. The team can also view the other programs, such as SkyX and the DFM control system/Maxim DL.



Figure 2. The 0.91-meter telescope, the main reflector telescope used to observe the candidates for this project.

2.1 Software used at West Mountain Observatory

There is a multitude of different software installed on the computers at WMO, as detailed in section 2. It is important to describe how each software functions and how important its role is in the project. First, the 0.91-meter telescope must be linked to the following software: the SkyX and the Maxim DL. This is done by pressing the “link to software” button in the CCD Autopilot 5 software. Then, when the telescope is connected, the DFM control system software can collect different types of calibration frames, such as bias, dark, and flat frames. These frames are important to collect as the light frames, which display the raw data of the celestial targets observed, will be very noisy initially. With a lot of dust particles and background noise, it will be hard to even see the target. Bias frames are with 0 length exposure; it measures the readout noise of the CCD. This is the bias level, an image with a bias level is always going to have a pixel count, even if the image is completely dark. Bias frames also help correct the thermal noise. A dark frame is taken with the shutter closed, so there is no light entering the telescope and camera. It reduces thermal noise when the device is cool (one of the protocols is to turn on the coolers for this reason). A flat frame is taken with a more diffuse light source (usually at twilight), and this is because flat frames react differently to light. A lot of flat frames are taken, then they are averaged, and the maximum pixel count is taken. Flat frames normalize the pixels on the detector by a certain amount and equalize all of the frame responses (Thomas, 2020). Once these frames are collected, then they can be used to reduce the light frames.

The program called the Sky X views which stars can currently be looked at (Figure 3). When a star is clicked on in the Sky X, the telescope can start tracking it. The telescope will be skewed towards that star. Zooming in on a patch of the sky will generate a purple box, and in that box is the star field, where one can choose a star to focus on. The team then can see how far the target is from the meridian by looking at the hour angles: positive means west, and negative means east. The Maxim DL software that is connected to the camera will show the image of the light frame of the specified celestial target. Then, the team can check the properties of this light frame by hovering over parts of the frame. The software will give the number of pixels in the light frame. From there, it will calculate the number of electrons in the pixels to give the count. With the count one can figure out all sorts of properties of the potential candidate, such as how much light it is generating, or if it's saturated or underexposed.

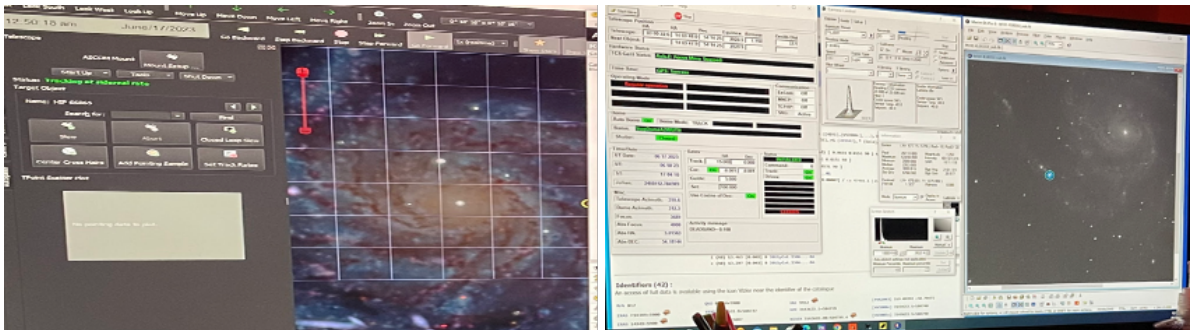


Figure 3. A sample of the Sky X and Maxim DL showing a raw light frame.

AstrolImageJ (AIJ) is the main photometry program (Figure 4). It is based on ImageJ with astronomy plug-ins. Data can be reduced in AstrolImageJ when one goes to calibrate the frames. First, the raw fits files are inputted into AstrolImageJ, then a click on the DP button will begin calibration. This involves subtracting the bias and dark frames and dividing the flat frames. This includes plate solving these frames, meaning that the celestial coordinates according to the SIMBAD database will be attached to these frames. From there, the images are calibrated. Then, it is time to align the frames using the RA and declination. Aligning them will allow the target to stay in one place and makes photometry work more consistent. Once AIJ finishes aligning the frames, they are ready for photometry. The target star and multiple comparison stars are selected. When one measures the brightness of these comparison stars, it will help compare their light curve to the target if there is a potential transit. Ideally, the comparison stars should display a flat line, while the target should display a dip in the light curve.

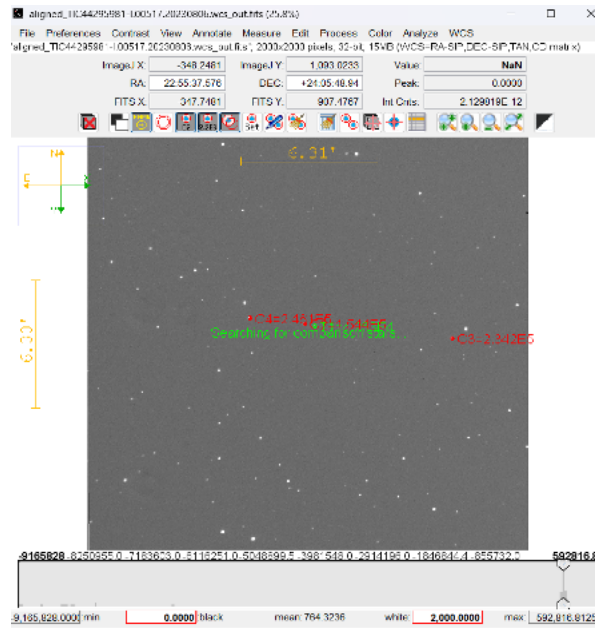


Figure 4. An example of doing photometry on a potential exoplanet candidate on AIJ.

TESS is the source to find potential exoplanet candidates in this project. It is a satellite that tracks any drop in light by snapshotting a potential dip in the light curve. TESS categorizes potential exoplanet candidates but also EBs, so one must be mindful of what they could be observing. On a specific observation day, TESS will provide multiple candidates with all sorts of information. Each exoplanet candidate has a string of numbers and the TESS Input Catalog (TIC). The TIC string will give the elevation, the magnitude of the star, the predicted transit time and duration, RA and declination, the size of the transit depth, and the predicted ingress and egress. Using this information, one can make a list of candidates to observe for that night. It is optimal to pick stars with lower magnitudes and high transit depths, as well as high elevations so that the candidates are easier to model. This is because there is limited time at WMO and many projects to be completed, so picking brighter stars and candidates with a large size will be time efficient.

2.2 Results

During the program here, the opportunity to conduct photometry on past WMO data arose. This was to aid the team in how to properly use the photometry software, AIJ. Eight data sets of different candidates were provided for which photometry could be completed and different transit curves could be generated. Below are the comparisons between the curves the team generated and the project advisor's light curves.

2.2.1 Past WMO Data

For the target KC26C0443 (Figures 5 and 6), one can see there is a transit in this target that looks consistent in the filters. However, this is not an exoplanet; this is a nearby eclipsing binary. This is because the target candidate light curve is flat. Should the target star's light curve be flat, it is in one's best interest to select different target stars, especially ones near the target star to see if

they transit. In this case, the one next to it had a transit. This can be ruled this out as an EB since it is likely the smaller star blocked out the light from the larger one.

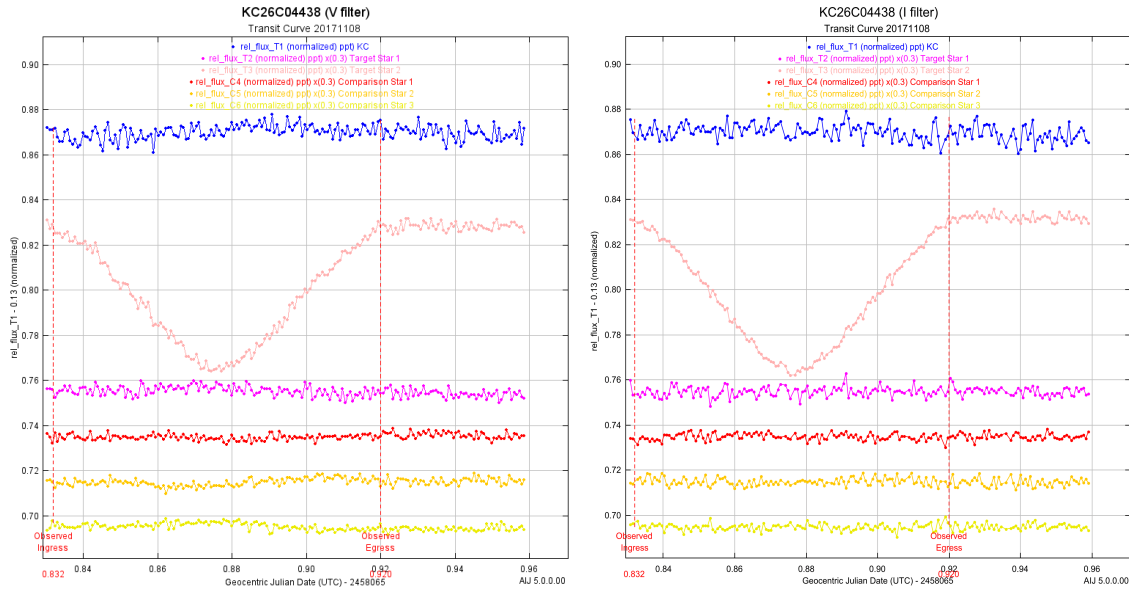


Figure 5. Transit light curve graphs of the target KC26C04438 in both V and I filters.

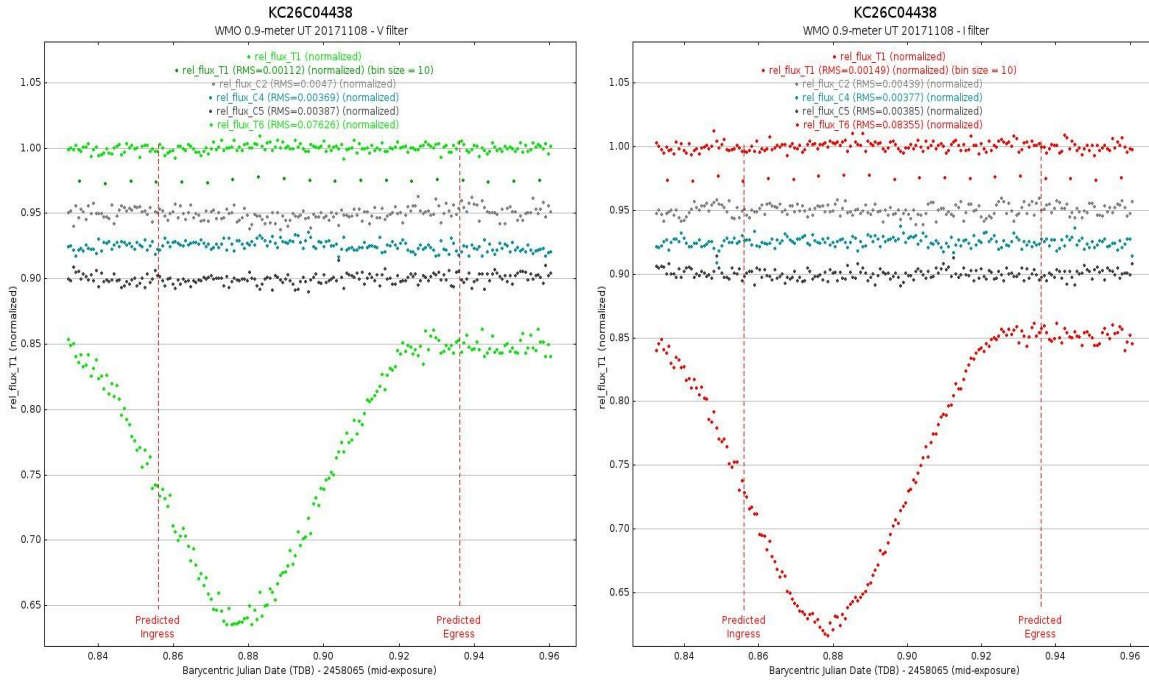


Figure 6. Advisor's graph of the target KC26C04438 in both V and I filters.

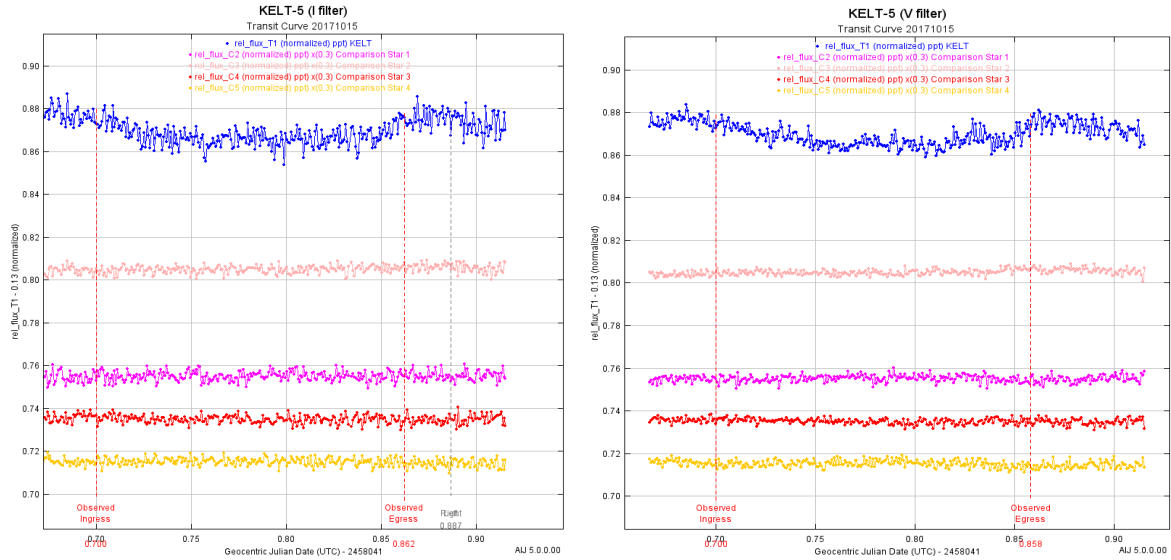


Figure 7. Transit light curve graphs of the target KELT-5 in both V and I filters.

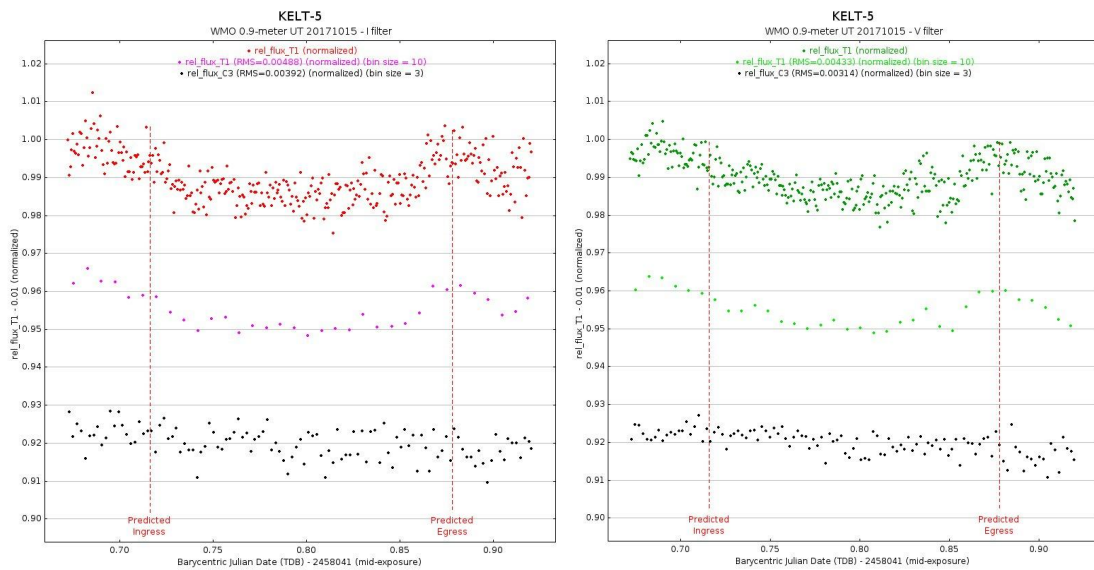


Figure 8. Advisor's graph of the target KELT-5 in both V and I filters.

There is also a clear transit in the KELT-5 candidate (Figures 7 and 8), and the transit dip is consistent and present between filters. This case is an exoplanet. Something that is interesting to note is that its star gave out pulsations that made it difficult to determine properties for this planet. It can also make further analysis to deem this as a potential planet rather inconsistent. Because of this, it can be hard to deem it as a planet at first.

2.2.2 Current WMO Data

A total of four targets were observed at WMO for this project, two of which had transits present. Below are the graphs of those targets (Figures 9 and 10).

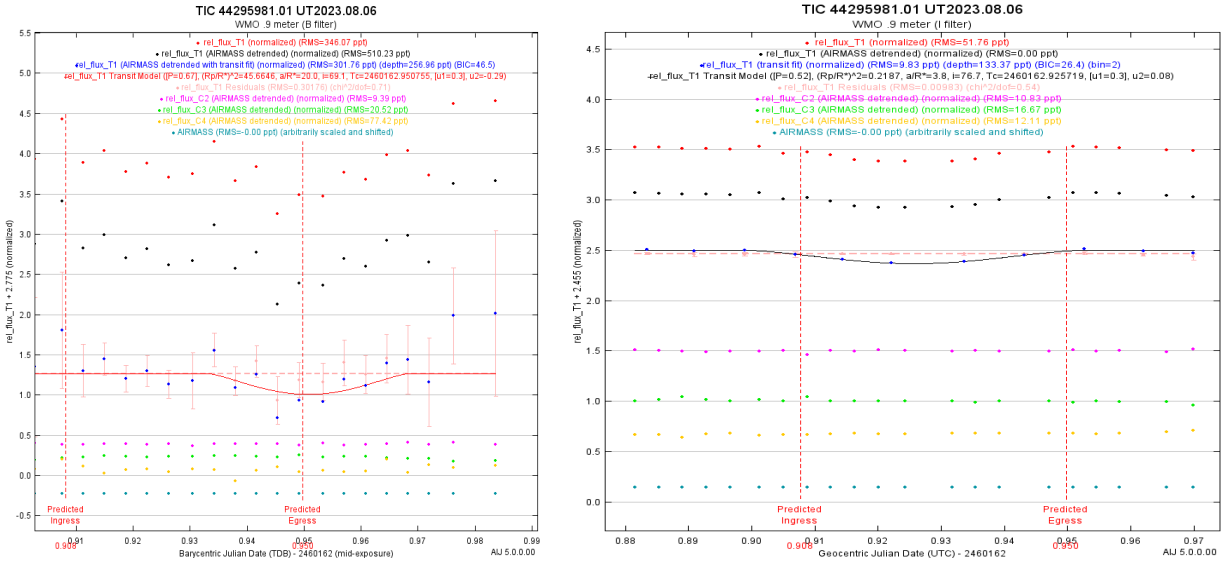


Figure 9. Transit light curve graphs of the target TIC 44295981.01 in both B and I filters.

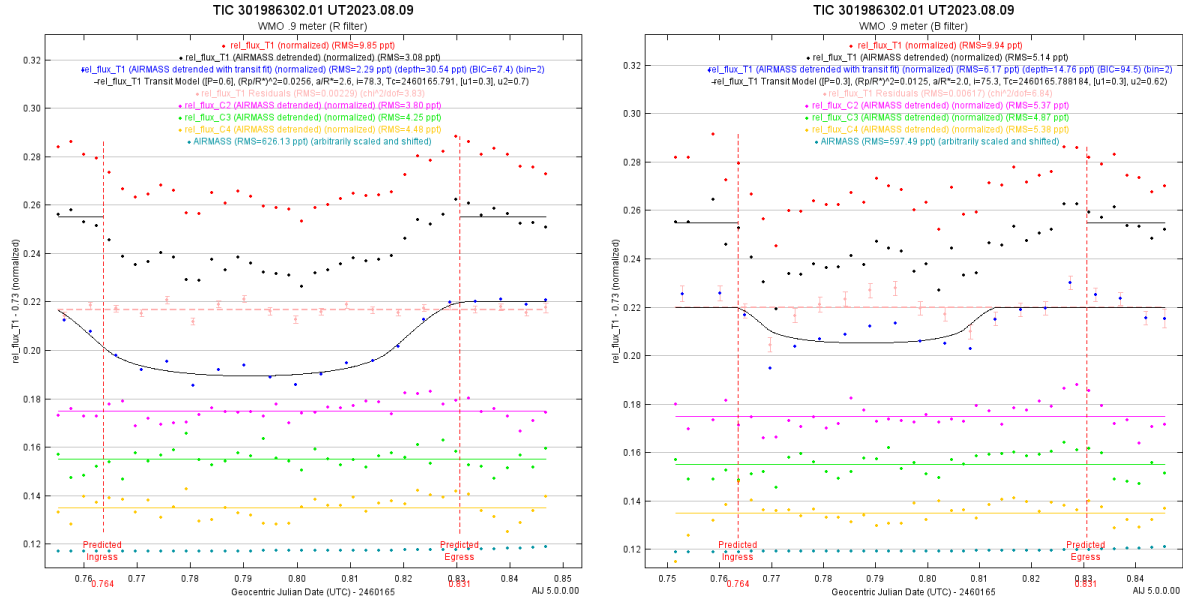


Figure 10. Transit light curve graphs of the target TIC 301986302.01 in both B and R filters.

In the infrared (I filter), there is a clear transit at the predicted ingress. However, in the blue (B filter), though there is transit, the star is not visible when doing photometry in the B filter. As discussed in section 2.1, counts in the light frame can determine if a light frame is

saturated or underexposed. In this case, this target's light graph was heavily underexposed, meaning not enough pixels in the image in the B filter compared to the I filter. Therefore, a chromaticity check cannot be completed as the star had blended in with the background in the B filter due to it being underexposed.

A transit is visible and consistent in both the blue and red filters. With this target, the team conducted data reduction, subtracting biases and darks and dividing flats, along with plate solving the data. This target passes the chromaticity check, as the transit depth in both filters is consistent. However, the transit is not smooth, with a noisy flat bottom. This can be because the star could be pulsating, such as in Fig. 8 with the KELT target, and the photometry is being interrupted because of that. More information is needed at this time. Another possible factor may be that data reduction was not properly handled, so perhaps a few frames may not have been of sufficient quality, and it may skew the readings of the rest of the frames.

3. Conclusions

Two out of four candidates have transits, yet one, TIC 301986302.01, seems the most viable as the light curve is consistent in both filters. When collecting data on potential exoplanet candidates, there are bound to be some discrepancies within the data. Usually, this can be remedied by removing anomalous data. In other cases, choosing different comparison stars may help as well to make the transit graph consistent. The transit of the comparison stars should always be flat as it will help even out the transit. If the target star is found to be flat instead, perhaps target stars near that aperture should be studied in search of other sources of transit. If a transit is found at another target star, it can be ruled as an EB.

There were some challenges the team encountered while securing observations. Due to cloudy skies, there weren't many nights the team was able to observe at WMO. If the sky is overcast, then it is not a good night for observing as visibility would be greatly hindered. If a strand of cloud covers the targets for only a small period of time, it will still show up in the photometry process through AIJ. This can mess up the photometry by making the image underexposed, meaning it doesn't have enough counts to display the data on the graphs, as shown by the targets below (Figure 11). Another challenge the team encountered involved numerous file naming issues. To make the reduction process goes smoother, it is in one's best interest to adopt standards and naming conventions that are consistent throughout the project to apply the data and analyzation process. There is a lot of information flowing through the different software so selecting a naming standard and conforming to it will allow the researcher to recall naming easier. When there are software issues, it becomes very hard to keep observing on track for that night. For instance, the CCD autopilot may not connect to the DFM control center, which means all calibration frames must be taken through the DFM, and this requires observing targets manually. This can cause target observing time to end earlier or later than usual, which is unfortunate as it robs transit data points.

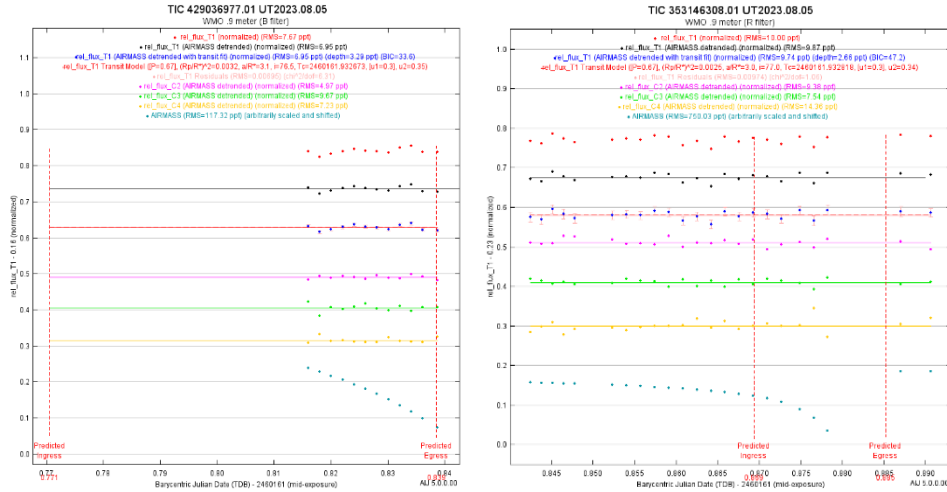


Figure 11. Graphs of the two transit light curves that did not have transits. The frames were too few and frame collecting had stopped due to terrible weather.

With two transit graphs having a transit, these candidates could potentially be an exoplanet. In the case of TIC 44295981.01, there wasn't a proper transit curve in the B filter, resulting in insufficient information to determine the validity of this candidate. It is easier to find an exoplanet if the transit depths are consistent throughout the filters. In the case of TIC 301986302.01, it is consistent across filters, however; it cannot be deemed as an exoplanet quite yet because of uncertainties. Perhaps with another fit model it would be easier to see an exoplanet fit. This can be done with a program called EXOFAST.

During this project, many skills were gained. Not only did the team frequently learn about how to set up, maintain, and shut down the telescopes each night, there were a variety of different software to use: the main telescope software and the photometry software of AIJ. Even if there isn't a clear answer on whether these candidates are exoplanets, in the continuation of this project there will be more opportunities to acquire more targets and learn if the chosen candidates pass for exoplanets.

Acknowledgements

I acknowledge Brigham Young University's Department of Physics and Astronomy for supporting West Mountain Observatory and making it available for this research. This research was also funded by the NSF grant #2051129. I would like to thank Fei Villar for additional help in generating transit light curves, Dr. Stephans for the transit light curve template, and finally the research team who spent an abundance of time with me up at WMO.

References

Deljookorani, S. et al. (2020, May 15). Exoplanet Photometry and false positives. Journal of Research in Progress Vol 3.

<https://pressbooks.howardcc.edu/jrip3/chapter/exoplanet-photometry-and-false-positives/#:~:text=Exoplanet%20transit%20photometry%2C%20also%20known,system%20is%20called%20an%20exoplanet>

Faulkes Telescope. (n.d.). Photometry of supernovae with Makalii. Photometry in Astronomy. http://resources.faulkes-telescope.com/file.php/144/Supernovae_with_Makali.pdf

Lee, R. (2018, October 21). A guide to astroimagej differential photometry - britastro.org. A Guide to AstroImageJ Differential Photometry. https://britastro.org/wp-content/uploads/sites/Tutorial_AIJ_Photometry_v2.06.pdf

NASA. (n.d.). 5 Ways to Find a Planet | Explore – Exoplanet Exploration: Planets Beyond our Solar System. Exoplanet Exploration: Planets Beyond Our Solar System. <https://exoplanets.nasa.gov/alien-worlds/ways-to-find-a-planet/#/2>

Swanson, T. (2016, November 30). Time-Series Methods in Experimental Research. Association for Psychological Science - APS. <https://www.psychologicalscience.org/observer/time-series-methods-in-experimental-research>

Thomas, M. (2020). Lights, Darks, Bias and Flats - What are they? — Astro Journey UK. Astro Journey UK. <https://astrojourneyuk.com/lights-darks-bias-and-flats-what-are-they-how-do-you-take-them-and-what-do-you-do-with-thems>

Cooperative Observing at a Modest-Sized Observatory

Michael D. Joner¹, Denzil E. Watts IV¹, Seneca H. Bahr¹, Oliver Hancock¹, Michael W. Holland¹, Hafsa Jamil^{1,2}, Eden Saxton^{1,3}, and Malaya Williams-Jones^{1,4}

¹Brigham Young University, Department of Physics and Astronomy, Provo, UT 84602

²Rutgers, the State University of New Jersey, Department of Physics and Astronomy, Piscataway, NJ 08854

³Weber State University, Department of Physics, Ogden, UT 84408

⁴Columbia University, Department of Physics, New York, NY 10027

Subject Keywords

Observatory Operations; Undergraduate Education; Photometry, CCD

Abstract

The West Mountain Observatory is an astronomical research facility operated by Brigham Young University, located on an isolated mountain approximately 22 kilometers southwest of the main Provo UT campus. The observatory was upgraded 15 years ago and has since been utilized primarily as an undergraduate research facility. The observatory is well suited to do work on projects utilizing time series photometric observations and has been particularly successful at conducting multiple projects for undergraduate student researchers that require observations of different durations and cadences using various filter combinations. This requires additional planning and cooperation between the different programs that are often running during the same periods of time. Our student observers are often asked to coordinate their observations with observations for other student projects so that everyone can get the data they need regardless of temporary disruptions from weather, schedules, instrumentation problems, or other unforeseen events. This use of cooperative observing has worked well in past years and has resulted in our undergraduate student researchers gaining a wide variety of experiences securing observations for projects as different as making rotation curves of solar system objects, observing various classes of variable stars, detecting exoplanet transits, and working on reverberation mapping and variability analysis of AGNs. This paper will present results from our recent 2023 summer observing season that included four BYU undergraduate students and three students participating in a 10-week Research Experience for Undergraduates. Each of these students spent multiple two-night observing runs at the observatory doing cooperative observing for multiple projects.

1. Introduction

The Brigham Young University West Mountain Observatory (WMO) is a research facility that is operated primarily by undergraduate students during the busy spring and summer observing season. The primary goal of these operations is providing an immersive experience for the

student observers that gives them a good chance of completing their own individual research projects.

Using a technique called cooperative observing, undergraduate students at WMO successfully work on different time-series imaging projects being conducted by themselves, other students, and faculty. Working on multiple projects being done at different cadences has proven to be especially useful in helping increase the chances of having many different investigators obtain sufficient data to successfully complete their respective projects despite the usual problems that disrupt observational data flow.

Our student observers generally work in small teams for a couple of nights at a time and secure observations needed for different student projects while also working on observations for their own research. The most likely result of this practice is that each student ends up with the observations they need independent of interruptions caused from poor weather, preset observing schedules, instrumentation problems, or other random occurrences. This model of cooperative observing has allowed our undergraduate student researchers to gain a wide variety of experience working on different projects with targets ranging from objects within the solar system to distant active galaxies.

This paper will describe cooperative observing efforts at WMO during 2023. We also present several examples of student research work as well as results from additional long-term monitoring projects done during the 2023 spring and summer observing season.

2. Facilities at West Mountain

The Brigham Young University (BYU) West Mountain Observatory (WMO) shown in Figure 1 is a modern astronomical research facility located approximately one hour from the main BYU campus in Provo, Utah. West Mountain is a lone mountain in the center of Utah Valley on the southeast shore of Utah Lake. The observatory is located slightly west of Long Ridge, about a quarter mile from the numerous communications towers seen near the center of the 6850-foot West Mountain. The site itself is far enough to the west of the developed areas along the Wasatch Mountains so that it continues to produce high-quality research observations. Overhead and to the west, the sky brightness at the West Mountain site is approximately Bortle 4, with median seeing conditions of about 1.6". Seeing is worse when it is windy, but there are also occasional nights with sub-arcsecond seeing conditions.



Figure 1. The BYU West Mountain Observatory looking west toward Utah Lake. Beyond that are the open spaces of western Utah and Nevada. Photo courtesy of Patrick Wiggins.

WMO was built in 1981 when it became apparent that there were no longer opportunities to make dark sky research observations from the Provo campus. The original instrument at WMO was an aging 0.6-m Tinsley reflector. This telescope was purchased in the 1950s and placed atop the BYU Eyring Science Center, where it produced high-quality photometric observations for many publications until local light pollution and encroaching development on campus necessitated a move to the remote site at West Mountain. Realizing that the 0.6-m telescope would soon reach the end of its useful life, BYU designed and built the observatory dome and building at West Mountain to house a 1-meter class telescope without requiring significant modifications to the facility itself. A home was built next to the observatory in 1982 where the resident astronomer lived until 1988. Through the mid 1990s, research and teaching were vigorously pursued at West Mountain.

For the next ten years there were numerous attempts made to upgrade the older telescope. While these were generally successful, it was also apparent that the 0.6-m telescope would not be suitable for making long, guided exposures without making a large investment to replace the telescope mount. It was clear that this upgrade would be comparable in cost and scope to obtaining a larger replacement telescope.

In 2006 the BYU astronomy group was awarded a National Science Foundation PREST (AST 0618209) grant to upgrade the main telescope at WMO. In the middle of 2009, construction of the new DFM Engineering 0.91-m f/5.5 Ritchey-Chrétien reflecting telescope (Figure 2) for WMO was completed. The telescope was installed in the main dome in late August of 2009 and regular research observations commenced the next week.



Figure 2. The 0.91-meter $f/5.5$ Ritchey-Chrétien reflecting telescope at WMO.

The dome visible on the south end of the main building is 7 meters in diameter with a slit that is 1.3m wide. The large dome on the main building is the location of the DFM 0.91-meter $f/5.5$ Ritchey-Chrétien reflecting telescope. The smaller round building and dome house a 0.51-meter RCOS reflector (Figure 3) mounted on a Mathis Systems fork mount. The small rectangular building and dome contain a 0.32-meter RCOS optical tube (Figure 4) mounted on a Planewave L-350 mount. The house to the north is the resident observer's former quarters. The observatory itself contains a computer room, a local area network, a large control room, several work areas, a small library, kitchenette, rest rooms, living space, and two dorm rooms, each of which has two beds. The observatory and house together can accommodate up to eight people (a bit crowded) for an extended observing run.

The largest nearby town is Payson, UT with a population of about 22,000. The communities of Genola to the south and Benjamin to the east are agricultural areas with low populations. Utah Lake borders to the west and north. There is very little population west of the lake for hundreds of miles and the skies are especially dark in that direction. Although the population along the Wasatch front is growing, most of this growth is to the north. Zoning to the south and east of the observatory and the lake on the north and west ensure that the site will remain adequately dark for the foreseeable future.



Figure 3. The 0.51-meter $f/8$ Ritchey-Chrétien reflecting telescope at WMO.



Figure 4. The 0.32-meter $f/9$ Ritchey-Chrétien reflecting telescope at WMO.

In order to show site quality, Figure 5 shows a typical example of deep sky imaging that has been done at the observatory in recent years to create selected EPO images from WMO.



Figure 5. The Western Veil Nebula, NGC 6960, imaged with the 0.91-m telescope at WMO in BVR, H-alpha, and OIII filters. Image assembly courtesy of Robert Gendler.

3. Cooperative Observing

BYU has long emphasized providing mentored research opportunities for undergraduate students. In support of this program, WMO has been operated by groups of undergraduate students during the Spring and Summer terms each year, when students can conveniently stay at the observatory for two or three night observing runs without conflicting with class work.

It has been a challenge to find ways to schedule and operate the observatory in a manner that provides opportunities for the students to work on individual projects while still leaving open time for observations to be obtained for multi-year monitoring projects or the occasional target of opportunity. The process is further complicated by the occurrence of random events such as an unusual run of bad weather, excessive fire smoke, equipment problems, or some event like the recent COVID-19 pandemic that can impact regular operations at the observatory. If observations are tied to a fixed schedule, an all too common outcome is that one or more students do not work sufficient time at the observatory to fully learn the operating systems or secure enough observations to complete their projects. This is especially true for the one or two summer REU students who work at the observatory for just 10 weeks during the summer months.

With a moderate amount of schedule coordination, it is possible to work on 10 or 12 (and sometimes more) different projects requiring observations in different filters at different

cadences at a small observatory with two or three well-equipped research telescopes like those at WMO. This allows student observers to work on individual projects and also contribute to some long-term monitoring work. Students gain observing experience using different telescopes to work on projects requiring different strategies.

Cooperative observing programs work well in a setting such as a small college or university observatory by helping to ensure students get the data they need for their projects while not being locked into a limited number of scheduled nights that can be lost to different random events. During times that are not suitable for observations, students can work on data reduction and analysis. Cooperative observing has proven to be successful for operating a small observatory like WMO. The inherent flexibility of cooperative observing has added to student training and experience levels at WMO and has decreased the ‘feast or famine’ pattern that is more typical in a fixed schedule or allocated observing time approach.

4. Student Projects

There were four primary student research projects worked on at the observatory during 2023. These projects each involved time series photometry and required observational cadences that ranged from 30 seconds or less for several hours on a few nights up to needing a group of points two or three times a week for a period of several months. The projects for the student observers were given high priority when making plans for individual nights that were suitable for observations.

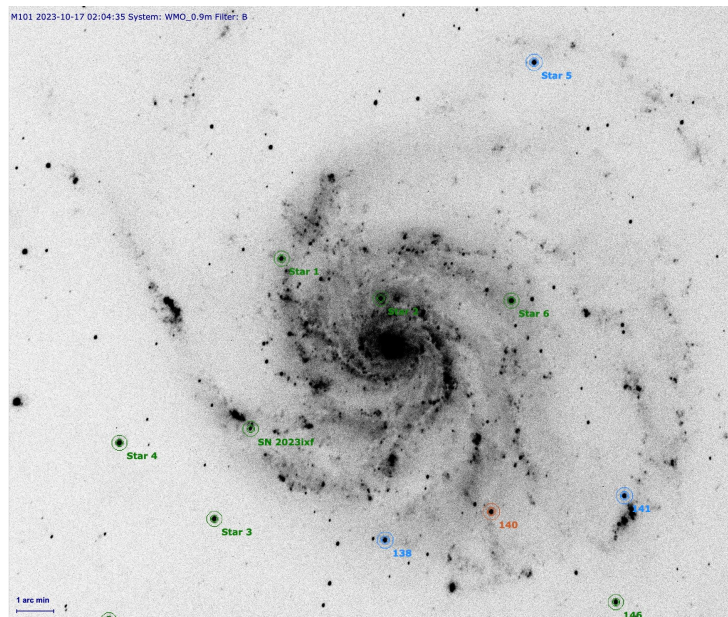


Figure 6. A 300-second exposure using the B filter and the 0.9-m telescope at WMO. The field is approximately 20' square and centered on M 101. The comparison stars used are marked, along with the position of SN 2023ixf.

In addition to working on strategies for automated data reduction routines at the observatory, Malaya Williams-Jones and Michael Holland secured regular observations using the 0.9-m telescope with BVR_cI_c filters for SN 2023ixf in the M 101 galaxy. The results of these observations are shown in Figures 6 and 7.

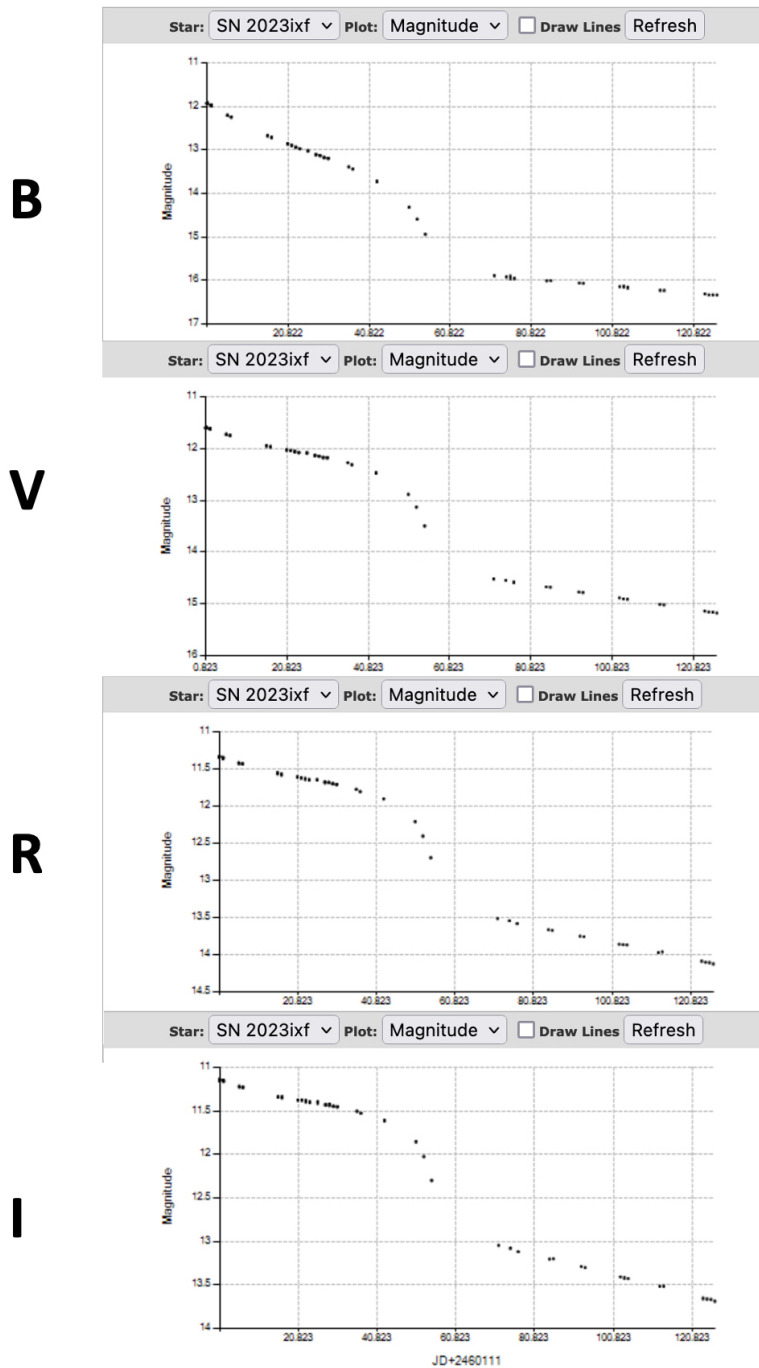


Figure 7. Light curves for SN 2023ixf in the $BV(RI)c$ filters.

Students Hafsa Jamil and Oliver Hancock worked on learning the techniques needed to photometrically observe and confirm TESS candidates selected as possible transiting exoplanets. These new skills were practiced by first observing and making light curves for some high amplitude δ Scuti (HADS) variables. Next, the students made light curves for some archival suspected exoplanet transits observed at WMO for the KELT survey follow-up project. These new skills were then tested by selecting actual TESS candidates, securing new observations, and examining the results to search for nearby eclipsing binaries, do chromaticity checks, and verify transits. Results from these learning experiences are shown in Figures 8 and 9 below.

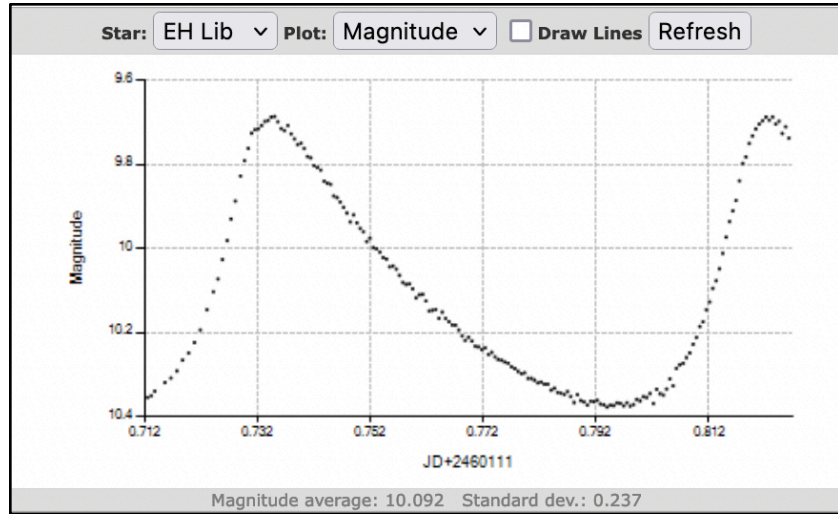


Figure 8. Light curve for the HADS EH Lib in the B filter secured with the 0.32-m telescope at WMO.

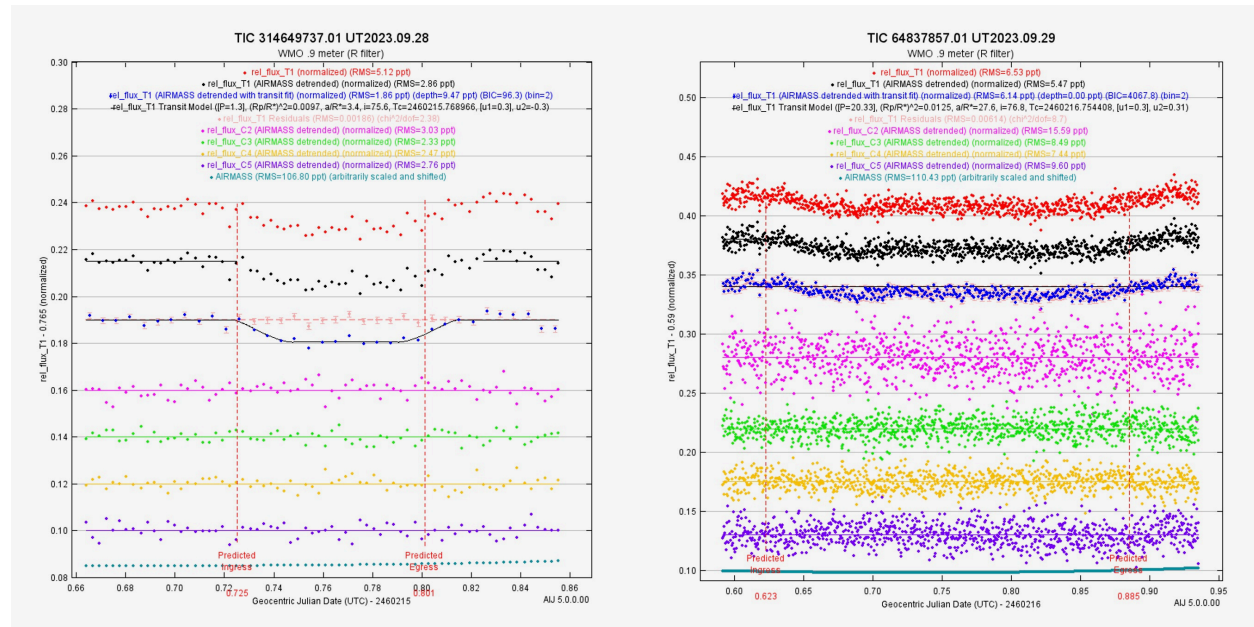


Figure 9. Light curves for suspected transiting exoplanets from the 0.9-m telescope at WMO.

Eden Saxton secured regular BVR_{clc} observations of NGC 5466 to supplement archival data and study the properties of the anomalous Cepheid BL Boo and three additional RR Lyr variables. A sample of her results are shown in Figure 10 below.

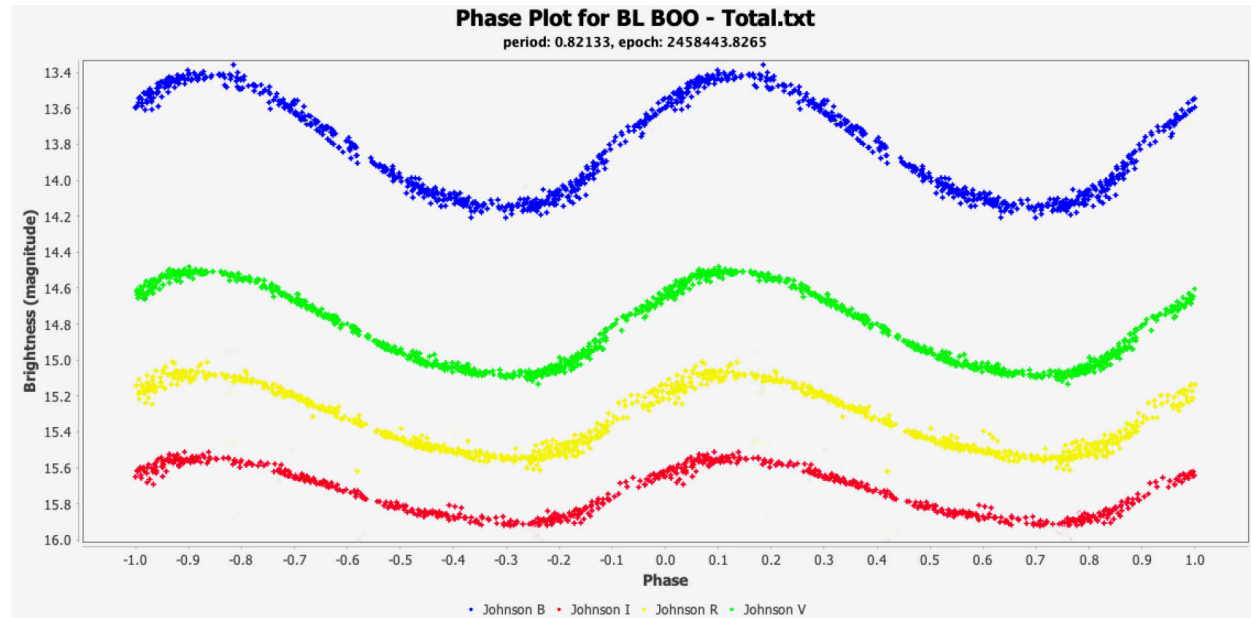


Figure 10. Preliminary differential light curves of BL Boo in the globular cluster NGC 5466 from data secured between 2015 and 2023 using BVR_{clc} filters on the 0.9-m telescope at WMO.

Denzil Watts worked on comparing measurements made using different temperature indices ($B-V$, $b-y$, α , and β) during the pulsation cycles of the variable star V2455 Cyg. During this investigation, he also secured high quality light curves of many other high amplitude δ Scuti and SX Phoenicis stars. Some examples of this work are shown (Figures 11 – 14) below.

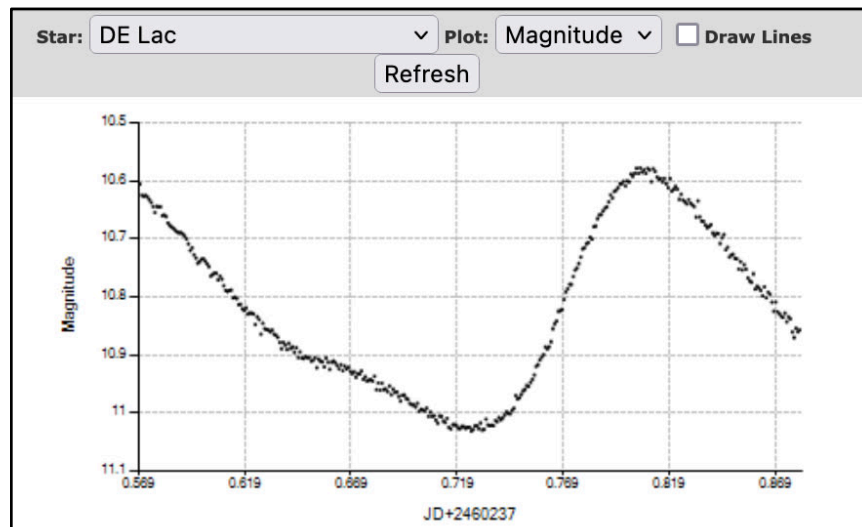


Figure 11. Light curve for the high amplitude δ Scuti star DE Lac in the B filter secured with the 0.32-m telescope at WMO.

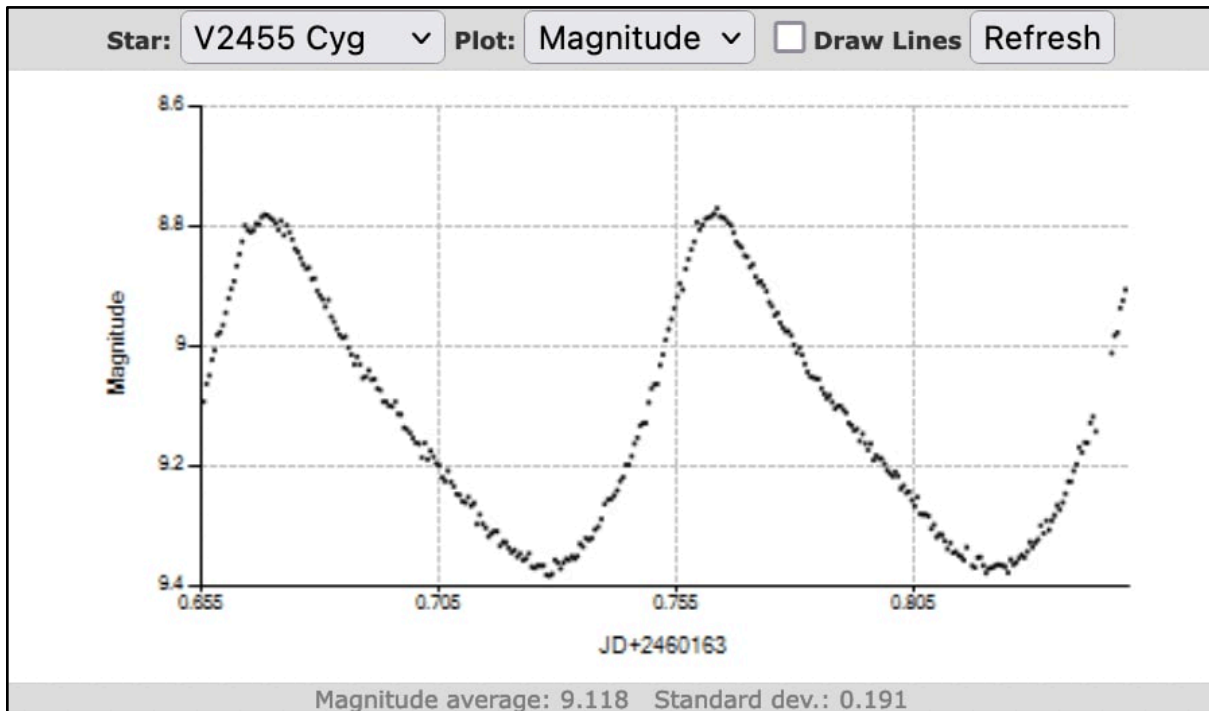


Figure 12. Light curve for the high amplitude δ Scuti star V2455 Cyg in the B filter secured with the 0.32-m telescope at WMO.

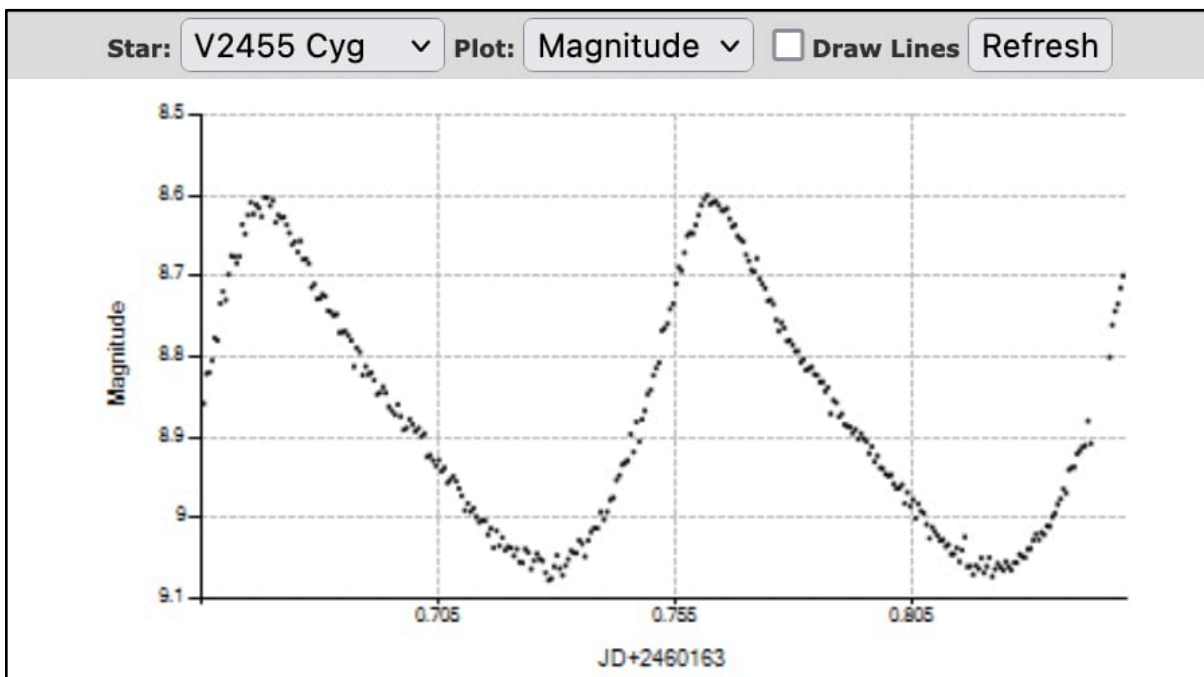


Figure 13. Light curve for the high amplitude δ Scuti star V2455 Cyg in the V filter secured with the 0.32-m telescope at WMO.

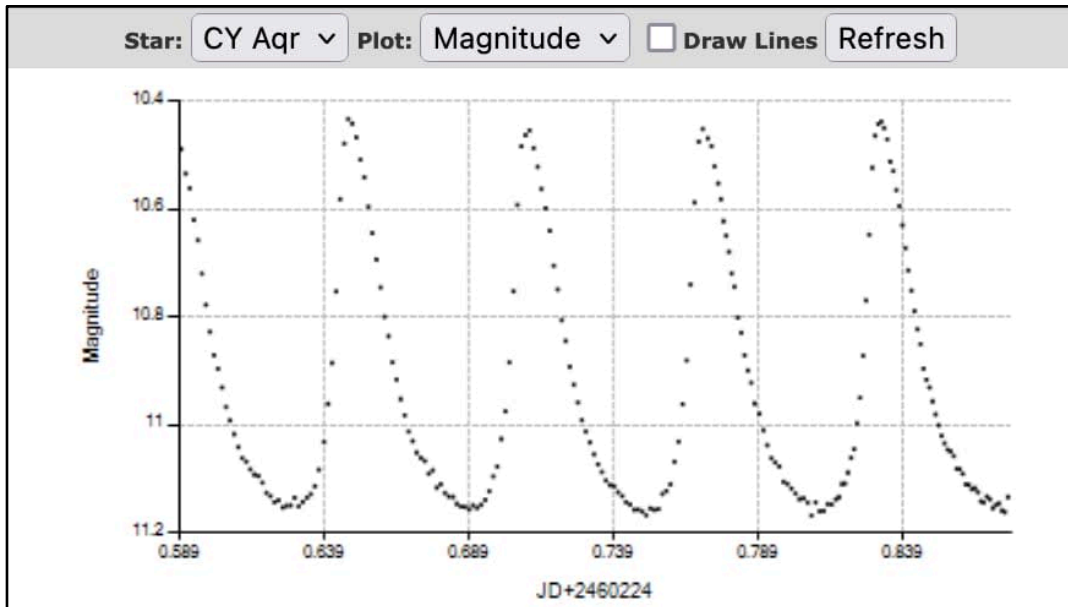


Figure 14. Light curve for the SX Phoenicis star CY Aqr in the V filter secured with the 0.32-m telescope at WMO.

Results from these various student projects frequently appear in presentations made by students at professional meetings. Student presentations made during the past five years are listed in Figure 15. Student coauthors decreased during this time due to the low number of students available to work at the observatory during the COVID-19 pandemic. There were 19 student coauthors on nine different presentations made at the 243rd meeting of the American Astronomical Society in January 2024 that resulted from the 2023 summer research program.

Recent Student Coauthored Meeting Presentations

“Variable Star Detection in Open Clusters Using Deep Learning and Transformers,” 2023, AAS, **241**, 105.14 - Two undergraduate coauthors

“Photometric Analysis and Temperature Estimates of the High-Amplitude delta Scuti Star V2455 Cygni,” 2023, AAS, **241**, 303.08 – Two undergraduate coauthors

“Optical brightening of BL Lacertae,” 2022, ATEL, 15684 – Two undergraduate coauthors

“Standardized H-alpha Observations of Open Star Clusters h and chi Persei and NGC 752,” 2021, AAS, **237**, 150.11 – One undergraduate coauthor

“The 2021 Outburst of BL Lacertae,” APS Four Corners Section, Virtual Meeting, October 2021 – One undergraduate coauthor

“Confirmation of Short Period Pulsating Variables Discovered by the ATLAS Survey – The Faint End,” 2020, AAS, **235**, 106.04 – Nine undergraduate coauthors

“Confirming Faint Objects Data from ATLAS as Variable Stars,” APS Four Corners Section, Prescott, AZ, October 2019 – Two undergraduate coauthors

Figure 15. Number of BYU student coauthors using WMO data in presentations made between 2019 and 2023.

5. Other Monitoring Projects

Several of the long-term monitoring projects over the past several years have involved securing regular observations of different active galaxies. Typical AGN targets include blazars, such as Mrk 501, AO 0235+164, and BL Lac, or Seyfert galaxies like Mrk 817, Zw 229-015, and NGC 5548. Cadences for these observations are generally one sequence of observations every observable night, but during times of high activity observations are often done in a longer time series over a period of several hours.

Observations that are secured at WMO have contributed to numerous articles in refereed journals that involve major group collaborations such as LAMP, AGNSTORM, and WEBT. Student observers that make significant contributions to these projects are often invited to be coauthors on these impactful publications.

Examples of a seasonal light curve and a night of longer time series runs are shown below (Figures 16 – 18) for the blazar BL Lac followed at WMO in 2023.

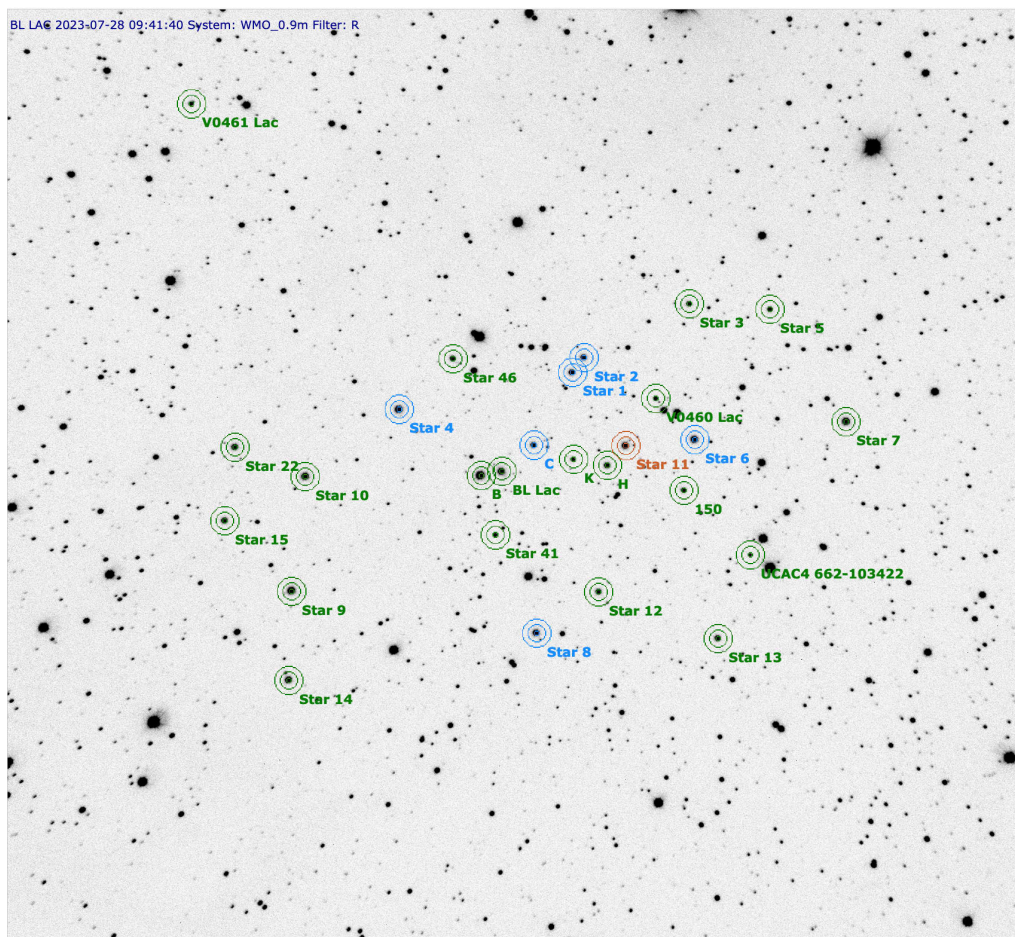


Figure 16. R_c image of BL Lac secured with the 0.9-m telescope at WMO. The field shown here is approximately 20' wide. North is up, with east to the left.

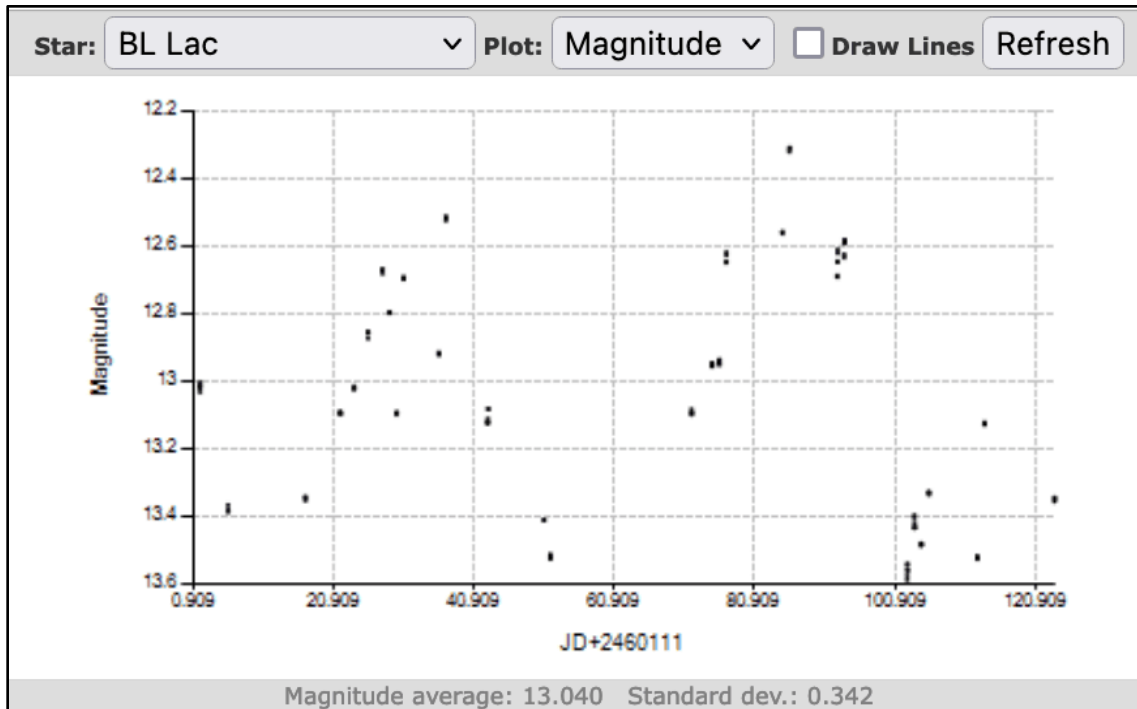


Figure 17. A seasonal light curve for BL Lac secured with the 0.9-m telescope using an R_c filter during summer 2023.

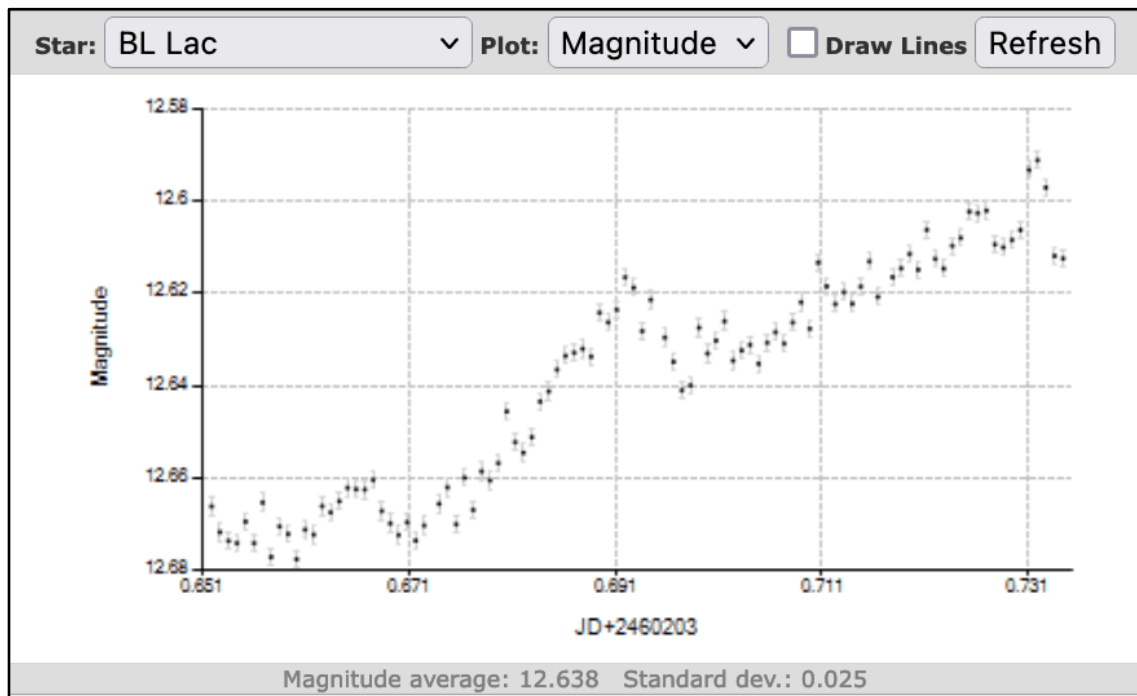


Figure 18. Light curve for BL Lac secured with the 0.9-m telescope using an R_c filter on UT 20230916. This curve shows a 0.09 magnitude increase in a little less than two hours of time.

Interesting faint variable stars that can be observed photometrically at a variety of cadences are ideal targets for the telescopes at WMO. Figures 18 and 19 show examples of two faint SX

Phoenicis stars that can be observed at relatively short cadences with the main 0.91-m telescope. The pulsation periods of 56 minutes for BL Cam and 87 minutes for the even fainter BQ Psc necessitate rapid cadence observing sequences. Fainter targets than BQ Psc can be observed with longer exposures if high time resolution is not required.

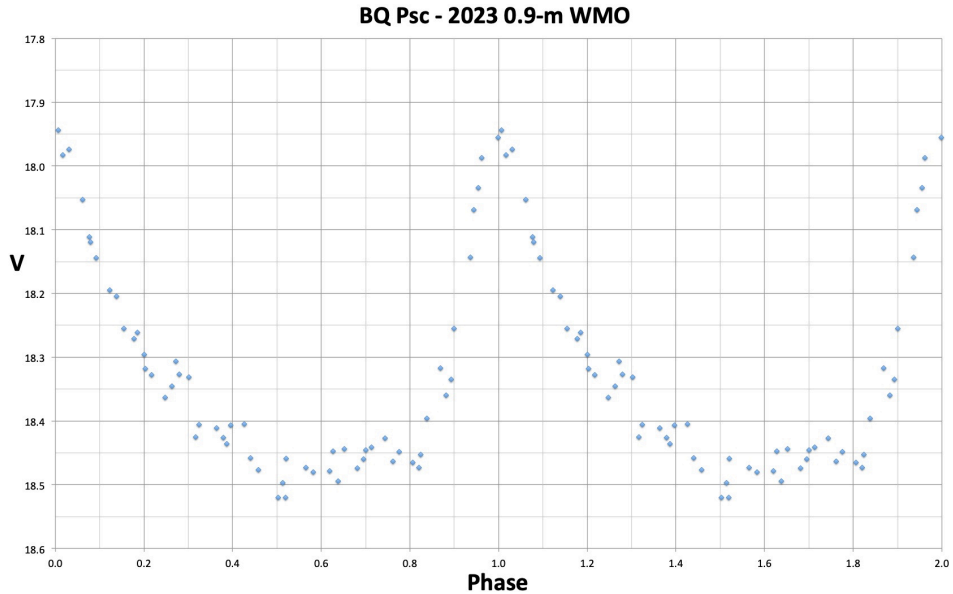


Figure 19. Faint SX Phoenicis star in the V filter from observations secured with the 0.9-meter telescope at WMO.

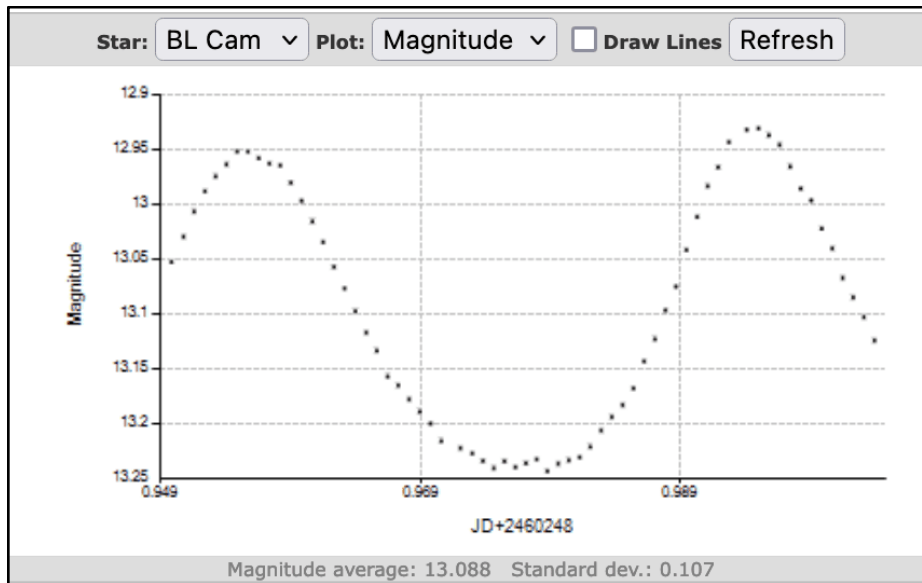


Figure 20. A V filter light curve for the SX Phoenicis star BL Cam secured with the WMO 0.91-m telescope.

The student observations secured for target of opportunity observations and long-term monitoring projects often appear a year or more later as part of a significant publication in a refereed journal. Students who have made a significant number of observations for a project of

this type are often invited to appear as coauthors on the publications. There are usually authorship rules established for these different major collaborations, but in many cases the student researchers qualify to appear as coauthors. Publications that utilize large numbers of WMO observations that have invited student coauthors during the past three years are listed in Figure 21. It is noteworthy that all these publications appear in high-impact journals. It is anticipated that this level of student publication will continue and many of the students who participated in the 2023 observing season will appear on upcoming publications.

Recent Student Coauthored Refereed Publications

“Extreme photometric and polarimetric variability of blazar S4 0954+65 at its maximum optical and γ -ray brightness levels”, 2023, MNRAS, **526**, 4502 – Three undergraduate coauthors.

“The Optical Behaviour of BL Lacertae at its Maximum Brightness Levels: A Blend of Geometry and Energetics”, 2023, MNRAS, **522**, 102 – Four undergraduate coauthors

“Multi-messenger characterization of Mrk 501 during historically low X-ray and γ -ray activity,” 2023, ApJS, **266**, 37 – Five undergraduate coauthors

“Searching for Dwarf H α Emission-line Galaxies within Voids. I. Survey Methods and First Observations,” 2023, ApJ, **950**, 189 – Three student coauthors.

“Rapid Quasi-Periodic Oscillations in the Relativistic Jet of the Blazar BL Lacertae,” 2022, Nature, **609**, 265 – Two undergraduate coauthors

“Space Telescope and Optical Reverberation Mapping Project. IX. Velocity-Delay Maps for Broad Emission Lines in NGC 5548,” 2021, ApJ, **907**, 76 – One undergraduate coauthor

“Discovery of a Young Low-mass Brown Dwarf Transiting a Fast-rotating F-type Star by the Galactic Plane exoplanet (GPX) Survey,” 2021, MNRAS, **505**, 4956 – One undergraduate coauthor

Figure 21. Publications utilizing data from WMO that have included BYU student coauthors in the past three years. Each of these publications appeared in high-impact journals.

6. Summary

This paper has presented a model of cooperative observing that has been used successfully at WMO as it has been adjusted for varying circumstances over the past several years. A primary benefit from this scheduling method has been a more even distribution of usable data among the various student research projects. An additional bonus is being able to continue an observing program with several long-term monitoring projects and the option to make target of opportunity observations, should that become a priority. Results from several student research projects and additional monitoring observations done during the recent 2023 summer observing season were given in this paper. These results illustrate the variety of different time series observations that can be scheduled using this method. Cooperative observing allows students to spend roughly equal periods of time at the observatory regardless of the time required for their project. This is a significant benefit in regard to student training on the various observatory systems. For example, the 2023 student observers included four BYU undergraduate students and three undergraduate students participating in a summer Research Experience for Undergraduates program. These students each started off with very different levels of observing experience and knowledge of the work done at a research observatory. Observing skills steadily

improved as the students spent multiple two-night observing runs at WMO doing cooperative observing for multiple projects. By the end of the summer, even the least experienced students were able to operate the different available telescopes, make a variety of photometric observations, and solve many of minor problems that occur during a typical observing run. Even more significant was the fact that all students had enough training, data, and experience from their time at the observatory to satisfactorily complete their projects.

Acknowledgments

Many of the light curves given in this paper are screenshots of graphs generated for various targets using the VPHOT program available through the AAVSO membership of several of the authors. Unless otherwise noted, all photos displayed here were secured by the different authors of this presentation.

We thank the Brigham Young University College of Physical and Mathematical Sciences and Department of Physics and Astronomy for continuing support of undergraduate mentoring and the research done at the West Mountain Observatory. Funding for the summer REU students was provided by NSF Grant #2051129. Additional students were supported by college mentoring funds.

Blame it on Aquila: Fictional and Factual Novae

Kristine Larsen

Central Connecticut State University, 1615 Stanley St., New Britain, CT, 06050, USA;
larsen@ccsu.edu

Subject Keywords

History of astronomy; interdisciplinary astronomy; novae, historical; stars: individual (CI Aql, DO Aql, GK Per, S For, V382 Vel, V603 Aql, V1494 Aql, V1548 Aql, V2572 Sgr, V3645 Sgr)

Abstract

Astronomical objects have featured in works of science fiction for centuries, including variable stars. In particular, novae and supernovae have played central roles in the plots of numerous works of science fiction. While the names and locations in the sky of most of these fictional variables are vague, occasionally a specific constellation will be named, or a historical nova or supernova is specifically invoked in fiction, to give real-world gravitas to the imaginary scenario. This work reviews the use of novae and supernovae as plot devices in works of science fiction, demonstrating a curious association of such objects with the constellation Aquila despite the fact that there are several constellations that have hosted more known novae. A study of popular-level astronomical news coverage of observed novae in Aquila in the 20th century reveals possible explanations for the frequency of spectacular Novae Aquilae in science fiction.

1. Introduction

Astronomical objects of many types have provided fruitful fodder for works of science fiction for centuries. Variable stars are no exception. From the fictional eclipsing binary Walaz in the Edmond Hamilton 1934 short story “Thundering Worlds” to the use of pulsating variables as signposts on an interstellar highway in George O. Smith’s 1953 pulp novel *Troubled Star*, variable stars of various flavors have starred in popular media. Not surprisingly, cataclysmic variables, in particular novae and supernovae, have been a favorite plot hammer in the novelist’s (and screen writer’s) toolkit. Exploding stars have featured in science fiction for well over a century, long before the existence of both novae and supernovae as separate classes of objects was known (Baade & Zwicky 1934, 254). Indeed, even in the 21st century the term “nova” is often used ubiquitously in popular media as a catch-all term for stellar outbursts, even when a supernova – or a super-flare – is clearly meant.

2. Connection to Real-world Novae

2.1 Identifying Possible Real-world Precedents

While the names and locations in the sky of most fictional variables remain vague in fiction, occasionally a specific constellation will be named, as in the case of the film *2:22* (2017), in which

a nova is specifically said to occur in Aries (the ceiling of New York’s Grand Central Station playing a significant role in the film), or *Nova* (2013), in which a supernova is seen in Orion. There are also other examples where a real-world precedent can be tentatively identified. In Larry Niven’s novella “The Fourth Profession” (1971), an interstellar species mysteriously arrives on Earth, their approach observed while still in the outer solar system because astronomers had been looking in the direction of Sagittarius, observing a nova. This is perhaps a nod to Nova Sagittarii 1970 (V3645 Sgr), which reached magnitude 8, or Nova Sagittarii 1969 (V2572 Sgr), which reached 6.5 (Arhipova & Dokuchaeva 1970; Bateson 1969). Niven’s extraterrestrial mercenaries threaten humanity with the explosion of the sun if we do not build them a moon-based laser system to launch their ship toward the next star on their trade route, the aforementioned nova insinuated as the unfortunate fate of an extraterrestrial civilization that had refused a similar request.

On rare occasions, a historical nova or supernova is specifically invoked in fiction, to give real-world gravitas to the imaginary scenario. For example, GK Persei (Nova Persei 1901) features prominently in H.P. Lovecraft’s 1919 short story “Beyond the Wall of Sleep,” with the author (who owned three telescopes and had been interested in astronomy since the age of 12 [Williams 2011, 36]) quoting by name from Garrett P. Serviss’ description of the nova in his *Astronomy with the Naked Eye* (1909, 152). James Blish’s 1971 novel *And All the Stars a Stage* follows the interstellar journey of survivors from a blue variable star’s planetary system as they search for a new planet to call home. At the end of the novel, the humanoids settle on Earth, and the destruction of their home star is witnessed by their descendants as SN 1054 (191). In the novel *Sunstorm* (2005) by Arthur C. Clarke and Stephen Baxter the sun suffers a planet-threatening super-flare event, described as similar to the behavior of the star S Fornacis (86). The only reported outburst of S For was reported by Abetti and two other observers on March 6, 1899; as noted by Annie Jump Cannon (1907, 35) and later Cecilia Payne-Gaposchkin (1952, 223), the Harvard plates do not show any evidence of this event. VSX lists the star as constant (VSX 2022). Apparently, this inconvenient truth about the star escaped the authors during their research.

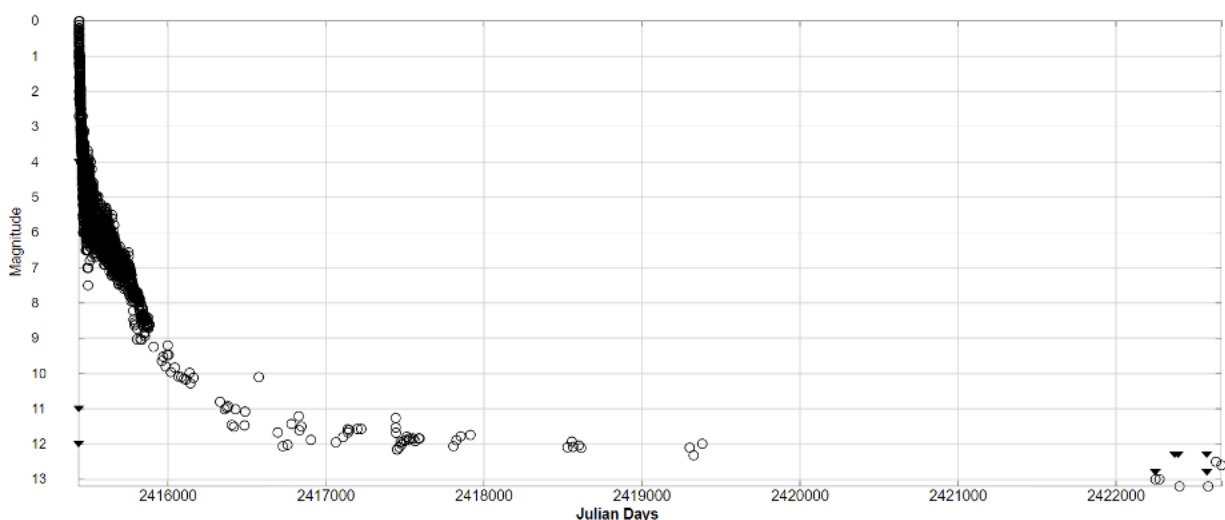


Figure 1. AAVSO visual light curve of GK Persei.

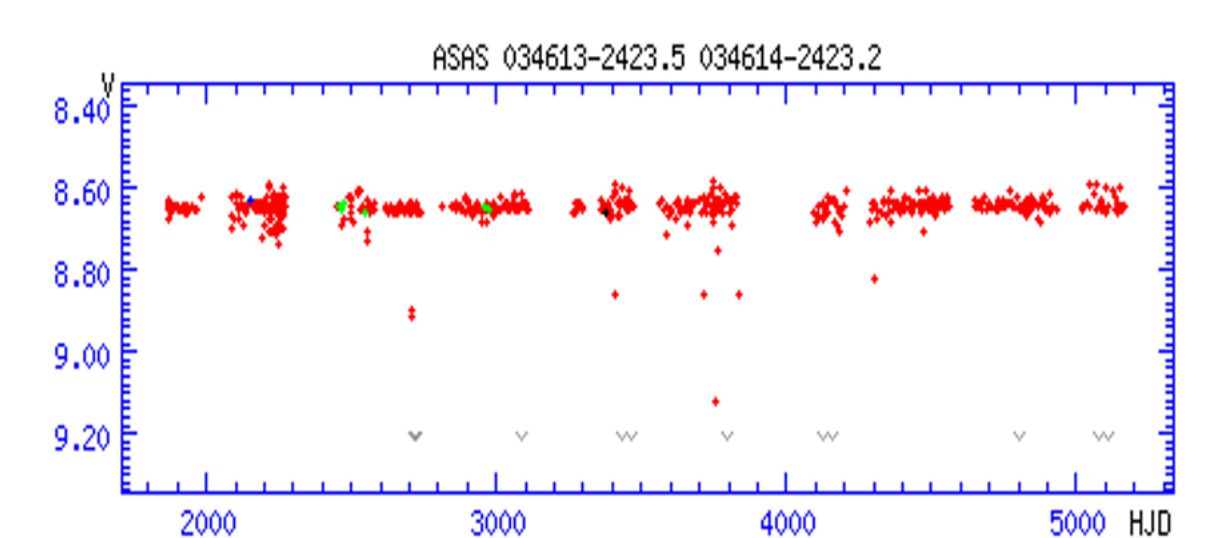


Figure 2. ASAS light curve of *S For* demonstrating its constant behavior. Courtesy of VSX.

2.2 Novae in Aquila

But there is an even more interesting variable star connection in *Sunstorm*, to the constellation Aquila. A computer model uncovers that the solar outburst was caused by a brown dwarf/super-jupiter that had been intentionally collided with the sun by an advanced extraterrestrial civilization, causing an internal solar instability that leads to the earth-threatening outburst. The original source of the brown dwarf/super-jupiter is determined to be Altair in Aquila. Astronomers realize that we are not the first civilization to be threatened in this way, pointing to the fact that “over the last three-quarters of a century, about a quarter of the brighter novae – exploding stars – we have observed have been concentrated in one little corner of the sky,” Aquila (Clarke & Baxter 2005, 355). Surprisingly, this was not the first novel to blame Aquila for threats to our solar system. The 1995 Charles Pellegrino and George Zebrowski novel *The Killing Star* features the sterilization of all life in our solar system by an automated extraterrestrial killing force. Only two groups of survivors escape, one of which intentionally blows up the sun in order to eradicate as much of the enemy force as possible. This group of scientists realizes that “All those exploding stars in the constellation Aquila” could have been signs of similar attacks on other star systems (Pellegrino & Zebrowski 1995, 228).

2.3. Statistical Analysis of Historical Novae

A review of the 353 novae catalogued by the Central Bureau for Astronomical Telegrams (CBAT) shows that between 1612-2004 the top constellations for novae outbursts were as follows (Table 1):

Table 1. Observed Nova Outbursts by Constellation, 1612-2004

<u>Constellation</u>	<u>Number</u>
Sagittarius	90
Scorpius	32
Ophiuchus	30
Aquila	26

This includes two outbursts of CI Aql, in 1917 and 2000. A 27th reported “nova” in Aquila (Nova Aquilae 1946 [V0890 Aql]) later turned out to be asteroid N258 Tyche (VSX 2005). The large number of nova outbursts observed in Sagittarius is due to its location in the direction of the center of the galaxy. Scorpius and Ophiuchus are neighboring constellations, with Aquila next up along the plane of our galaxy, explaining the remainder of the data. It is therefore not surprising that these constellations would play host to numerous novae, as noted by Knut Lundmark (1921, 220).

It is instructional to look at the years directly preceding the writing of the two aforementioned novels to see if there are any notable outbursts. Between 1992-4 there were 13 nova outbursts noted by CBAT, with only one in Aquila and six in Sagittarius. None of these were particularly bright. There was another nova in Aquila in 1995, but this one was also below naked-eye visibility at maximum (CBAT n.d.). Between 1999-2001 there were 17 outbursts noted by CBAT, with four in Aquila and five in Sagittarius. The brightest nova during this time frame was actually Nova Velorum 1999 (V382 Vel), which reached magnitude 2.7 (Warner 2006, 1.31).

3. Discussion

3.1 Explaining SciFi’s Fascination with Novae in Aquila

Considering bright novae specifically, we find that of the 26 overall outbursts seen in Aquila, only five reached magnitude 6.0; of the dozen brightest nova outbursts in the 20th century, only one, Nova Aquilae 1918 (V603 Aql), occurred in Aquila, while three (in 1934, 1960, and 1963) were observed in Hercules (Warner 2006, 1.31). However, it is true that Nova Aquilae 1918 was the brightest modern nova, with a maximum brightness at least -0.5 (Johnson et al. 2014, 2) although other sources place it at -1.1 (Warner 2006, 1.31) or even -1.4 (Aitken 1918, 259). As one might expect, it made quite a stir in the astronomical community, with Harlow Shapley noting that it had been discovered by a “hundred or more different observers” (1923, 39). The object was quickly proclaimed the “brightest Nova since Kepler’s Star in Ophiuchus, which appeared in 1604” (Aitken 1918, 259).

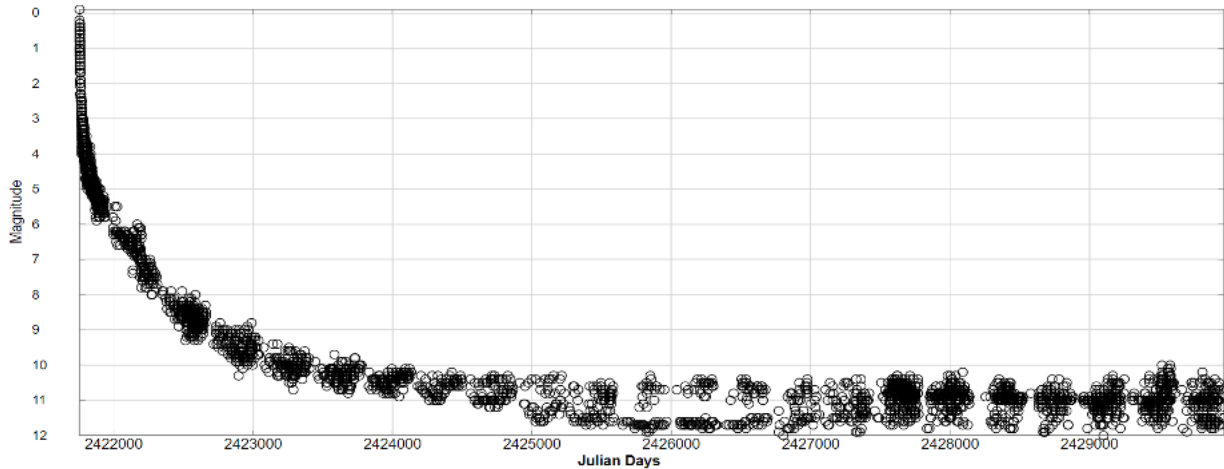


Figure 3. AAVSO visual light curve of V603 Aql (Nova Aquilae 1918).

There are also reasons why this extremely bright nova could be conflated with strange statistics, especially decades after the fact. The 1905 *Harvard College Observatory Bulletin* announcement of the discovery of a nova in the constellation Aquila took great care to distinguish this object, Nova Aquilae No. 2, from the earlier Nova Aquilae No. 1, announced in 1900, both of which were discovered on photographic plates by Williamina Paton Fleming (Pickering & Fleming 271). The brilliant Nova Aquilae 1918 was therefore dubbed Nova Aquilae No. 3, which added to its cultural allure (Pickering 1918, 1). In 1936 Nils Tamm discovered two back-to-back novae in Aquila, one in September, the other in October, a mere six degrees apart in the sky, another curious coincidence (Anon. 1936, 756).

Even relatively dim novae in Aquila have resulted in notoriety in the press. For example, the *Journal of the British Astronomical Association* highlighted the discovery of Nova Aquilae 2001 (V1548 Aql) by UK observer Mike Collins in celebration of the thirteen years of observations it took to make this first discovery, as part in the UK Nova/Supernova Patrol (Hurst 2001, 181). The star only reached magnitude 10.8 (VSX 2017). The second brightest modern nova seen in Aquila was Nova Aquilae 1999 (V1494 Aql), which peaked at magnitude 4.1 and was featured in the December 15, 1999, *Astronomy Picture of the Day* (APOD) image (Nemiroff & Bonnell 1999). These events could have influenced the authors of the later novel, especially if they engaged in even minimal research in the astronomical literature.

3.2 Connections with the Star of Bethlehem

But there is one final science/popular culture connection that may have been a direct influence on *Sunstorm's* specific invoking of Aquila. In his 1999 book *The Star of Bethlehem: an Astronomer's View*, Mark Kidger (269) proposed that the star DO Aql (Nova Aquilae 1925) is a recurring novae and that it had erupted in 5-6 B.C.E. (the modern suggestion for the birthdate of a historical Jesus); he also claimed that at that earlier event it attained a far brighter maximum than the 8.5 observed in 1925 (VSX 2010), thus explaining the famed Biblical "Star of Bethlehem" (henceforth called the Star). While Bradley Schaefer (2013, 227) subsequently quite convincingly

debunked Kidger's hypothesis – on both astronomical and historical grounds – Kidger's book could have certainly served as source material for science fiction writers. This is perhaps even more likely since Kidger himself (1999, 136) references Arthur C. Clarke's 1955 short story "The Star" in his book, a work in which the death of a highly advanced extraterrestrial civilization is caused by a supernova explosion that is viewed on Earth as the Star. The short story was dramatized as an episode of *The Twilight Zone* in 1985. In a case of art imitating science imitating art perhaps, in Clarke and Baxter's *Sunstorm* an initial solar outburst caused by the act of the brown dwarf/super-jupiter being consumed by the sun is their 'scientific' explanation for the Star within the novel.

4. Conclusions

As demonstrated by this research, an analysis of astronomical history in tandem with examples of astronomical references in popular culture can reveal the influence that one has upon the other and can solve the mystery of how astronomical events can be easily conflated by authors, even in works of "hard" science fiction.

References

- 2:22. 2017, directed by Paul Currie, 2929 Productions.
- Aitken, R.G. 1918, *PASP*, **30**, 259.
- Anon. 1936, *Nature*, **138**, 756.
- Arhipova, V., & O. Dokuchaeva. 1970, *IBVS*, No. 494.
- Baade, W., & F. Zwicky. 1934, *Proc. N.A.S.*, **20**, 254.
- Bateson, F.M. 1969, *IBVS*, No. 389.
- Blish, J. 1971, *And All the Stars a Stage*, Avon, New York.
- Cannon, A.J. 1907, *Ann. Astron. Obs. Har. Col.*, **55**, 1-94.
- CBAT. n.d., List of Novae in the Milky Way, http://www.cbat.eps.harvard.edu/nova_list.html.
- Clarke, A.C., 1955. *Infinity Science Fiction* **1**(1), 120.
- Clarke, A.C., & S. Baxter. 2005, *Sunstorm*, Ballantine, New York.
- Hamilton, E. 2005, *The Best of Edmond Hamilton*, ed. Leigh Beckett, Phoenix Pick, Rockville.
- Hurst, G.M. 2001, *J. Br. Astron. Assoc.*, **111**, 181.
- Johnson, C.B. et al. 2014, *ApJ Lett.*, **780**, 25.
- Kidger, M. 1999, *The Star of Bethlehem: an Astronomer's View*. Princeton UP, Princeton.
- Lovecraft, H.P. 2009, Beyond the Walls of Sleep, <https://www.hplovecraft.com/writings/texts/fiction/bws.aspx>.
- Lundmark, L. 1921, *PASP*, **33**, 220
- Nemiroff, R., and J. Bonnell 1999, A Nova in Aquila, <https://apod.nasa.gov/apod/ap991215.html>.
- Niven, L. 1974, "The Fourth Profession," *A Hole in Space*, Ballantine Books New York.
- Nova*. 2013, directed by Ezequiel Romero and Bruno Teixdor, #littlesecretfilm.

- Payne-Gaposchkin, C. 1952, *Ann. Astron. Obs. Har. Col.*, **115**, 219.
- Pickering, E.C. 1918, *Har. Col. Obs. Bull.*, **662**, 1.
- Pickering, E.C., & W.P. Fleming. 1905, *ApJ*, **22**, 271.
- Serviss, G.P. 1909, *Astronomy with the Naked Eye*, Harper and Brothers, New York.
- Schaefer, B.E. 2013, *Obs.* 133, 227.
- Shapley, H. 1923, *Proc. N.A.S.*, **9**, 39.
- Smith, George O., 1959, *Troubled Star*, Galaxy Publishing, New York.
- VSX. 2005, V0890 Aql, <https://www.aavso.org/vsx/index.php?view=detail.top&oid=2029>.
- VSX. 2017, V1548 Aql, <https://www.aavso.org/vsx/index.php?view=detail.top&oid=2687>.
- VSX. 2022, S For, <https://www.aavso.org/vsx/index.php?view=detail.top&oid=14225>.
- Warner, B. 2006, *Astron. & Geophys.*, **47**, 1.29.
- Williams, S. 2011, *Soc. Hist. Astron. Bull.*, **21**, 33.

Modelling Pulsating Stars

Philip Masding and Robin Leadbeater

British Astronomical Association; philipmasding@gmail.com

Subject Keywords

Hydrodynamic codes; radial velocity measurement; spectroscopy; pulsating stars; SZ Lyn

Abstract

Pulsating stars have been studied using non-linear hydrodynamic codes since the pioneering work of Robert Christy in the 1960's. Modern codes include improvements such as allowing for convection but there is a penalty in terms of computation speed and for some stars convection is not significant. In this work a new version of the Christy program has been developed which can run hundreds of star models to convergence in a day or two of computer time. This allows overall patterns of behaviour to be studied and suitable models for individual case stars to be identified. The star SZ Lyn was chosen as a test case for the model. Light curve and radial velocity data were obtained for this star using amateur equipment. A run of 625 parameter sets (mass, luminosity, effective temperature and hydrogen fraction) identified the best fit parameters for SZ Lyn. Model results show a good fit to the observed data in terms of amplitude, period and shape of the light and velocity curves. In this paper we report on the model developed by PM and radial velocity observations by RL.

1. Introduction

Pulsating variable stars are very important in astronomy particularly because the period-luminosity relationship is vital for determining distances. The first Cepheid was discovered by John Goodricke in 1784 but little was known about the fundamental mechanism of variation until the early 20th century. Eclipses by binary companion stars were suggested but did not explain the shape of the light curves. This led to the proposal by Shapley that the variability was due to intrinsic pulsation of the star (Shapley, 1914). Beginning in 1918 the scientist and mathematician Arthur Eddington developed the heat engine theory to explain the pulsation (Eddington, 1918).

With their importance in distance determination, as exemplified by Hubble using Cepheids to establish that the Andromeda galaxy is a separate star system to the Milky Way, there was an obvious incentive to reproduce the behaviour of real stars using Eddington's theory. Unfortunately, the equations cannot be solved analytically and linear solutions can only explain the amplitude and period of the brightness curves rather than their shape. However, with the advent of powerful computers in the 1960's and the numerical mathematical techniques developed during the Manhattan project in the second world war it became possible to calculate a solution based on Eddington's theory. The pioneer in this area was Robert Christy. His work

showed that it was possible to predict many of the complex features seen in variable star brightness and radial velocity curves (Christy, 1964).

The motivation of this work is to develop a modern version of Christy's code and exploit the speed of modern computers to run hundreds of trial models to match observations. Amateur astronomers have a long history of observing variable star light curves but in recent years it has become possible to observe the radial velocity as well using a spectrograph on a small telescope. The combination of a model which can run quickly on a personal computer and observational data to go with it means that amateurs can contribute to the understanding of pulsating stars.

2. The Mechanism of Variability

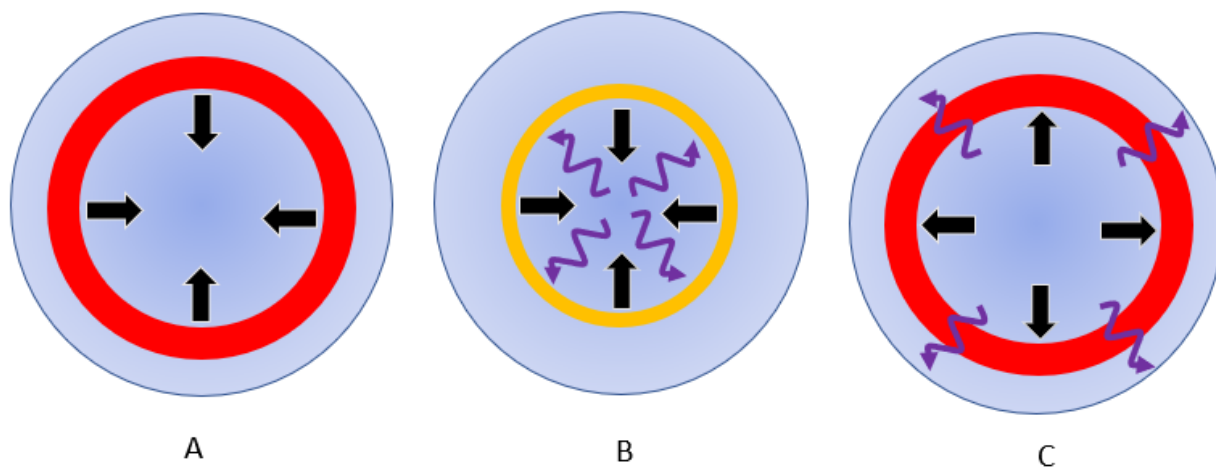


Figure 1. Illustration of Eddington's heat engine theory

A simple illustration of Eddington's theory is shown in Figure 1. In 1A a zone of a star is not in hydrostatic equilibrium such that the gravity force exceeds the supporting pressure so the zone falls. As it falls it is compressed and becomes denser and more opaque, trapping radiation in the zone below. Eventually at 1C the trapped radiation increases the pressure below the zone so much that it is forced upwards whereupon it becomes relatively transparent, allowing the radiation to escape and the cycle will repeat.

A problem with the initial version of the theory is that as the zone falls and is compressed it becomes denser and hotter. Although increasing density is associated with higher opacity, increasing temperature causes lower opacity and the temperature effect will predominate. An explanation was provided by Zhevakin (Zhevakin, 1953) who showed that in some stars temperatures at critical depths are just right to cause ionisation of hydrogen and helium. This ionisation absorbs energy without a temperature rise, leaving the increasing density to raise opacity. This is the so-called kappa mechanism which explains why only some stars pulsate.

3. The Computer Model

By the 1960's computers had become powerful enough to calculate a numerical solution to the pulsating star theory. Also, new methods from the atom bomb project could now be used to solve the equations for gases under extreme conditions. One of the people who had worked on the bomb project, Robert Christy, had by this time moved to Caltech and he developed a model using the IBM 7090 computer (Figure 2) at the university.



Figure 2. An IBM 7090 computer in the 1960's (credit NASA)

In this project a new version of Christy's code was developed in C++ to take advantage of the speed of a modern PC which is typically 10,000 times faster than the IBM7090.

This type of model is 1 dimensional which means that the star can pulsate in the radial direction only. In order to allow this, the star is divided up into a number of mass zones or shells from the surface down to a depth where any pulsation is negligible which is typically 15% of the total radius. The inner boundary condition is then zero velocity and a constant radiation flux from the nuclear reactions in the core. A simplified schematic of the new code is shown in Figure 3.

There are 3 main parts to the solution beginning with the static solver. Solving the static model requires finding a set of temperatures and zone radii which achieve hydrostatic equilibrium or a balance of gravity and pressure forces. The other one-off calculation is to create a 2D look-up table of properties of the gas mixture at various temperature and densities. This calculation requires a solution of the Saha equations to determine the state of ionisation of the hydrogen, helium and metal mixture.

In the dynamic stage the model steps forward through time with a variable step length dependent on the Courant condition or time for sound to cross the narrowest zone. Each cycle begins by

solving the energy balance for the temperature using an iterative technique. The velocity and radius are then updated by explicit numerical integration.

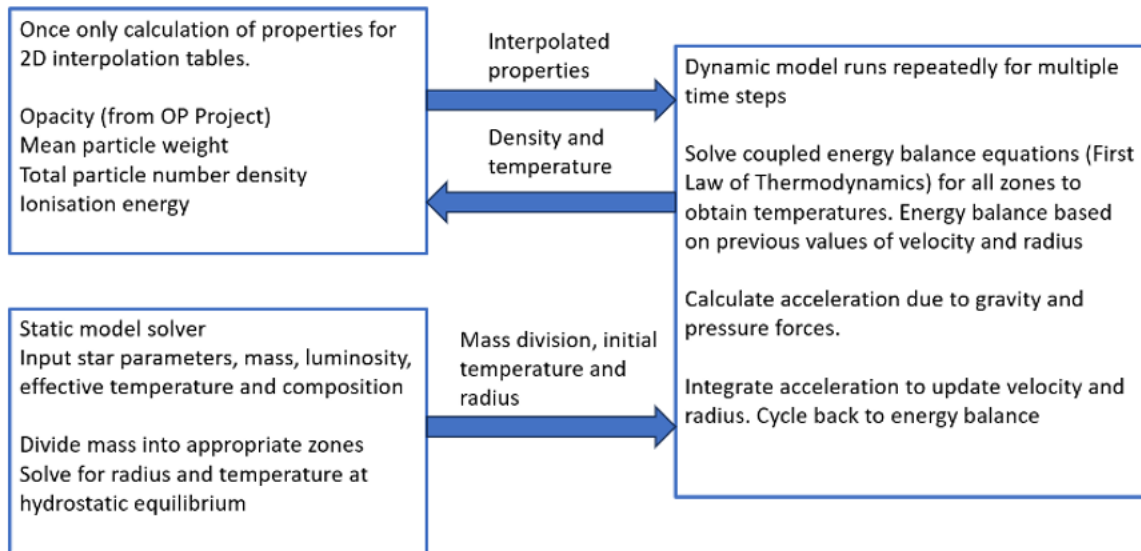


Figure 3. The model structure

4. Observations for a Test Star SZ Lyn

In order to test the model, the authors obtained light curve and radial velocity data for the high amplitude δ Scuti star SZ Lyn. This star is conveniently placed for northern hemisphere observers in the spring and has a short 2.892-hour period which means all observations can be obtained in one night. At magnitude 9.08 to 9.72 it is also bright enough to allow the radial velocity to be measured.

Data for the light curve was obtained unfiltered using an 80mm refractor and Atik 313+ camera. These observations were reduced using standard techniques. The radial velocity measurements are more involved and are the subject of the next section.

4.1 Measurement of radial velocity

The star-centric radial pulsation velocity data for SZ Lyn used in this paper were derived from radial velocity measurements on spectra recorded using a LHIRES III spectrograph (resolving power $R = 7000$) mounted on a 0.28m aperture telescope. The wavelength covered was 443-458 nm and the exposure time for each measurement was 600s. To minimise the effects of any drift in the spectrograph, the wavelength calibration was based on the average of calibration lamp spectra taken before and after each star spectrum.

For SZ Lyn, 34 spectra were recorded during the night of 7-8th March 2023 covering 2 complete pulsation cycles. The signal/noise ratio in each spectrum was typically 35 per resolution interval.

The spectra were individually reduced using ISIS software [isis-software \(astrosurf.com\)](https://isis-software.astrosurf.com). Typical spectra recorded around maximum and minimum radial velocity are shown in Figure 4. All spectra are available to view and download from the British Astronomical Association Spectroscopy Database (<https://britastro.org/specdb/>).

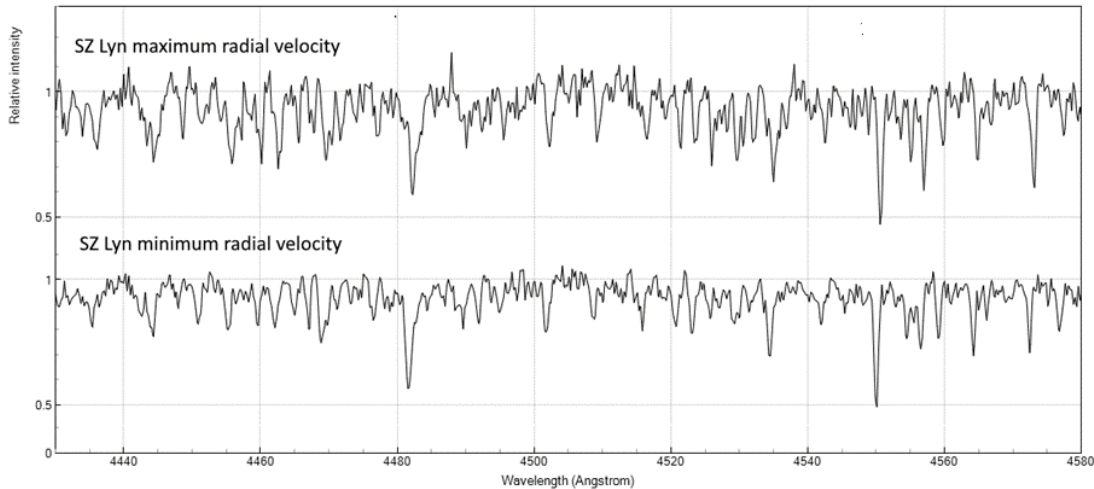


Figure 4. Spectra of SZ Lyn

The relative radial velocities were measured by the cross-correlation method, using the tool in ISIS. The first spectrum in the series was used as the reference template. The velocities and observation times were then heliocentric corrected.

The data were folded into a single cycle using a period 0.12053 day for SZ Lyn as published in the International Variable Star Index (<https://www.aavso.org/vsx/>) and the phase referenced relative to the time of maximum brightness. The velocity offset (due to the motion of the star and the arbitrary choice of reference spectrum) was removed. The resulting measured radial velocities are plotted in Figure 5.

A projection factor was applied to account for the fact that the measured velocity is an average over the stellar disc of the component of the star-centric radial pulsation velocity in our direction. (This component reduces towards the limb and hence the average measured velocity is smaller than the pulsation velocity.) This factor also includes the effect of limb darkening among other factors and its precise value remains of some debate and may to some degree be star specific (Borgniet, 2019). Here we have adopted a value of 1.35 with an uncertainty of $\sim 5\%$.

Finally, the sign of the velocity was reversed to change the origin of the reference coordinates from heliocentric to star centric.

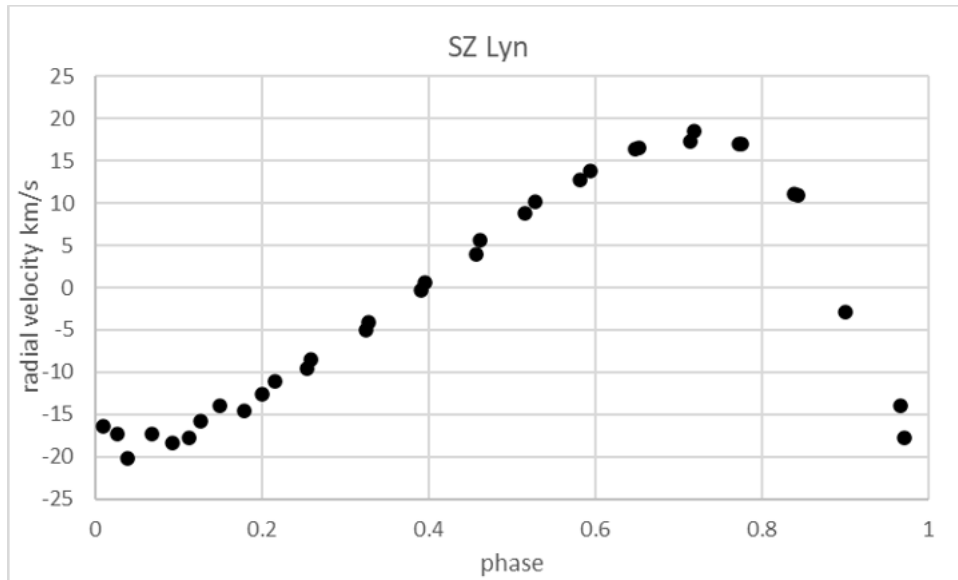


Figure 5. Radial velocity for SZ Lyn

The stochastic uncertainty of the individual measured pulsation velocities is 2 km/s for SZ Lyn, estimated from the residuals to a quadratic fit over the falling part of the pulsation velocity curve. There is an additional systematic uncertainty arising from the uncertainty in the value of the projection factor.

Note: SZ Lyn is a binary system with a period of 3.1 years and so the orbital motion will affect the observation times and measured radial velocities and any light from the secondary would be included in the brightness measurements. (Moffett, et al., 1988). The timescale covering these observations was sufficiently short compared with the orbital period such that effect on the timings and radial velocity are negligible and were not corrected for. There is no evidence of the secondary in the visible spectrum which implies the secondary is at least 2 magnitudes fainter (Bardin & Imbert, 1984). A 2-magnitude fainter secondary would reduce the observed magnitude range by 0.09. Here we have assumed no significant contribution from the secondary in the brightness measurements.

4.2 Model results

The model requires a number of key parameters to define a star. For SZ Lyn suitable literature values are $7200K < T_e < 7800K$, $0.91M_{\odot} < M < 1.74M_{\odot}$ and $2.3R_{\odot} < R < 2.87R_{\odot}$ (Adadduriya, et al., 2020). In order to find the best fit to the observational data, the model was run with 5 values of each parameter spanning the quoted range of uncertainty. In addition, the composition was varied with 5 values of hydrogen fraction in the range $0.6 < X < 0.73$ at fixed $Z=0.015$. As a result, the total number of cases computed was 625. The model used a 74-zone envelope with 20km/s initial velocity imposed at the surface.

Best fit physical parameters from all these cases are $T_e = 7500K$, $R = 2.81R_\odot$, $M=1.57M_\odot$ and $X = 0.61$. With these values the model result show excellent agreement with observations made by the authors in March 2023 (Figure 6).

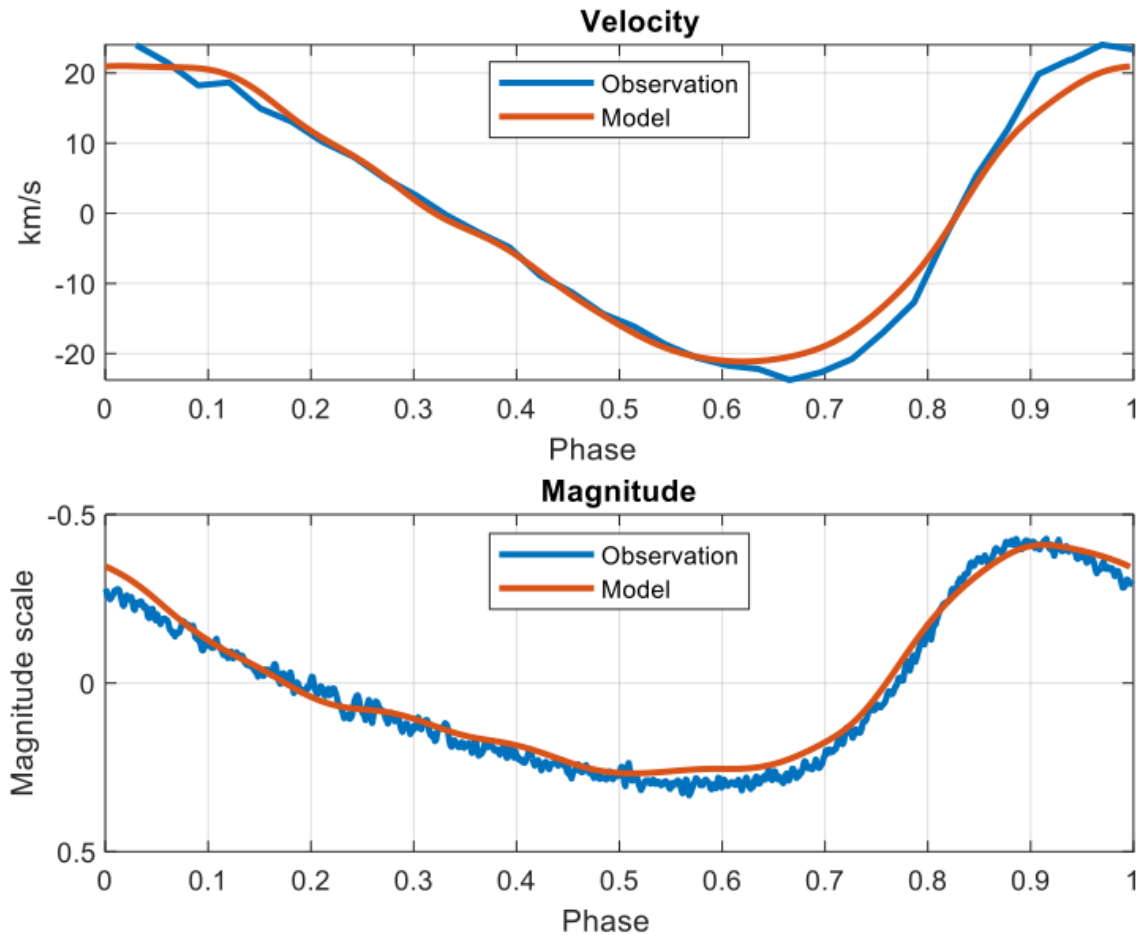


Figure 6. Model and Observation for SZ Lyn

4.5 Inside the star

Observations are restricted to what happens at the surface of the star, but with the model we can predict what is happening throughout the envelope. In Figure 7 we see the velocity of the zones, with yellow colours indicating positive velocity as the star expands and blue indicating negative velocity as it contracts. Notice that significant velocity only extends down to about 75% of the total radius.

Figure 8 shows the variation of Hell as a fraction of total helium. As such the bright yellow band represents 100% Hell and this band is broadest at maximum radius. The transition from Hel to Hell always takes place over a short distance near the surface whereas the transition from Hell to Hell is at a deeper level and takes place over a larger distance.

The variation of opacity within the star has interesting patterns as shown by Figure 9. On this scale the cycling of hydrogen ionisation is poorly resolved since it takes place so close to the surface. In deeper zones the variation in opacity due to helium and the Z-bump leads to complex cycling.

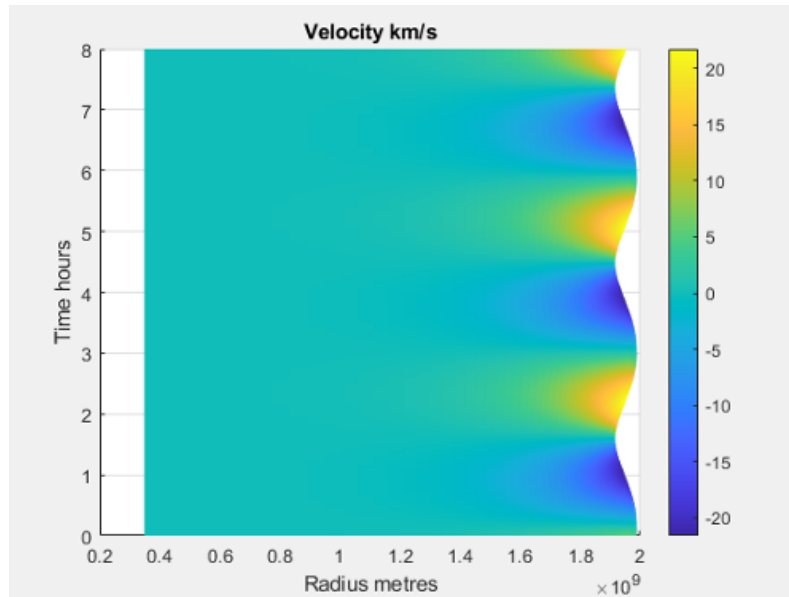


Figure 7. Contour plot of radial velocity as a function of radius and time inside the star

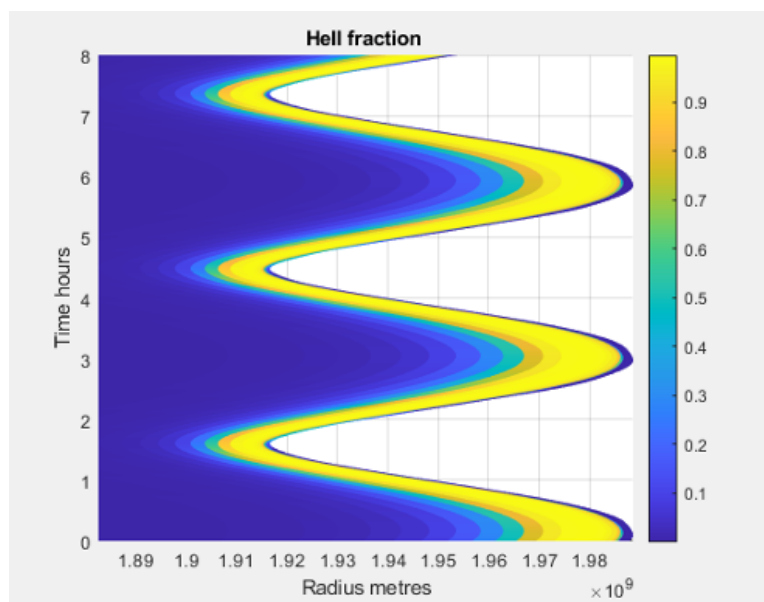


Figure 8. Contour plot of variation of Hell fraction as a function of radius and time inside the star

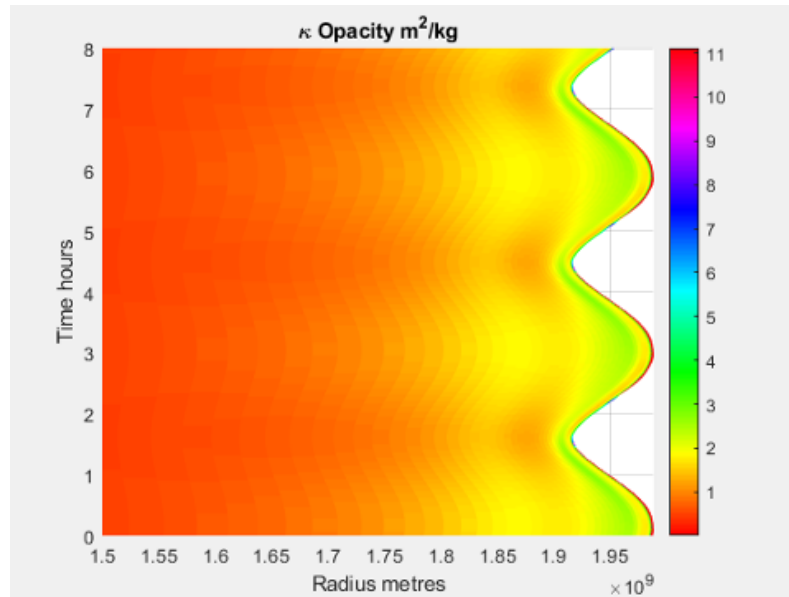


Figure 9. Contour plot of opacity as a function of radius and time inside the star

5. Conclusions

This work has demonstrated that a new implementation of the Christy hydrodynamic code can run extremely fast on a modern computer. This speed opens up the possibility to test hundreds of sets of the basic input parameters of mass, luminosity, effective temperature and composition and obtain a best fit model for observed light and radial velocity curves for a given star.

Amateur astronomers have a long history of observing light curves but in recent years spectrographs such as the LHIRES III have become available which are capable of measuring the radial velocity of stars down to at least magnitude 10 using telescopes of around 0.3m aperture. This means that amateur data can be used to fully test the model.

We obtained observational results for SZ Lyn as a test case for the model. This star is relatively bright and has a short period making it ideal to observe. In this case we screened several hundred parameter sets and found a set which very accurately fits the observed data and is within error bounds for each parameter as quoted in the literature.

In future work it is hoped to observe and fit models to more stars. The original Christy model does not include convection which does limit its applicability, so a future plan is to include a simple representation of convection in the new code.

Acknowledgements

PM would like to thank Joyce Guzik for her encouragement in submitting this work to the AAVSO conference and also to thank Edward Masding for his help with C++ coding and building a fast computer.

This research has made use of the International Variable Star Index (VSX) database, operated at AAVSO, Cambridge, Massachusetts, USA.

References

- Adadduriya, J. et al. 2020, Asteroseismology of SZ Lyn using multiband high time resolution photometry from ground and space, *Monthly Notices of the Royal Astronomical Society*, 502, 541.
- Borgniet, S. et al. 2019, Consistent radial velocities of classical Cepheids from the cross-correlation technique, *Astronomy & Astrophysics*, 631, A37.
- Christy, R F. 1964, The Calculation of Stellar Pulsation, *Rev. Mod. Phys.*, 36, p. 555.
- Eddington, A. S. 1918, On the pulsation of gaseous stars and the problem of the Cepheid variables, *Monthly Notices of the Royal Astronomical Society*, 79, pp. 2 - 22.
- Moffett, T.J. et al., 1988. Orbital and photometric properties of SZ Lyncis, *The Astronomical Journal*, 95, 1534
- Shapley, H. 1914, On the Nature and Cause of Cepheid Variation, *The Astrophysical Journal*, 40, pp. 448-465.
- Zhevakin, S.A. 1953, Theory of Cepheids, *Russ. Astron. J.*, 30, 161.

Period Change Updates for δ Scuti Variable DY Her

Abigale Moen, Matthew Craig, Emily Watson, and Tanner Weyer

Minnesota State University Moorhead, 1104 7th Ave S, Moorhead, MN, 56563, USA;
abigale.moen.2@go.minnesota.edu

Subject Keywords

AAVSO International Database; Photometry, CCD; Cataclysmic Variables; stars: individual (DY Her)

Abstract

This study observes period changes of DY Her, a high amplitude δ Scuti variable star with a period of 0.148631353 days. DY Her has been observed to have a slow overall period change from data gathered over several decades. Using light curve data taken over multiple nights at Paul P. Feder Observatory and observations of DY Her obtained from AAVSO from the past 20 years, the observed and calculated maxima were found, and an O-C graph was created to observe the period changes. A predicted O-C curve from past work was plotted alongside the O-C data in this study to see if the more recent data on DY Her's period changes remain consistent with prior data on the star. The new O-C observations agree with previous analysis of the period changes and show that the period of DY Her is slowly decreasing.

1. Introduction

δ Scuti stars are a type of variable star classified by their short periods, ranging from 0.02 to 0.3 days. They are pulsating variables of spectral type A and F that fall on the main sequence inside the downwards extension of the Cepheid Instability strip. High Amplitude δ Scuti (HADS) are a type of δ Scuti variable that typically have amplitudes greater than 0.3 (Percy 2007).

DY Her is a HADS found in the constellation Hercules, with RA and Dec of 16h 31m 17.95 +11° 59' 52.5. It has a period of 0.148631353 days, which is around 3.5 hours, and a magnitude range of 10.15-10.66 from VSX (Watson 2006). Many light curve observations have been taken for DY Her since its first observation, but observations on any period changes of DY Her have not occurred as much.

Period changes within a variable star are thought to occur due to the stellar evolution of the star. Period changes are slow, but they have a cumulative effect, allowing them to be measurable (Percy 2007). The way to measure period changes within a star is to create an O-C diagram, where the time of calculated maximum is subtracted from the time of observed maximum. The slope of the diagram shows if the star's period is changing; if the slope is a horizontal line, there is no period change present; if the slope is linear, there is a change in period, but the assumed initial period of the star is incorrect; and if the O-C graph has a parabolic slope, then the period is

changing at a constant rate, with a concave down curve meaning the period is decreasing and a concave up curve meaning the period is increasing.

O-C observations of DY Her have been made before, with data spanning from 1950 to 2003 (Derekas et al. 2009), but AAVSO currently has light curve data on DY Her spanning from 2003 to present day that has not been analyzed to see period changes. The purpose of this project is to create more current O-C observations of DY Her while also comparing them to past observations to see if the change in period remains consistent.

2. Data collection and analysis

2.1 Methods

This study uses data taken by the authors at the Paul P. Feder Observatory at the Minnesota State University Moorhead Regional Science Center and data retrieved from the AAVSO. In both cases the goal was to measure as many times of maximum as possible for constructing an O-C curve.

2.1.1 Feder Observatory data

Observations were done of DY Her on the dates listed in Table 1. The telescope is a 16" Cassegrain manufactured by DFM Engineering, with an Andor Alta CG16-M camera and photometric filters. All observations were done in a single filter, Sloan r, because the filter wheel was not functioning at the time. Dark, bias and twilight flats were taken each night, and each night's data were reduced using standard techniques with the software ccdproc.

A relative flux was calculated for DY Her on each night using the method described by Collins (2017). All non-variable stars in the field that were in the APASS DR9 catalog (Henden 2015) were used as comparison, with the caveat that several portions of the CCD were excluded because of the environmental issues described in Table 1 that affected parts of the field of view. The only parts of the CCD used on each night were those that were unobstructed on that night. The location of the obstructions was different for some of the nights, which means that the set of comparison stars was different for each night. As a result, the relative flux cannot be directly compared across nights.

To determine the time of maximum on each night, a 5th degree polynomial was fit to the region near the maximum. The maximum of the fit was used as the time of maximum. Light curves for each night are in Figure 1.

Table 1. Data collection at Feder Observatory

UTC date of start of observations*	Notes on camera obstructions
June 11, 2023	Caddisfly blocking right portion of frame
June 12, 2023	Caddisfly blocking right portion of frame
June 16, 2023	Caddisfly part blocking top portion of frame
June 20, 2023	Caddisfly part blocking top portion of frame; seed blocking circular region in left-center part of frame

*The hyperlink for each night is to a gallery of the uncalibrated images for the night. The format for these links is https://physics.mnstate.edu/feder_gallery/YYYY-MM-DD/, where the month and date are local date, typically a day before the UTC data in the table.

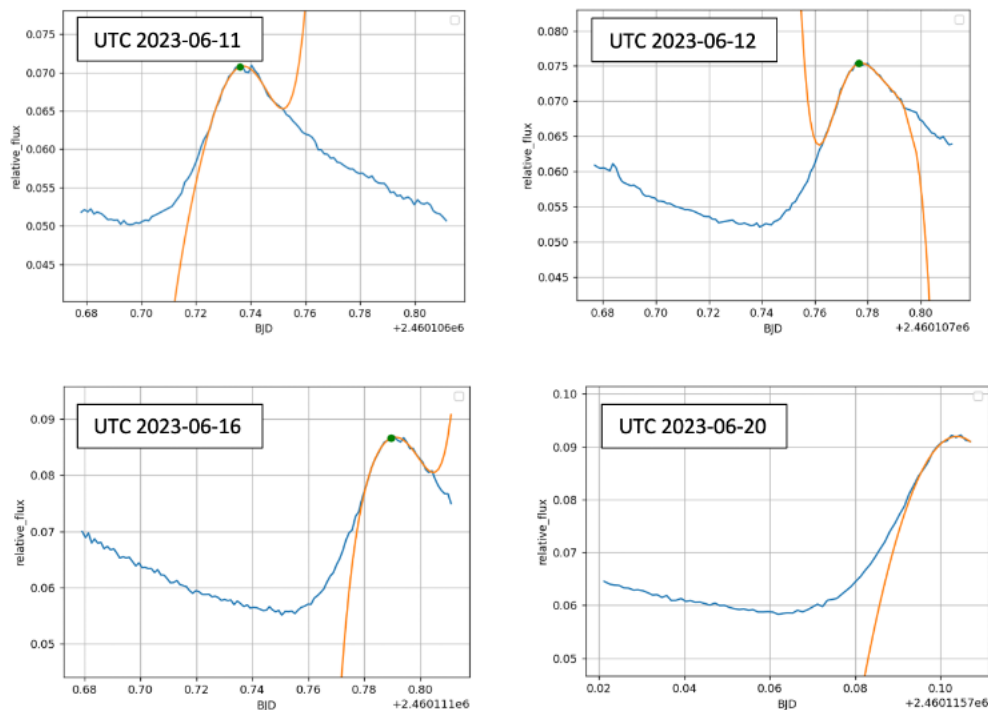


Figure 1. Relative flux from DY Her on each of the four nights it was observed. In each plot the blue curve is the relative flux, the gold curve is a 5th order polynomial fit to the region near the peak, and the dot marks the location of the maximum of the fit.

2.1.2 AAVSO data

Data on the star DY Her were downloaded from AAVSO's website around mid-summer of 2023. Data taken using a V-band filter were specifically selected, as observations using the V filter were the most numerous and would allow the observations to be consistent with previous data on DY Her. The data ranged from early 2003 to May of 2023.

The selected data were then plotted together on one graph (see Figure 2.A). A running average of the data were then created to reduce noise in the data. The running averages were used so

the code would have an easier time automatically finding a range around each of the peaks to fit a polynomial curve to, as it would sometimes mistake noise in the data to be a peak. When a range around the peak of the light curves was found, a 5th degree polynomial curve was then applied to every single one. Then, the peaks of each curve fit were found and recorded. The times of these peaks were then taken and translated into a Heliocentric Julian Date (HJD) on the UTC time scale.

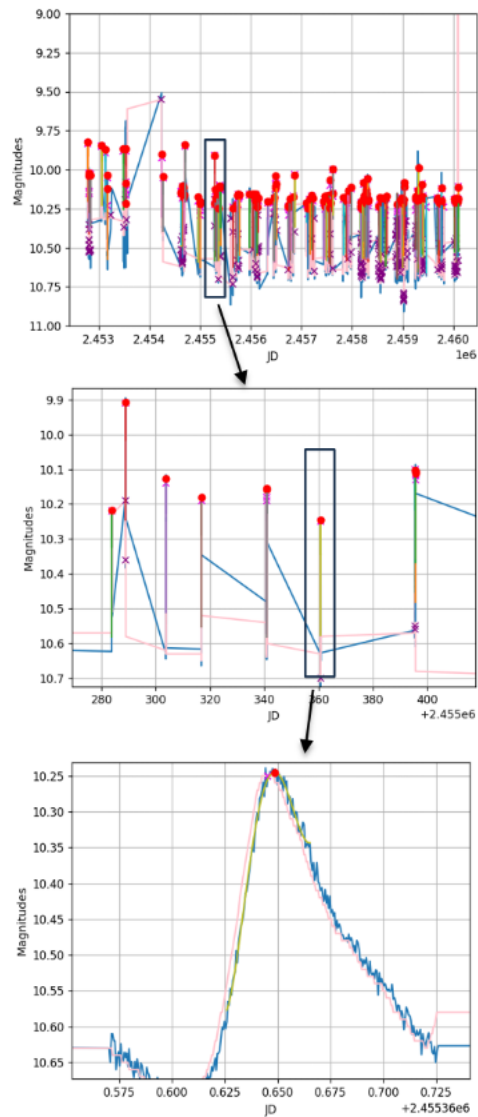


Figure 2. Plot A (top) shows every light curve of DY Her available on AAVSO's website. Plot B shows the area of plot A that is marked out by a black box. The purple "x" on plots A and B are data excluded from analysis as they were false positive peaks identified by the code. Plot C is then a zoomed in image of plot B from the highlighted box showing a single light curve. The blue line is the light curve of DY Her from the AAVSO data. The pink curve is the running average of the blue line. The yellow line on Plot C is a 5th degree polynomial fit of the blue line and the red dot is the point of maximum of the polynomial fit.

2.1.3 Ephemeris

We adopt the ephemeris used in Derekas et. al. (2009)

$$HJD_{MAX} = 2433439.4871 + 0.1486309 \times N \quad (1)$$

for calculating the cycle number N for each maximum.

2.2 Results

Times of maximum derived from the Feder data are listed in Table 2. The times of maximum for the Feder and AAVSO data are plotted in Figure 3.

Table 2. Times of maximum derived from Feder data

UTC date at start of observation	Time of maximum, BJD (TDB time scale)	Time of maximum, HJD (UTC time scale)
June 11, 2023	2460106.738487	2460106.737686
June 12, 2023	2460107.779942	2460107.779141
June 16, 2023	2460111.792383	2460111.791582
June 20, 2023	2460115.803809	2460115.803008

3. Conclusions

Using the observed times of maximum gathered from the AAVSO data and the data from Section 2.2, the calculated times of maximum can be found using the period 0.148631353 days and the epoch 2433439.4871 (HJD) (Derekas et al. 2009). Then the calculated times of maximum can be subtracted from the observed times of maximum to find the O-C. The O-C is then plotted against cycle number.

The O-C diagram seen in Figure 3 is plotted with a 2nd degree polynomial curve with the equation (Derekas et al. 2009):

$$(O - C)_{HJD} = -0.001 \pm 0.003 + 3.98 \times 10^{-7} \cdot N - 8.98 \times 10^{-13} \cdot N^2, \quad (2)$$

where N is the cycle number. This is the same equation used in the paper that reported the initial O-C observations.

The recent O-C observations of DY Her agree with prior observations of the star, as most of the data points fall within the error bars of the fit curve in Figure 3. Ideally, we would plot the old data with the new data and create a new fit curve that would better show the period changes in DY Her, which is the next step in this project.

Due to the fact that the slope of the O-C graph is a concave down 2nd degree polynomial curve, DY Her's period is decreasing at a constant rate, as mentioned in Section 1.

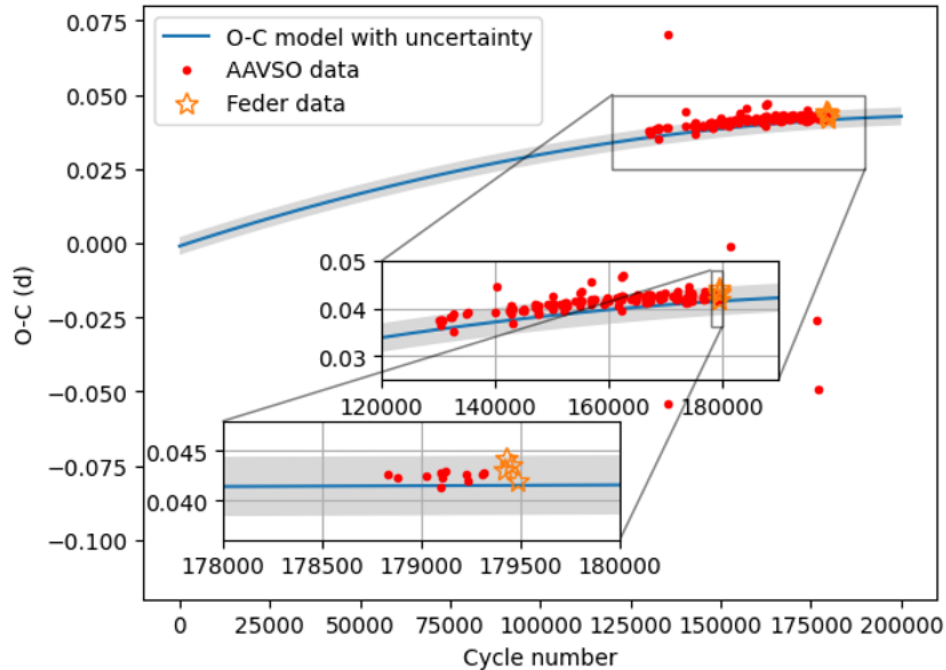


Figure 3. Plot A (top) shows the O-C observations plotted against the cycle number. Equation 2 is plotted along with the O-C graph, with the blue line being the actual equation, and the grey around it being the error. Plot B shows plot A zoomed in on an area highlighted by the black box to better show the data. Plot C shows a further zoomed in area of plot B, with yellow stars highlighting data taken from the Paul P. Feder Observatory.

Acknowledgements

Abigale Moen, Emily Watson, and Tanner Weyer were supported by an award from the Strong Endowment at Minnesota State University Moorhead. We acknowledge with thanks the variable star observations from the AAVSO International Database contributed by observers worldwide and used in this research.

References

- Astropy Collaboration, 2022, “The Astropy Project: Sustaining and Growing a Community-oriented Open-source Project and the Latest Major Release (v5.0) of the Core Package”, *The Astrophysical Journal*, 935, 2. doi:10.3847/1538-4357/ac7c74
- Collins, K. A., Kielkopf, J. F., Stassun, K. G. & Hessman, F. V. 2017, AstrolmageJ: Image Processing and Photometric Extraction for Ultra-precise Astronomical Light Curves, *The Astronomical Journal*, 153, 77
- Derekas, A. et al. 2009, Binariness and multiperiodicity in high-amplitude δ Scuti stars, *Monthly Notices of the Royal Astronomical Society*, 394, Issue 2, pp. 995–1008, <https://doi.org/10.1111/j.1365-2966.2008.14381.x>
- Harris, C.R., Millman, K.J., van der Walt, S.J. et al. 2020, Array programming with NumPy, *Nature* 585, 357–362. DOI: 10.1038/s41586-020-2649-2

- Henden, A.A., Levine, S., Terrell, D., Welch, D.L. 2015, American Astronomical Society, AAS Meeting #225, id.336.16
- Percy, J. R. 2007, *Understanding Variable Stars*, pp. 68-71 and pp. 182-186
- Watson, C.L., Henden, A.A., & Price, A. 2006, The International Variable Star Index (VSX), Society for Astronomical Sciences Annual Symposium, 25, 47

Developing Algorithms to Determine an Asteroid's Physical Properties and the Success of Deflection Missions

Arushi Nath

Founder, MonitorMyPlanet, Toronto, Canada; arushi@monitormyplanet.com

Subject Keywords

Near-Earth Asteroids, Python Algorithms, DART Mission, Open Data, Citizen Scientists, Asteroid Characterization

Abstract

The rate of discovery of near-earth asteroids outpaces current abilities to analyze them. Knowledge of an asteroid's physical properties is essential to deflect them. I developed open-source algorithms using images from robotic telescopes, open data, and math to determine asteroids' size, rotation, and strength. I took observations of the Didymos binary asteroid, and my algorithm determined its size to be 820 metres, with a 2.26-hour rotation period and rubble-pile strength. I measured a decrease in the mutual orbital period after impact by the 2022 NASA DART Mission confirming successful deflection. External sources validated the findings. Every citizen scientist is now a planetary defender.

1. Introduction

There are over 32,000 known near-earth asteroids as of May 2023, and hundreds of new ones are discovered every month. See Figure 1. Orbits of near-earth asteroids can enter Earth's neighborhood (within 1.3 astronomical units of the Sun), raising the possibility of collisions. If an asteroid were on a collision course with the Earth, the deflection strategy would depend on the asteroid's physical properties, such as its size, rotation period, strength, and the presence of a moonlet. Unfortunately, the pace of discovery of near-earth asteroids currently outpaces the ability of astronomers to analyze them.

Planetary defense is being taken seriously by national governments and space agencies. On 26 September 2022, NASA's Double Asteroid Redirection Test (DART) mission successfully tested its first planetary defense by impacting moonlet Dimorphos of the binary asteroid (65803) Didymos with a fridge-sized spacecraft and changed its orbital path. In December 2026, the European Space Agency's (ESA) Hera Mission will rendezvous with Didymos to determine the momentum transfer efficiency of the DART mission. In 2025 the China National Space Administration (CNSA) will launch an impactor to change the trajectory of the earth-crossing asteroid 2020 PN1^[2].

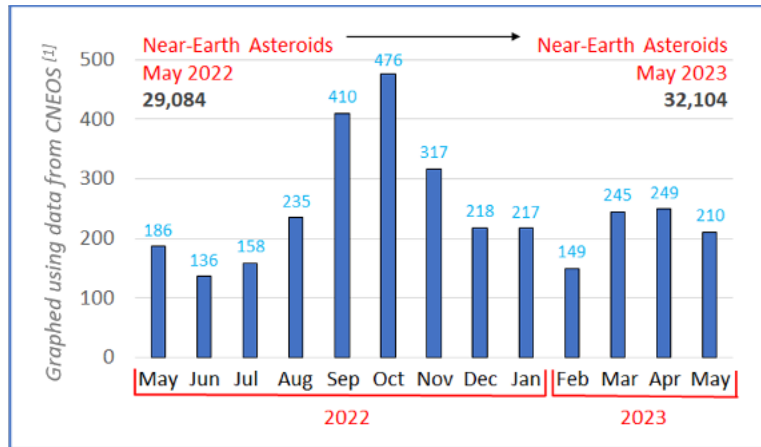


Figure 1. Hundreds of New Near-Earth Asteroids are Discovered Every Month

If we could make it easier for citizen scientists and backyard astronomers to determine the physical properties of near-earth asteroids, it would accelerate the pace of analysis. Every citizen scientist could become a planetary defender, which could mean the difference between planetary defense and planetary extinction.

2. Project Goals and Objectives

My project had two goals:

1. Develop algorithms that citizen scientists can use to accurately determine an asteroid's physical properties using observations from robotic telescopes, open data, and school-level math.
2. Apply the algorithms to a real-world scenario to determine the physical properties of the Didymos binary asteroid and measure the success of NASA's DART Mission in deflecting Dimorphos.

The specific objectives were:

1. Develop photometry algorithms that can combine observations from multiple robotic telescopes to:
 - Generate composite asteroid light curves.
 - Determine the absolute magnitude, rotation period, size, and strength of asteroids and mutual orbital period in the case of binary asteroids.
2. Image Didymos binary asteroid system before, during and after the impact by NASA's DART mission to:
 - Determine the physical properties of the binary asteroid Didymos and its moonlet Dimorphos.
 - Study the ejecta tail of Dimorphos after the impact.

- Determine the change in the orbital path of Dimorphos to confirm successful asteroid deflection.

3. Data Collection: Observations from Robotic Telescopes

3.1 Imaging Binary Asteroid Didymos Before, During and After the Impact by the DART Mission

I wrote research proposals for the Faulkes Telescope Project, the American Association of Variable Star Observers (AAVSO), the Canadian Space Agency, and the Burke Gaffney Observatory to get observation time on their telescopes.

I created observation plans and took over 55 hours of observations of the Didymos binary asteroid over several months (before, during and after the impact) using robotic telescopes across four continents in Australia, Canada, Chile, and Spain. See Figure 2.

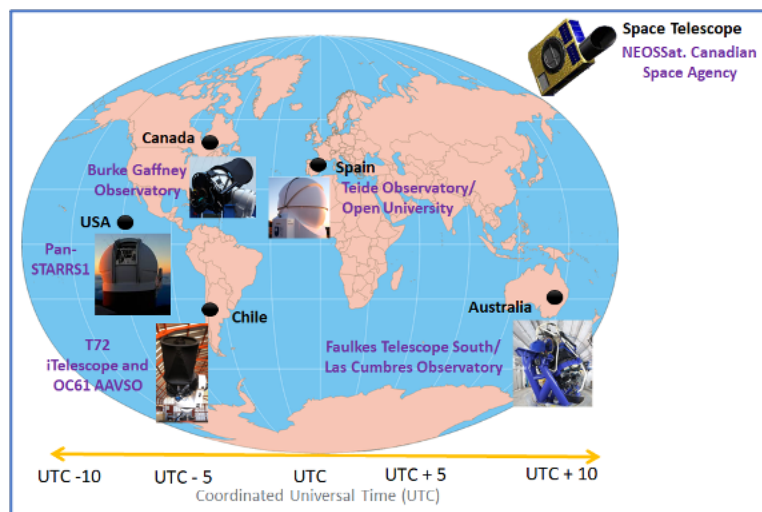


Figure 2. Robotic Telescopes Used by Me to Observe Asteroids

Observations from different longitudes provided more continuous time-series data to determine an asteroid's physical properties accurately. I also took observations from Canadian Space Agency's space telescope: Near Earth Object Surveillance Satellite NEOSat).

3.2 Collaboration with Citizen Scientists for Joint Observations and Data Sharing

As there was high demand for robotic telescopes to observe Didymos during the impact of the DART Mission, I collaborated with citizen scientist astronomers in Chile, France, and the USA. We coordinated our observation time on the telescopes to image the Didymos system at different times over multiple nights and shared the data. It allowed for extended observations of Didymos, which is useful for binary asteroids as their mutual orbital period could run from a few hours to more than a day. See Table 1 for the list of primary observations of Didymos used for analysis.

Table 1. Log of Primary Observations of Didymos System using Robotic Telescopes

Date	Telescope	Observation (hours)	Filter
2022-09-11	T30	3.8	R
2022-09-19	T72	2.3	R
2022-09-20	T72	4	R
2022-09-23	T72	1.1	R
2022-09-24	T72	2	R
2022-09-27	T30	1	R
2022-09-30	T32	3.9	R
2022-10-01	OC61 AAVSO	4	SR
2022-10-01	T72	2.8	R
2022-10-02	T72	3.2	R
2022-10-02	T30	1.2	C
2022-10-23	NEOSSat	2.2	C
2022-11-17	FTS/LCO	1.2	R
2022-11-21	FTS/LCO	1.5	R
2022-11-30	BGO	3.1	C
2022-12-02	Sugarloaf Observatory	4	C
2022-12-21	Sugarloaf Observatory	4	C
2022-12-25	Sugarloaf Observatory	4	C
2022-12-26	Sugarloaf Observatory	4	C

4. Methodology

I devised a ten-step methodology to determine the physical properties of near-earth asteroids. The methodology centred on developing photometry algorithms to analyze data from robotic telescopes and to accurately measure the periodic change in an asteroid's brightness because of its physical characteristics. The algorithms were written using Python programming language and its free libraries and used open data and school-level math.

4.1 Centroiding Known Stars and Asteroids

Data gathered from robotic telescopes contain information about the right ascension and declination of the image, field of view, binning, and pixel scale. I wrote Python routines that used this information to query the European Space Agency's GAIA DR3 and NASA/JPL's Horizons System database to find the celestial coordinates of known stars and asteroids, respectively, in the image.

The celestial coordinates were transformed to pixel coordinates to map the known stars and the asteroid onto the image. I made two assumptions to find the stars' and asteroids' centers in the

image. First, the stars are circular, and second, they are brightest in the center and become dimmer towards the edges. I used the area of the circle and the weighted mean formula to develop the centroiding algorithm. See Figure 3. Higher weight was given to the brighter pixels in the image of the stars and asteroids to allow the algorithm to find their centres quickly.

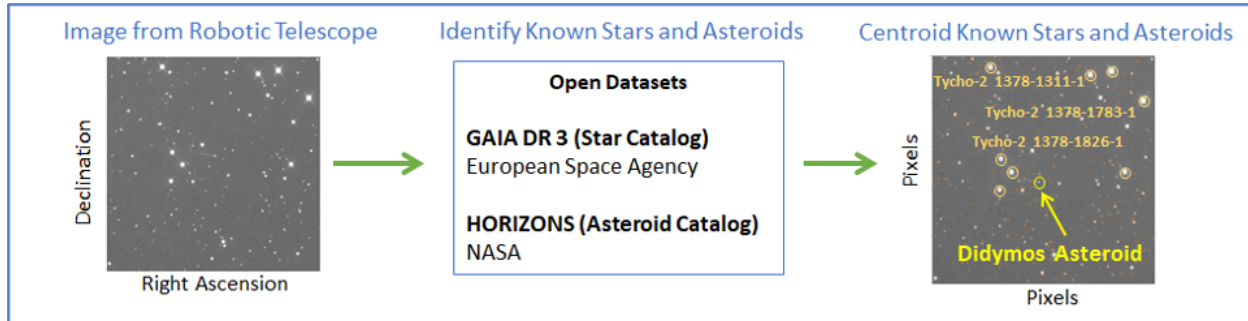


Figure 3. Mapping Celestial Coordinates of Known Stars and Asteroids to Pixel Coordinates and Centroiding Them

4.2 Determining the Optimal Aperture Size for Photometry

I created a circular aperture around the asteroid to count its total pixel brightness. The optimal aperture size had to be determined as it would be the same for all the images in an observation. If the aperture is too small, it will not measure the full brightness of the asteroid, and if it is too large, the background noise associated with reading pixel values will increase.

Citizen scientists usually have access to telescopes with smaller apertures and image asteroids during opposition (closest to Earth) when they are brighter. During this time, the pixel spread of the asteroid on the image is large and may be close to surrounding stars causing their light to be included in the asteroid's pixel brightness calculation. The algorithm undertakes slope analysis on the graph between the total pixel brightness of the asteroid and the aperture size. The aperture corresponding to the slope of 1 on the graph is the smallest optimal size. A slope of less than one means adding more pixels would increase background noise, while a slope of more than one means more pixels could be added to the aperture to measure the total brightness of the asteroid. See Figure 4. The process was repeated for all the images in the observation, and the median value was used as the optimal aperture size.

An annulus was created around the asteroid aperture to measure the average background sky brightness in the image. The contribution of sky brightness was subtracted from the total pixel brightness of the asteroid. Log formulas were applied to convert the total pixel brightness value into instrument magnitude.

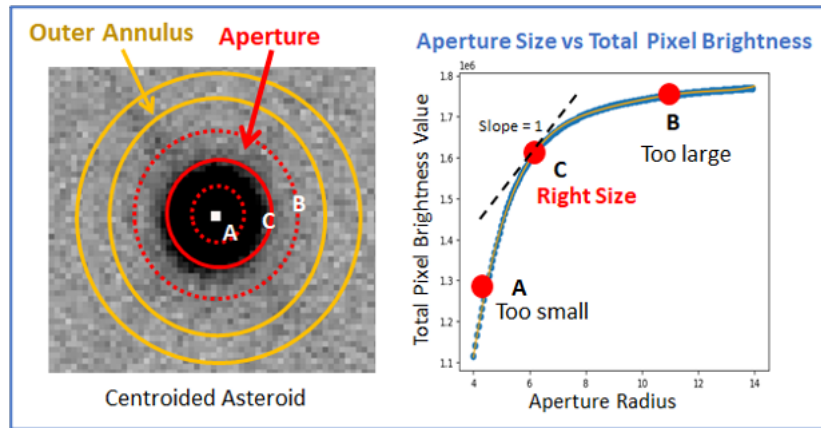


Figure 4. Determining Optimal Aperture Size for Photometry Using Slope Analysis

4.3 Finding Comparison Stars

A single photometry observation may extend over 3 hours, during which seeing conditions may change due to changes in weather and airmass, which impact the instrument magnitude of the asteroid. The algorithm selects 4 to 7 comparison stars of known and constant magnitudes in the field of view of the asteroid. The effects of changes in seeing conditions can be eliminated by quantifying changes in the instrument magnitude of these comparison stars during the observation period. These comparison stars are similar to the asteroid in size and color, and their instrument magnitude and true magnitude must maintain a linear relationship; they cannot be variable magnitude stars. The similar size ensures that the same aperture size can be used for measuring their brightness, and similar color eliminates differences in sensitivities of the telescope camera to celestial objects of different colors. See Figure 5.

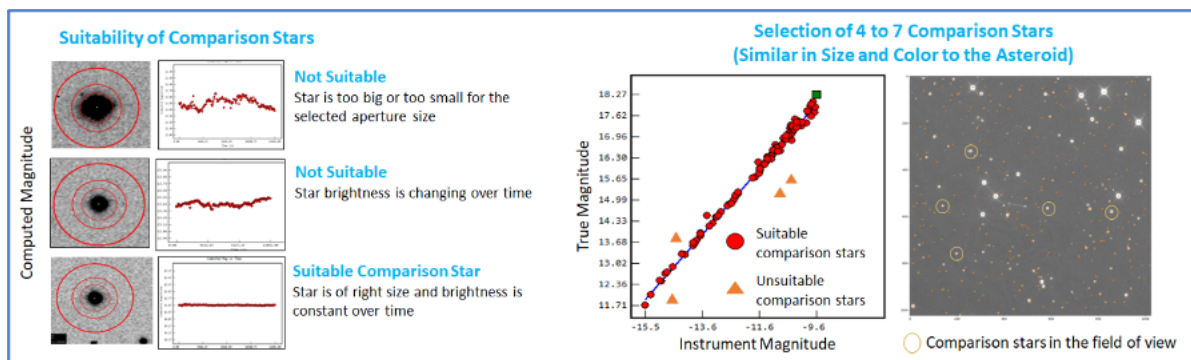


Figure 5. Criteria for the Selection of Comparison Stars

When observing asteroids during opposition, a unique challenge is presented for telescopes with a small field of view. The asteroid's proper motion (as viewed by the observer) is the highest, and the stars in the field of view change quickly, making it difficult to have fixed comparison stars for the duration of the observation. My algorithm addressed this challenge by searching and adding new comparison stars in the field of view.

4.4 Finding the Computed Magnitude of an Asteroid

The algorithm calculates the instrument magnitude of the comparison stars and queries their "true magnitude" from the GAIA DR3 star catalog. Differences in instrument magnitude and true magnitude are determined and averaged for all the comparison stars to determine changes in their magnitude because of the seeing conditions. See Figure 6.

These corrections are then applied to the asteroid's instrument magnitude, resulting in its time-series computed magnitude.

4.5 Applying Offsets to Find the Absolute Magnitude of the Asteroid

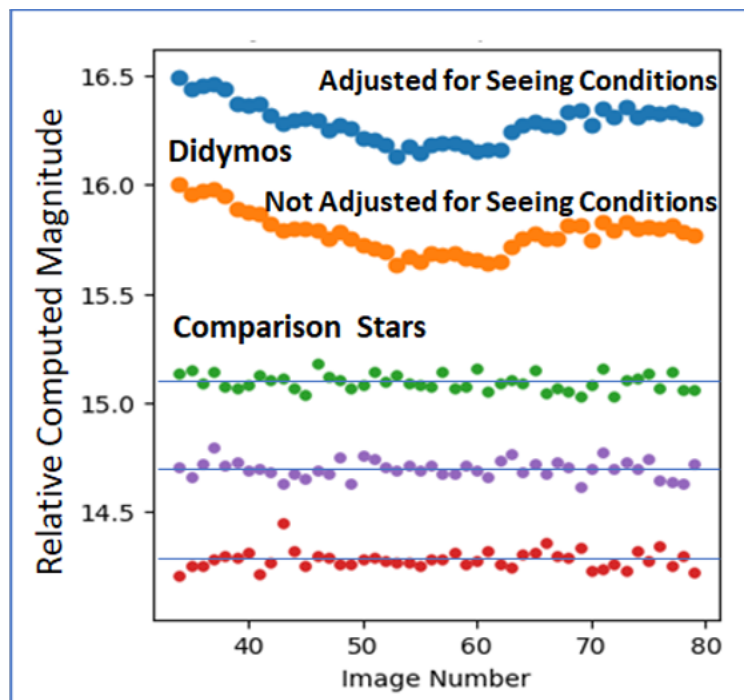


Figure 6. Eliminating the Effects of Seeing Conditions to Determine Asteroid's Computed Magnitude using Comparison Stars

Asteroids orbit the Sun, which means their heliocentric (asteroid-Sun) and geocentric (asteroid-Earth) distances and phase angles (Sun-asteroid-Earth angle) are constantly changing. These movements result in a change in the asteroid's computed magnitude and need to be eliminated. The algorithm applies offsets to standardize the asteroid's magnitude as if the asteroid were one astronomical unit from the Earth and the Sun and at a zero-phase angle. See Table 2.

Table 2. Applying Offsets to Standardize Asteroid's Magnitude at 1 Astronomical Unit from the Earth and the Sun and at a Zero-phase Angle

Observation Dates	18 Sep 2022	23 Sep 2022	18 Nov 2022
Computed Magnitude (M)	14.53	14.50	16.15
Earth-Asteroid Distance in AU (R)	0.09	0.08	0.15
Sun-Asteroid Distance in AU (r)	1.07	1.05	1.05
After Unity Offset $H(\alpha)$	19.61 (+5.08)	19.88 (+5.38)	20.16 (+4.01)
Phase Angle in Degrees (α)	41.7	49.7	59.9
Phase Offset	-1.63	-1.85	-2.15
Absolute Magnitude	17.98	18.03	18.01
Average Absolute Magnitude (H)	18.03 <i>(Based on 10 Observations)</i>		

To further improve the accuracy of the results, "light-time" corrections were applied to account for changes in time the light reflected from the asteroid takes to travel to Earth because of the asteroid's orbital motion. The algorithm time stamps each image with the time light left the asteroid rather than when it reaches the Earth. The correction allows citizen scientists to combine images taken weeks or years apart to analyze the asteroid's physical properties. Applying these offsets to the computed magnitudes of Didymos yields its time-series absolute magnitude, which can be plotted as a light curve. See Figure 7.

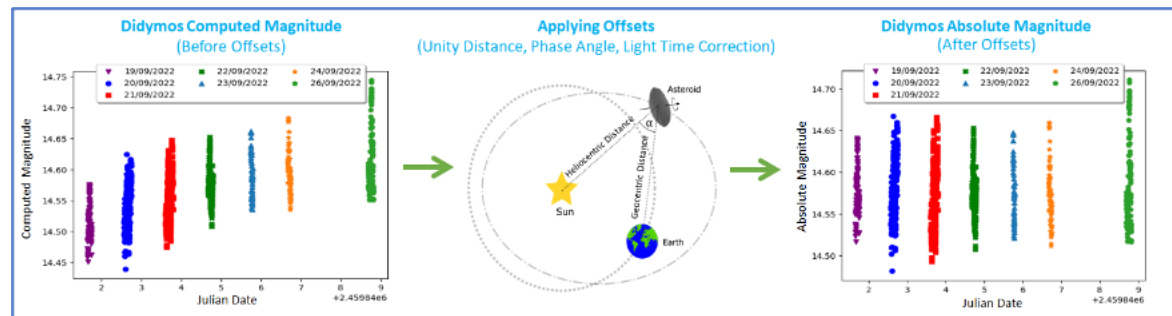


Figure 7. Applying Offsets to Eliminate Effects of the Asteroid's Orbital Motion to Determine its Time-Series Absolute Magnitude

4.6 Combining Individual Light Curves to Create Composite Light Curves

A light curve from a single observation is usually insufficient to determine an asteroid's physical properties. Light curves from multiple observations must be combined to determine asteroids' rotation and the longer orbital period in the case of binary asteroids. I used simpler school-level "modulo and congruence" math instead of complex tools such as Fourier transformations used by professional astronomers to make the algorithm easier to understand for citizen scientists and execute on their home computers.

I made a lower and upper estimate of the asteroid's rotational and orbital periodicity and divided them into thousands of intervals. The finer the intervals, the more accurate the periodicity value. After dividing the time stamps of the light curves by the periodicity value, the modulo function returned the remainder. Applying the congruent modulo made it possible to create a composite light curve of all the observations. I developed a Python function that determined the fourth-order curve fit of the composite light curve and calculated its root mean square error (RMSE). The process was repeated for each periodicity value. The correct periodicity corresponded to the composite light curve with the least RMSE.

4.7 Finding the Rotation Period of Asteroids

Most asteroids are irregular in shape as they lack sufficient gravity to make them spherical. Different sides reflect light differently as they rotate, leading to two maxima and two minima in their light curve, making it possible to determine their rotation period. See Figure 8.

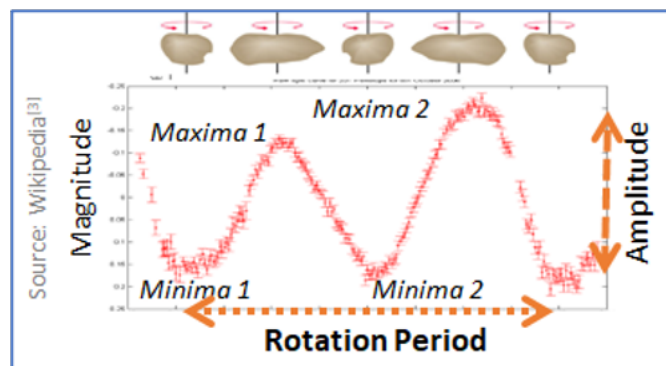


Figure 8. Asteroids' Light Curves Display 2 Minima and 2 Maxima Because of the Rotation of Asteroids

I estimated the periodicity of Didymos to be between 2 hours and 5 hours, subdivided them into 5000 intervals and combined light curves from multiple observations to create a composite curve with the least root mean square error. The periodicity of this composite light curve was the rotation period of Didymos.

4.8 Finding the Mutual Orbital Period of the Binary Asteroid

In the case of binary asteroids, light curves can yield the secondary asteroid's rotation period and mutual orbital period. Subtracting the primary asteroid rotation curve from the composite light curve generates the secondary asteroid light curve. See Figure 9.

Assuming, as with most binary asteroids, their primary and closely orbiting secondary is tidally locked, the orbital period of the secondary equals one rotation period of the secondary, simplifying the analysis.

Estimating the orbital period of Dimorphos to be between 8 hours and 16 hours, I divided them into 10 000 sub-intervals, found the fourth-order curve fit, and used the curve with the least

RMSE to determine the orbital period of the secondary. See Figure 10 for the composite light curves and Figure 11 for the RMSE Graph.

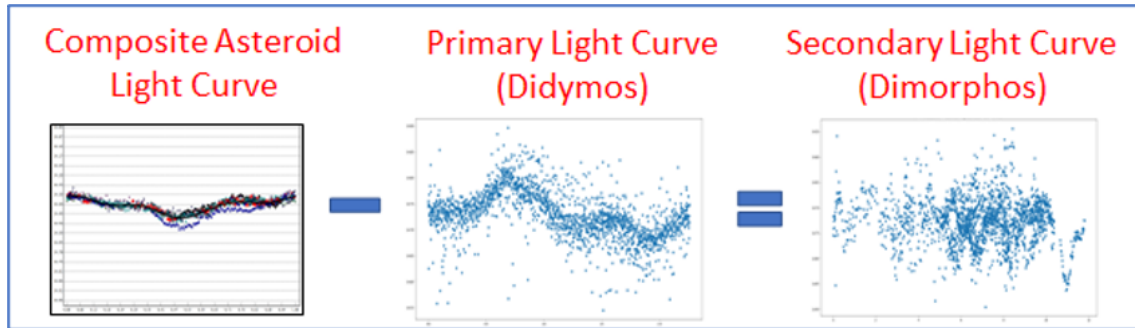


Figure 9. Determining the Secondary Light Curve of a Binary Asteroid by Subtracting the Primary Light Curve from the Composite Light Curve

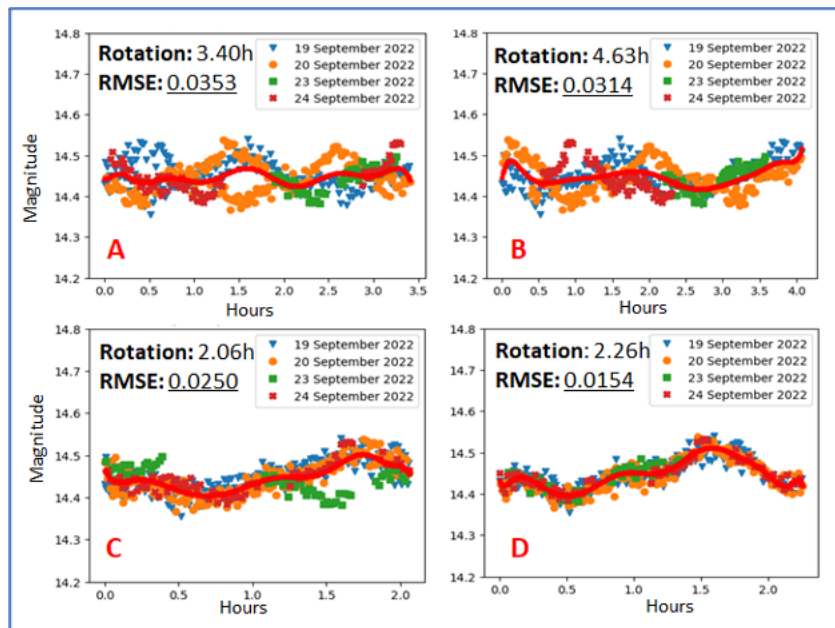


Figure 10. Combined Light Curves with Different Periodicities, in Decreasing Order of RMSEs to Determine Rotation Period of Didymos.

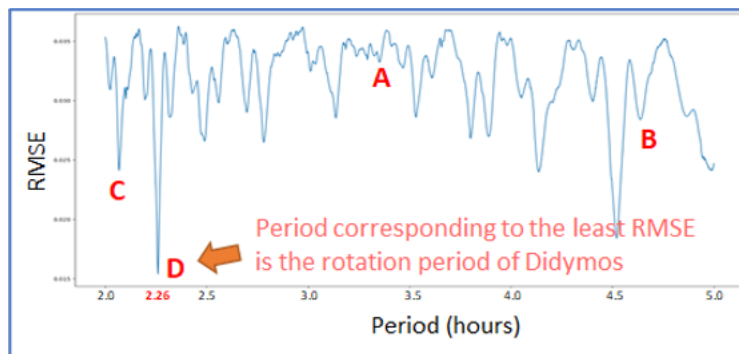


Figure 11. Graph of Root Mean Square Errors to Find the Rotation Period of Didymos

4.9 Finding Change in the Apparent Magnitude of the Asteroid after the DART Impact

The kinetic impact of the DART spacecraft on Dimorphos would change its apparent magnitude due to the sunlight reflected from the stream of ejected material. The difference in the apparent magnitude of the Didymos system was measured before and after the impact and compared with the expected magnitude of the system if there was no impact.

4.10 Measuring the Length of the Ejecta Tail of Asteroid Dimorphos After the Impact

The impact of the DART spacecraft on Dimorphos led to a stream of debris ejected away from its surface. To measure the length of the ejecta tail, I imaged the Didymos system over multiple nights immediately after the impact. See Figure 12.

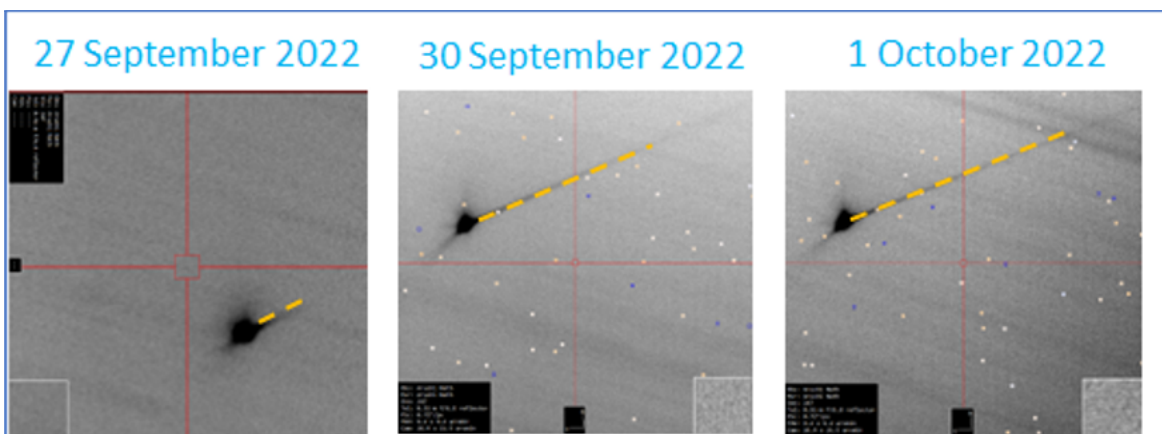


Figure 12. Measuring Pixel Length of the Ejecta Tail of Dimorphos

I measured the pixel length of the tail and used the pixel scale value (measurement of how much of the sky is covered by one pixel) of the telescope's camera to convert pixel tail length into arcminutes. Using the distance of Didymos from the Earth at the imaging time, the tail length was converted from arcminutes to kilometres.

5. Results

5.1 Algorithm Developed for Use by Citizen Scientists to Determine an Asteroid's Physical Properties

The methodology was transformed using Python functions and Numpy, Matplotlib and Astropy libraries into an algorithm for citizen scientists. The functions queried open datasets and undertook weighted mean, median, root mean square error, and slope analysis calculations. The combined algorithm found the optimal aperture size, comparison stars, offsets, and merged observations from different observers and multiple nights to accurately determine an asteroid's physical properties. The algorithm uses school-level math and is computationally inexpensive to run.

5.2 Determining Physical Properties of the Didymos Binary Asteroid System

I applied my algorithm to observations of the Didymos binary system made from multiple robotic telescopes of aperture sizes (ranging from 40 cm to 200 cm) and obtained the following results:

5.2a Absolute Magnitude and Size of Didymos

The algorithm found the absolute magnitude of Didymos to be 18.03. Using the geometric albedo value of 0.16, its diameter was determined to be 820 metres.

5.2b Rotation Period of Didymos

The rotational period of Didymos was measured to be 2.26 hours with an amplitude of 0.1 magnitude. See Figure 13. No changes were measured in the rotation period and amplitude before and after the DART impact.

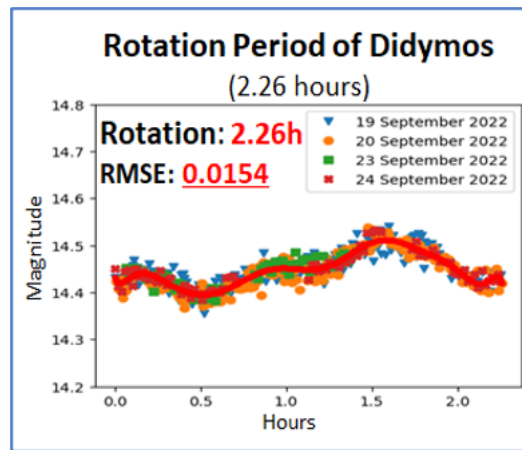


Figure 13. Rotation Period of Didymos (Did not change Post Impact)

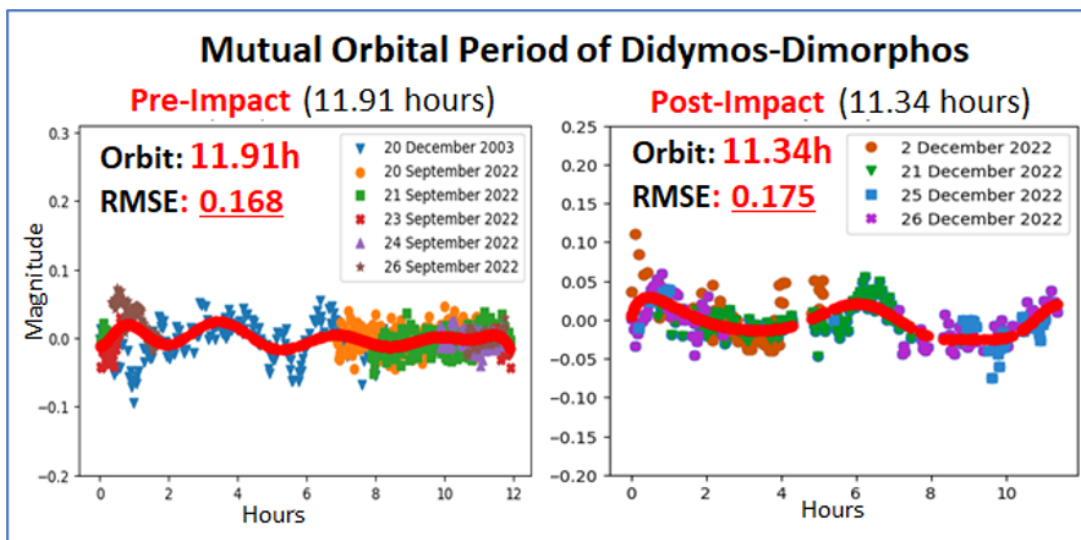


Figure 14. Determining Mutual Orbital Period of Dimorphos (Pre and Post Impact)

5.2c. Mutual Orbital Period of Dimorphos

The mutual orbital period of Dimorphos was measured to be 11h 55m before the impact. After the impact, the orbital period was reduced by 35 minutes to 11h 20m. See Figure 14.

5.2d Changes in the Apparent Magnitude of Didymos

Pre-impact, the apparent magnitude of Didymos was similar to the predicted values for those dates. Post-impact, a 1.2 magnitude change in apparent magnitude was observed. The asteroid had become brighter because of the sunlight reflected from the ejecta. The apparent magnitude took almost a month to return to its normal value. See Figure 15.

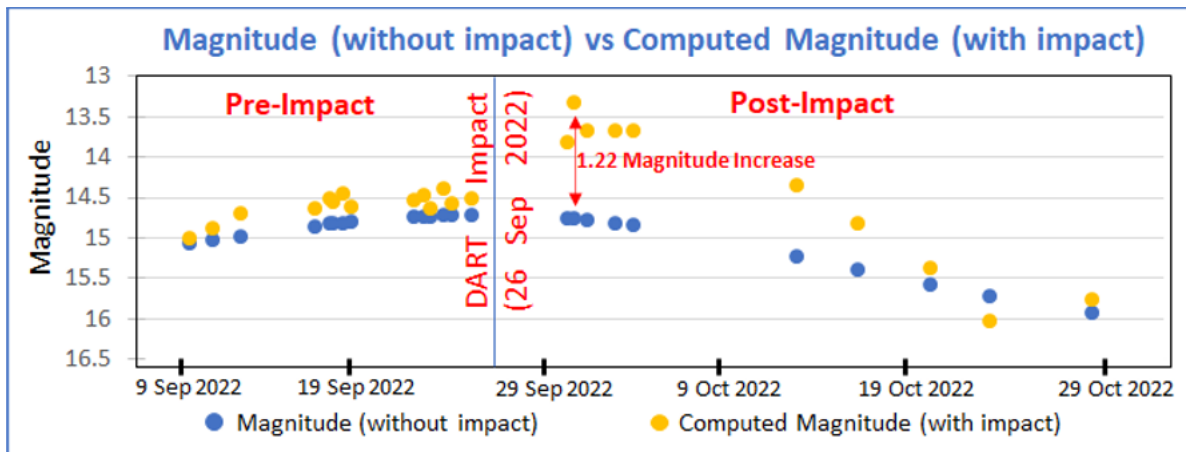


Figure 15. Increase in the Brightness of Didymos Post-Impact (26 September 2022)

5.2e Ejecta Analysis (Length of Visible Tail of Dimorphos)

The tail length of the ejecta increased every day. Five days after the impact, I measured the ejecta tail of Dimorphos from stacked images to be over 20,000 km. See Figure 16.

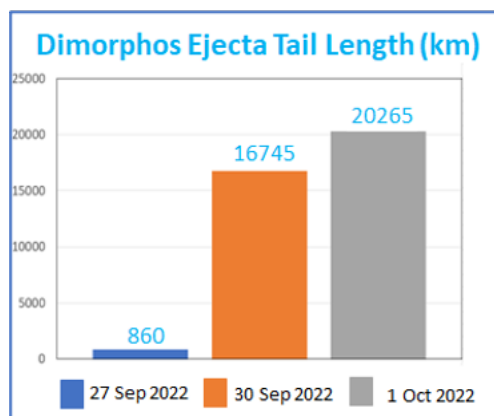


Figure 16. Increase in Ejecta Tail Length in Kilometres. Post-Impact (26 September 2022)

6. Discussion

Using the results from my algorithm, I could determine other physical properties of the asteroid.

6.1 Rotation Period and Strength of Didymos

Gravity keeps an asteroid intact. Asteroids with faster rotation periods (< 2.2 hours) are monolithic (strength-based); else, they would fly apart. Non-monolithic (rubble-based) asteroids must have a slower rotation period (> 2.2 hours). Furthermore, asteroids of sizes over 150 metres are likely to be "rubble piles" as larger asteroids are impacted by other asteroids causing them to fragment. See Figure 17.

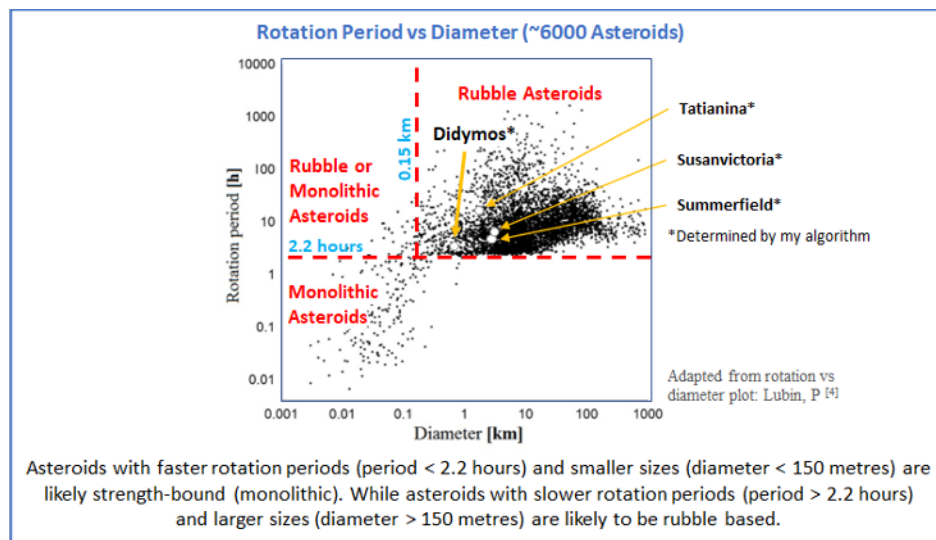


Figure 17. Determining Asteroid's Strength from its Rotation Period and Diameter

6.1a Strength of Didymos

From [Result 5.2a](#), I determined the size of Didymos to be 820 metres, and from [Result 5.2b](#), its rotation period was calculated to be 2.26 hours. As the size of the asteroid is above 150 metres and the rotation period is above 2.2 hours, Didymos is likely a rubble-based asteroid. A boulder on Didymos will not fly away in space as its rotation period is not high enough to overcome its gravity.

6.1b Strength of Dimorphos

As Didymos is a binary asteroid and Dimorphos is its moonlet, they are likely made of the same parent material. Furthermore, a 20,000 km ejecta tail obtained from [Result 5.2e](#) following a 160-metre Dimorphos strengthens the argument that Dimorphos is a rubble-based asteroid.

6.2 Change in the Orbital Path of Dimorphos

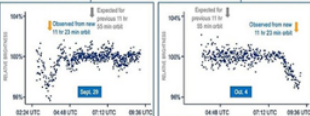

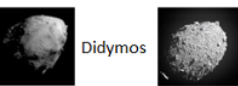
Kepler's third law states that the square of a celestial object's orbital period is directly proportional to the cube of the semimajor axis of its orbit. It implies that the period for a satellite to orbit the primary decreases rapidly as the radius of its orbit decreases.

Thus a 35-minute post-impact decrease in the orbital period of Dimorphos from [Result 5.2c](#) translates to a 40-metre decrease in its orbital radius, showing that asteroid deflection by the DART mission was successful.

6.3 Validation of the Results

The results from my algorithms matched those produced by the NASA DART Mission, and the asteroid's physical properties were correctly determined. See Table 3.

Table 3. Validation of the Results by Those Produced by NASA and Other Sources

Didymos Physical Properties		Calculated by My Algorithm	Measured by NASA	Accuracy	Validation Sources
Absolute Magnitude		18.03	18.12	99.5%	NASA Small Body Database Lookup https://ssd.jpl.nasa.gov/tools/sbdb_lookup.html/?sstr=65803
Size (metres)		820	780	95.1%	
Rotation Period and Amplitude		2.26 hours Amplitude = 0.1	2.26 hours Amplitude = 0.1	100%	
Mutual Orbital Period	Pre-Impact	11 hrs and 55 min (11.91 hrs)	11 hrs and 55 min (11.91 hrs)	100%	NASA https://www.nasa.gov/feature/nasa-dart-imagery-shows-changed-orbit-of-target
	Post-Impact	11 hrs and 20 min (11.34 hrs)	11 hrs and 23 min (11.38 hrs)	99.6%	
Post-Impact Peak Increase in Computed Magnitude		1.2 magnitude	1.2 magnitude	100%	 ATLAS Forced Photometry Server https://fallingstar-data.com/forcedphot
Asteroid Composition		Rubble Pile	Rubble Pile	100%	 Didymos Dimorphos

There was a perfect match in the rotation period, pre-impact mutual orbital period, peak brightness of the ejecta, ejecta tail length, and asteroid strength calculations. There was less than a 5% discrepancy in the size measurement of Didymos, likely due to the difference in measurement methods. My algorithm determined the asteroids' size using ground-based telescopes from the absolute magnitude and surface reflectivity of Didymos. NASA measurements were from space using the DRACO camera onboard the DART spacecraft on its close approach towards Didymos.

6.4 Applying the Algorithm to Analyze Other Near-Earth Binary Asteroids

My algorithm can combine multiple observations taken by citizen astronomers from different longitudes using different robotic telescopes. This attribute is especially useful for analyzing the physical properties of near-earth binary asteroids, as their mutual orbital period can extend over

a day and require longer time-series observations. As citizen astronomers are more numerous and distributed across the globe, they are likely to have a large amount of data that can be integrated and analyzed.

I have received requests from other professional and citizen science astronomers to apply my algorithm to new data they have gathered on binary asteroids to find their rotation and mutual orbital periods. The results of my algorithm were used to validate the results they obtained. The algorithm was successfully applied to binary asteroids (4786) Tatinina, (3378) Susanvictoria and (7344) Summerfield. See Figure 18.

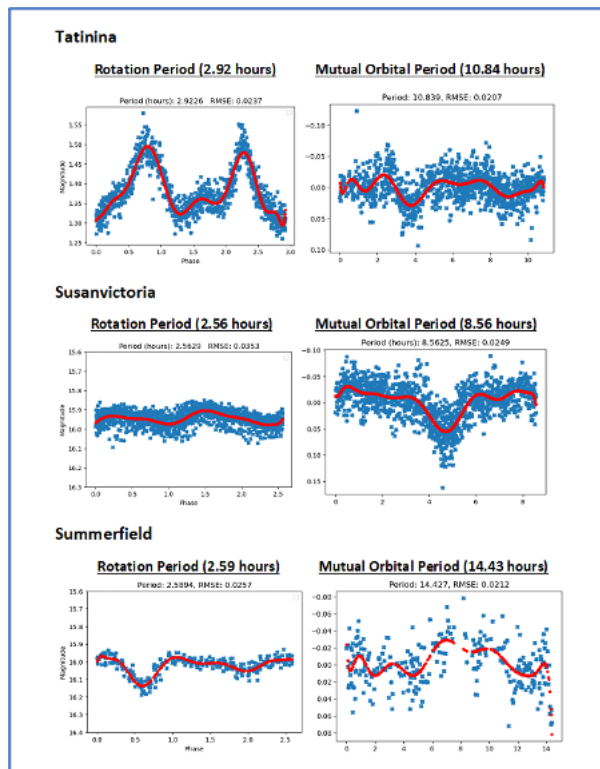


Figure 18. Applying the Algorithm on Other Binary Asteroids

6.5 Errors and Limitations

My observation plans for robotic telescopes aimed to achieve a Signal-to-Noise Ratio (SNR) greater than 100. It yielded a measurement uncertainty of less than 0.01 magnitude, which was acceptable for measuring an asteroid with an amplitude of 0.1 magnitude. The limited processing capability of my home computer restricted the precision of rotation period calculations to 2 significant digits. See Figure 19.

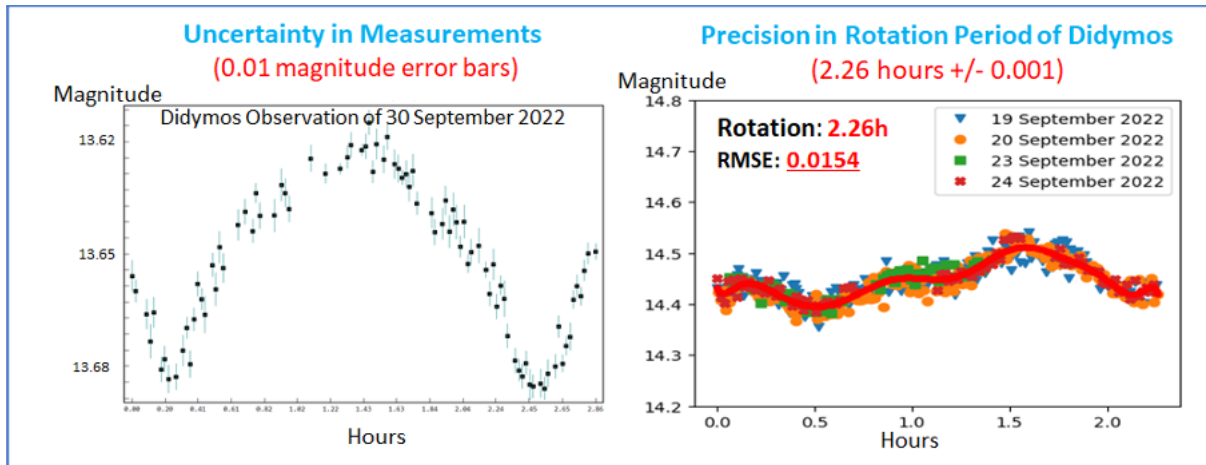


Figure 19. Uncertainty in Robotic Telescope Observations and Precision of Didymos

7. Conclusions

All the project goals were achieved. Algorithms were developed to accurately determine the physical properties of near-earth asteroids by combining images from robotic telescopes and open data. The algorithms work with smaller-aperture telescopes accessible to citizen scientists, use school-level math and can be run on home computers. When tested on a real-world scenario, the algorithms successfully determined the physical properties of the Didymos binary asteroid and confirmed the successful deflection of Dimorphos by NASA's DART mission. The results from my algorithms matched those produced by NASA. Citizen scientists can accelerate the pace of analysis of the physical properties of near-earth asteroids and become planetary defenders.

8. Open-Source Algorithm and Training Modules

I have made the methodology and algorithms open source on GitHub so that citizen scientists can use and adapt them. <https://github.com/Spacegirl123/Photometric-Observations-of-Didymos>

To encourage young citizen scientists, especially girls, to take up math, programming, and observational astronomy, I created a four-section training module on Jupyter Notebook on gathering data from robotic telescopes and analyzing it. They can use my raw time series data of the Didymos system that I made open source on the Asteroid Light Curve Data Exchange Format (ALCDEF) database.

I have given webinars about this project in partnership with the Royal Astronomical Society of Canada and iTelescope.net to excite youths to solve 'hard' problems that benefit humanity.

9. Future Applications

I will expand my algorithms to support the 2026 European Space Agency's Hera Mission to Didymos and the Chinese and Japanese Planetary Defense Test Missions to 30-metre asteroids. I

plan to integrate observations from radio telescopes to allow 3D shape modelling for additional characterization of asteroids.

Acknowledgments (Alphabetical Order)

I thank Brian D. Warner (ALCDEF), Christian Sasse and Leigh Moore (iTelescope), Cristina Tomas (NASA), Daniel Parrot (Citizen Scientist), Donald Prey (Sugarloaf Mountain Observatory), Helen Usher and Sarah Roberts (Faulkes Telescope), Jean-Claude Merlin (Citizen Scientist), Kenneth Menzies and Dirk Terrell (AAVSO), Martin Bergeron and Denis Laurin (Canadian Space Agency) and Paul Roche (Cardiff University).

References

- [1] Center for Near-Earth Object Studies. Total number of asteroids discovered monthly. Accessed May 2023. Retrieved from <https://cneos.jpl.nasa.gov/stats/totals.html>
- [2] Space.com. (2022, 8 December). China's Asteroid Impact Mission Will Send Two Spacecraft to Slam into Space Rock. Space.com. Accessed May 2023. Retrieved from <https://www.space.com/china-asteroid-impact-mission-two-spacecraft>
- [3] Wikipedia. (2022, 5 April). Light curve [Photograph]. Accessed April 2023. https://en.wikipedia.org/wiki/Light_curve
- [4] Lubin, P. Effect of asteroid rotation on directed energy deflection [Photograph]. Accessed June 2023. https://www.researchgate.net/figure/Measured-rotation-period-of-6-000-asteroids-A-distribution-of-measured-asteroid_fig1_286135399
- [5] Gault, D. Lightcurves of minor planets. British Astronomical Association. Accessed May 2023. <https://britastro.org/asteroids/dymock4.pdf>

“Long Secondary Period (LSP) Stars” and the LSP Phenomenon

John Percy, Mayank H. Shenoy, and Sandra Zhitkova

Department of Astronomy & Astrophysics and Dunlap Institute of Astronomy & Astrophysics,
University of Toronto; John.percy@utoronto.ca

Abstract

Red giant stars are unstable to radial pulsation, most commonly in the fundamental and/or first overtone mode. At least a third also have a *long secondary period* (LSP), 5 to 10 times the pulsation period. Its cause was unknown for decades but, in 2021, there was a publication with strong evidence that the LSP was due to eclipses of the red giant by a dust-enshrouded companion which was originally a planet, but accreted matter from the red giant wind and became a brown dwarf or low-mass star. Still, several questions remain, and some of these are among the motivations for the present work. One question is the nature and cause of “LSP stars” -- an unofficial class of red giant variables, introduced in the All-Sky Automated Survey for Supernovae (ASAS-SN) variable star catalog. In these, the LSP variability is dominant; it has a significantly larger amplitude than the pulsation.

In one part of the present study, we used AAVSO data and VSTAR software to analyze the variability of 102 red giants (and 10 red supergiants) in the AAVSO Binocular Observing Program (ABOP), including pulsation and LSP periods and amplitudes. At least 24 stars pulsated in two or more modes, and at least 58 had LSPs. In the other part of this study, we determined the periods and amplitudes of a sample of 35 of the 185 LSP stars in the ASAS-SN catalog, using ASAS-SN data, and VSTAR. These stars have short pulsation periods and small pulsation amplitudes, typical of a *low-luminosity* red giant. But such stars would not be expected to have strong winds, so how were they able to accrete enough matter to convert a planet into a brown dwarf or low-mass star? We note that several stars in the ABOP are LSP stars in the sense that their catalog period is actually their LSP, not their pulsation period.

We present an overview of our results, and their limitations, and mention several questions still remaining. Some of these questions involve the amplitudes of pulsation and LSP, which have not been determined and/or extensively discussed in previous studies. AAVSO observations can continue to help.

1. Introduction

Note: This is a brief summary of our two interrelated projects; two detailed papers have now been published in *JAASO* (Percy and Zhitkova 2023; Percy and Shenoy 2023).

Red giants are unstable to pulsation, in the fundamental, first overtone, or second overtone mode, or a mixture of these. The larger and more luminous the star, the longer the period and the larger the amplitude.

About a third of red giants also show a long secondary period (LSP), 5 to 10 times the pulsation period. These LSPs were studied extensively a century ago through photographic photometry, especially at the Harvard College Observatory. AAVSO observations have also provided important information about LSPs for up to a century (Percy and Deibert 2016), but their cause remained a mystery.

The 1990's brought several massive automated photometric surveys (ASAS, MACHO, OGLE) and a new interest in the LSP phenomenon. Wood's (2000) paper, based on MACHO observations of red giants in the Large Magellanic Cloud (LMC), showed period-luminosity relations for second-overtone, first-overtone and fundamental-mode pulsation periods, and for LSPs.

Soszyński et al. (2021) provided a plausible explanation for LSPs: "The LSP light changes are due to the presence of a dusty cloud orbiting the red giant, together with a companion, and obscuring the star once per orbit ... In this scenario, the low-mass companion is a former planet that has accreted a significant amount of mass from the envelope of the host star and grown into a brown dwarf."

Interesting questions remain. Will the sun have a dusty companion when it becomes a red giant? If LSPs are so common, why had red giants not been found in such configurations, decades ago? LSPs are found in red giants in the Magellanic Clouds, and in globular clusters; can the necessary planets and dust for the LSP mechanism be produced in these low-metallicity systems? Why is there a period-luminosity relation for LSPs? The luminosity depends on the star radius; the LSP depends on the companion's orbit radius. How are these related? And, finally, how can "LSP stars" be explained?

2. Project 1: LSP Stars

"LSP stars" is a new (but not official) class of red giant variable stars, introduced in the All-Sky Automated Survey for Supernovae (ASAS-SN) variable star catalog (asas-sn.osu.edu/variables). They are red giant variables in which the LSP variability dominates the pulsational variability. The ASAS-SN catalog lists the dominant period only, which is therefore the LSP in these stars.

The puzzling thing about the LSP stars is the following: their short pulsation periods and small pulsation amplitudes indicate that they are small, low-luminosity stars; in that case, their winds should be rather weak; so how can their companion accrete enough gas and dust to produce a sizable LSP amplitude?

In this project, we used ASAS-SN data and the AAVSO VSTAR time-series analysis package to determine LSP and pulsation periods and amplitudes in a moderate random sample of 35 of the 185 LSP stars in the ASAS-SN catalog. *Note that VSTAR determines semi-amplitudes in Fourier*

analysis; we refer to them as amplitudes from now on. By definition, the properties of this sample of stars are biased in the sense that they will have larger LSP amplitudes and smaller pulsation amplitudes. Also: the ASAS-SN database is only about 1500 days long, so it is difficult to identify and measure accurate LSPs, which are several hundred days long.

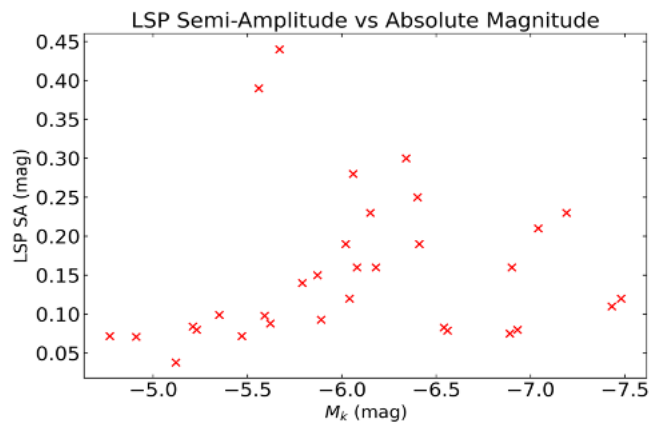


Figure 1. The LSP amplitude as a function of luminosity for LSP stars in the ASAS-SN catalog. There is a weak tendency for the amplitude to be lower in low- and high-luminosity stars.

As expected, the pulsation period increases with increasing luminosity or size of the star, though with some scatter because the stars may be pulsating in different low-order modes. Likewise, the pulsation amplitudes increase with increasing luminosity or size. The more interesting result is the relation between the LSP amplitude and the luminosity or size (Figure 1). The LSP amplitude is a measure of the extent of the eclipse of the star by its dust-enshrouded companion. It appears to be smaller in low- and high-luminosity stars, and larger in moderate-luminosity ones.

2.1 Project 1A: LSPs in Mira Stars

The largest, most luminous red giants are Mira stars. Do they have LSPs? We used long-term AAVSO data, and VSTAR to look for LSPs in a random sample of 27 Mira stars. The light curves and Fourier spectra are dominated by the large-amplitude pulsation so, in most cases, we found only upper limits – set by the noise level -- for the amplitudes. They were: $8 < 0.10$, $1 < 0.12$, $7 < 0.15$, $5 < 0.20$, $1 < 0.25$. Only four stars seemed to have LSPs – with amplitude of about 0.20 -- but Mira itself may have an amplitude of 0.53. This definitely deserves further study. But the values and upper limits that we have found are consistent with the conclusion, shown in Figure 1, that larger, more luminous stars have smaller LSP amplitudes.

3. Project 2: Red Giants in the AAVSO Binocular Observation Program

In order to put the Project 1 results into more context, and to investigate the LSP amplitudes in more detail, we undertook a second project: to determine pulsation periods, LSPs, and their amplitudes for the red giants (and a few red supergiants) in the AAVSO Binocular Observation Program. There are 137 such stars in this program; 110 yielded results. Note that this is also a biased sample, depending on the way that stars were chosen for this program: presumably bright

enough, and with a sufficient amplitude to be studied with visual observations through binoculars.

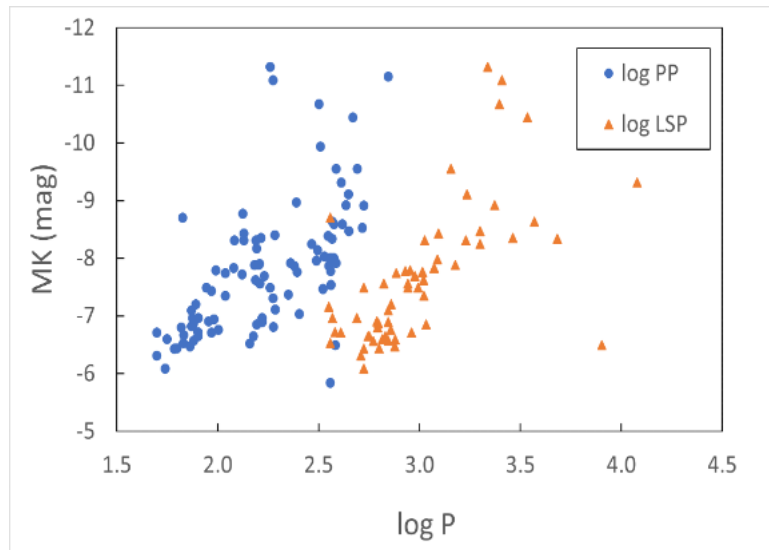


Figure 2. Period-luminosity relations for red giants in the AAVSO Binocular Observing Program. The sequences are, from left to right, first overtone and fundamental pulsation periods, and LSPs.

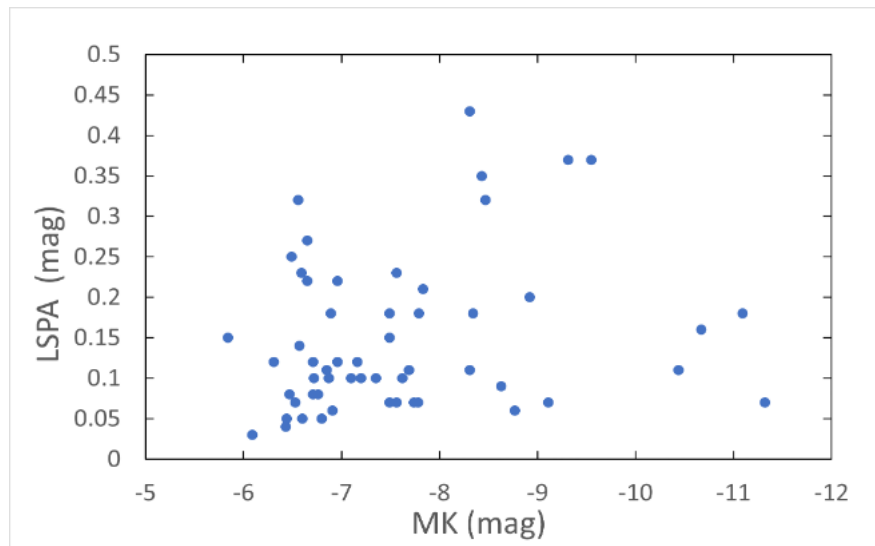


Figure 3. LSP amplitude as a function of luminosity for stars in the AAVSO Binocular Observing Program. As in Figure 1, there is a weak tendency for the LSP amplitude to be smaller in low- and high-luminosity stars.

Figure 2 shows the period-luminosity relations for the stars. From the left, the sequences represent first-overtone and fundamental-mode pulsation periods, and LSPs. The spacings between the sequences depend on the period ratios: approximately 0.5 for first overtone to fundamental, and either 4-5 or 9-10 for LSP to pulsation period, depending on whether the pulsation period is fundamental or first overtone. At least 58 of the stars had an LSP. At least 24

were bimodal: they pulsate in both the fundamental and first-overtone mode. The ratio of these two periods decreases slightly with increasing luminosity, in agreement with previous results, and pulsation models. As with the LSP stars, the pulsation periods and amplitudes of these stars increased with luminosity. And as with the LSP stars, the interesting result was the relation between LSP amplitude and the luminosity or size of the star (Figure 3): the LSP amplitude seems to be smaller in low- and high-luminosity stars, and larger in medium-luminosity ones.

Derekas *et al.* (2006) have measured LSP amplitudes in a much larger sample of red giants and found the same pattern. In those authors' opinion, however, their results “argue for pulsation rather than binarity as the cause of the LSP phenomenon”.

It seems reasonable that the LSP amplitude, being the extent of the eclipse of the star by the dust-enshrouded companion, might be smaller in large stars, in which the companion covers a smaller fraction of the large stellar disc. It is less clear why the extent of the eclipse would be smaller in smaller stars. Perhaps, in these stars, the companion has not had the opportunity to accrete matter from their weak winds. Note that the extent of the eclipse will also depend on the orientation of the companion's orbit; it may be a central eclipse if the orbit is exactly edge-on, or partial if the companion passes mostly above or below the stellar disc.

A warning: some of the catalog periods for the red giants in the Binocular Observation Program are actually LSPs, not pulsation periods as in the vast majority of the stars. Examples are: RW Boo, BM Eri, PV Peg, CI Phe, RY UMa, VW UMa, and GO Vel.

4. Future Directions

There are several possible projects which could further increase our understanding of the LSP stars and the LSP phenomenon:

- In general: detailed study of the LSP amplitudes in a much larger sample of stars
- Use of the long AAVSO database to confirm that the LSP is constant in time, as it should be if it is a binary period
- Study and modeling of the LSP phase curve to understand more about the geometry of the eclipse
- Use of the long AAVSO database to study long-term changes, if any, in the LSP amplitude and phase curve, i.e., in the amount and distribution of dust around the companion
- Comparison of photometric measurements of the eclipse with concurrent radial velocity observations – either new or archival – to confirm the binary/eclipse mechanism.
- Modelling of the accretion and kinematics of the dusty envelope around the companion

5. Conclusion

We have derived new information about the LSP stars and LSP phenomenon, using both AAVSO and ASAS-SN data. Many mysteries remain, including how small, low-luminosity LSP stars can

accrete enough gas and dust to produce the dust-enshrouded companion needed for the LSP phenomenon according to the Soszyński *et al.* (2021) mechanism.

Acknowledgements

We thank the AAVSO observers and staff, and the compilers of the ASAS-SN database and catalog for providing the data on which this study is based. Authors Shenoy and Zhitkova are astronomy majors at the University of Toronto, supported by the highly selective U of T Work-Study Program, and the Dunlap Institute. The Dunlap Institute is funded through an endowment created by the David Dunlap Family and the University of Toronto.

References

- Derekas, A. *et al.* 2006, *Astrophys. J.*, **650**, L55.
Percy, J.R. and Diebert, E. 2016, *J. Amer. Assoc. Var. Star Obs.*, **44**, 2.
Percy, J.R. and Shenoy, M.H. 2023, <https://app.aavso.org/jaavso/article/3918/>
Percy, J.R. and Zhitkova, S. 2023, <https://app.aavso.org/jaavso/article/3906/>
Soszyński, I. *et al.* 2021, *Astrophys. J. Lett.*, **911**, L22.
Wood, P.R. 2000, *Publ. Astron. Soc. Australia*, **17**, 18.

Variable Stars in the Cepheus Flare Region

Michael Poxon

AAVSO, 185 Alewife Brook Parkway, Suite 410, Cambridge, MA 02138, USA;
mikethestarman@gmail.com

Subject Keywords

Stellar kinematics; young stellar objects

Abstract

Young variable stars in the Cepheus Flare region are discussed, together with current and recent star formation (SF) in the area, with a view to encourage observers to monitor these, and associated, objects.

1. Introduction

The Cepheus Flare is a spur of the main galactic equator that contains a mélange of phenomena associated with ongoing star formation, such as runaway stars, nebulae of various kinds, molecular clouds and accompanying filamentary structures, evidence of past supernovae, recently formed collections of massive stars - and of course young variable stars.

The designation comes from Hubble, who noticed that there were 'zones of avoidance' for the external galaxies in which he was primarily interested. In his introduction to his 1934 paper, he says (by 'nebulae' he earlier says the term refers to extragalactic objects, i.e., galaxies):

"In general no nebulae are found along the Milky Way. The zone of avoidance, representing local obscuration, is irregular and follows the general pattern of the known obscuring clouds. It is bordered by partial obscuration, which fades away into the regions of normal distribution..."

and later he makes specific mention of the Cepheus Flare, having previously mentioned similar regions in Taurus and Ophiuchus:

"The Cepheus flare, north of the galactic plane and between longitudes 60° and 100°, is perhaps less familiar, although camera plates indicate that the entire region is affected by considerable obscuration. The flare extends out to latitude 20° or more, and the partial obscuration along its borders includes the position of the celestial pole [at galactic latitude 28°]."

These quotations are from Hubble (1934).

2. Phenomena of the Cepheus Flare

2.1 Structure

The Flare region is an extremely complex and dynamic 3-dimensional region of the Galaxy and can be seen to broadly consist of:

- Expanding regions of dense parts of the Interstellar Medium (ISM) which is the raw material from which stars are born
- Dark filaments with dense cores. These cores are embryonic stars and/or star systems
- Shells suggesting multiple ancient Supernovae
- Runaway stars, i.e., those with abnormally high proper motions, suggesting eviction from theatres of expulsion such as supernovae and star formation processes

Regions between the flare and the Galactic Equator are rich in OB associations. These are now-dispersed collections of hot massive stars which however had a common area of birth in regions of types (a) to (c) above and which may have been responsible for examples of type (d). Because these stars never have long lives and are still hot and massive, they are, by these criteria, young stars; although not, as it were, 'YSO-young'; neither are they necessarily variable.

2.2 Objects

Figure 1 shows the constellation of Cepheus with various SF-associated phenomena marked. These include type (a) effects where the expanding flare material collides with existing ISM objects such as the so-called *Cepheus Bubble*.

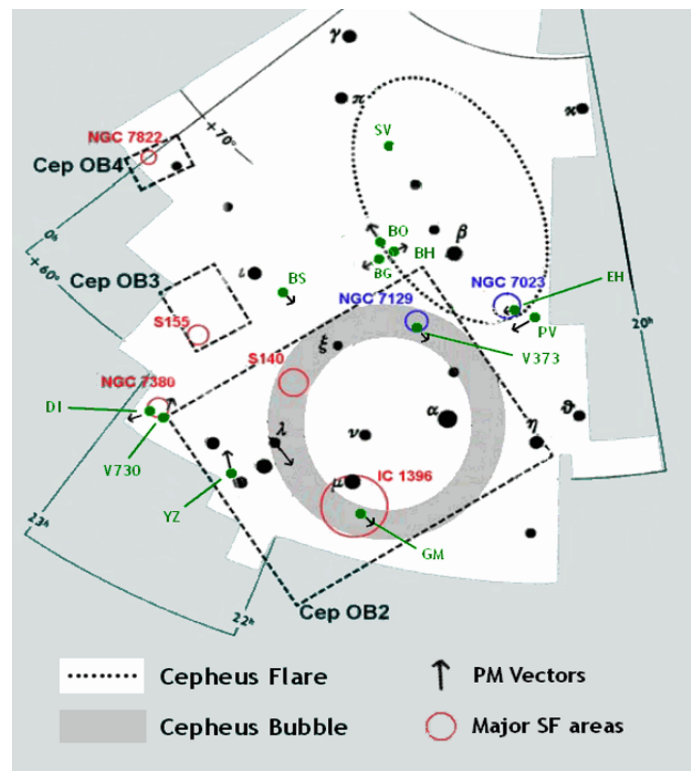


Figure 1. Star Formation phenomena associated with the Cepheus Flare region

Many of these are highly dynamic areas, such as IC 1396, Sharpless 140 and NGC 7380. Note how the major SF regions lie at the edges of both the flare and the bubble, suggesting violent bow-shock or collision processes are at work.

Several young variable stars in the AAVSO YSO programme are marked, together with their proper motion vectors. Most of these variables are intermediate-mass stars of spectral types A to G. Note that many of these stars are moving away from, or are involved with, the dynamic areas shown in Figure 1. The trio of BG, BH and BO Cep appear to be diverging from what may be a recent theatre of creation.

Table 1 shows the proper motions and distances of young stars in Figure 1. Parallaxes and PMs are all in mas/yr. PMa and PMd are colour-coded for direction of vector, and parallaxes are from Gaia DR2. The final column is simply a unitless index that serves to eliminate high values affected by proximity: thus YZ Cep has a high PM because it is closer to us, thus its V index is more or less in line with the rest (average value = 2.924) from which it can be seen that the O-type star I Cep has a far higher V value because of its genuinely high PM, which makes it a runaway star.

Table 1. Proper motions and distances of young stars in Figure 1

Star	Parallax	PMa	PMd	abs PM	V
BO Cep	2.670	5.044	3.279	6.016	2.253
BG Cep	1.627	2.287	-1.130	2.551	1.567
BH Cep	2.984	9.651	-1.604	9.783	3.278
BS Cep	1.111	-0.863	-2.280	2.438	2.194
CC Cep	1.889	-1.364	-1.360	1.926	1.020
DI Cep	2.297	4.809	-0.216	4.814	2.096
EH Cep	3.044	7.269	-2.330	7.633	2.508
GM Cep	1.213	-2.759	-4.449	5.235	4.317
PV Cep	2.910	8.228	-1.976	8.462	2.908
SV Cep	2.904	5.207	1.572	5.439	1.873
YZ Cep	4.265	0.523	13.524	13.534	3.173
V373 Cep	1.081	-1.537	-3.243	3.589	3.320
V730 Cep	2.079	4.72	-1.054	4.836	2.326
Iam Cep	1.650	-7.48	-11.090	13.377	8.107

In Figure 2 it can be more readily seen how SF processes are not simply relics of past events but are also happening currently, since many marked regions include currently variable stars such as GM Cep in IC1396. This IRAS view of the Cepheus bubble shows it as an actual 'visible' object along with the various phenomena already discussed. So the vacant centre was probably caused more recently by energetic stellar winds from the O9 star HD 207198 near the centre, among the Cep OB2a stellar association. The image demonstrates how all the major SF regions are located on the bubble's periphery. Their similar distances (about 800 pc) along the expanding bubble indicates a common instigator as a violent SN event in Cep OB2a, whose other supergiant members are shown in pink. The pink triple in IC1396 is the 'Northern Trapezium' Trumpler 37 system, consisting chiefly of the O-type triple HD206267 which in fact illuminates the entire nebula.

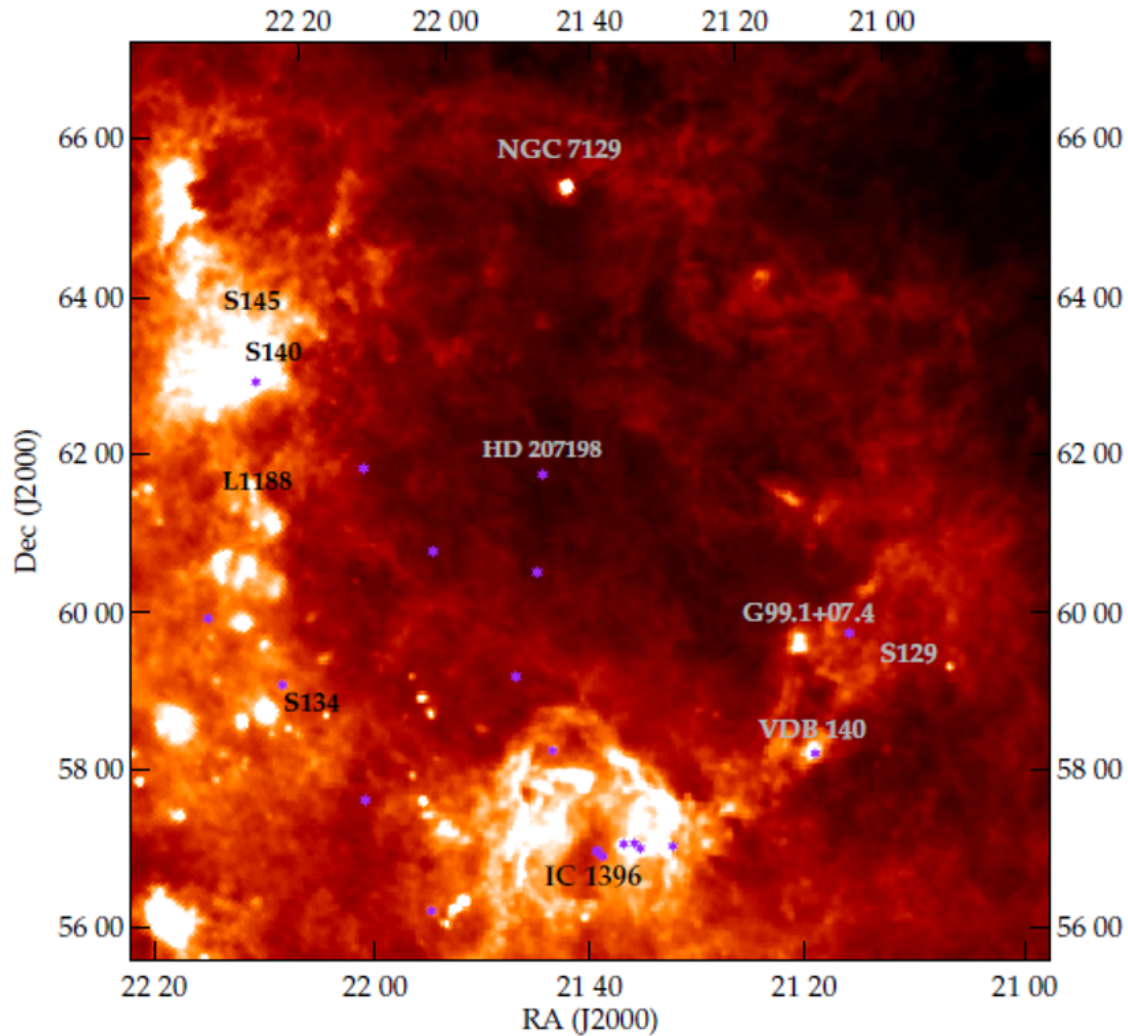


Figure 2. IRAS Image of the Cepheus Bubble

3. Example Variable Star: V730 Cephei

In the meeting presentation I showed the light curves of some of the stars in Figure 1, but here I would like to concentrate on just one of these in view of its very recent behaviour, typically varying between magnitudes 13 and 15 with a semi-regular period of about 13 days. I have observed this object since before its official variable star christening (it was previously named as MIS V1147) including two of its faintest brief minima at 15.7 and 16.1 visual. However, since about April 2023 it has been consistently below magnitude 15 – and often below magnitude 16 – for several months on end; a period from which it has only very recently emerged.

Recent studies such as that by Potravnov et al. (2017) overturn the previous classification of this object as an early-spectrum Herbig type (higher-mass) *HaeBe* star and establish its identity as a broadly solar-mass T Tauri object in view of its spectrum as deduced from their study together with its amended distance derived from Gaia, which turned out to be much less than previously thought – hence the lower luminosity and thus temperature and mass along with it.

Recently we have seen several examples of T Tauri stars behaving contrary to their previously 'normal' gradual and reasonably low-amplitude patterns of variation, such as SU Aur in 2018. The above fading event of V730 Cep merely outlines the importance of following all Young Stellar Objects in as many filters as possible, including of course observing them visually! The lightcurve (R band = red, visual = open circles) presented at the meeting shows the various phases associated with the star's recent behaviour. The outstanding event is what I call the 'Red Surge' in which the deep fade in visual is accompanied by a major brightening in longer wavelengths, which strongly indicates veiling of the star's photosphere by (probably) the circumstellar disc or a constituent of it. This effect was also observed to a slightly lesser extent by the 2018 event on SU Aurigae mentioned above. An event more similar to the V730 Cep episode is observed in the star AA Tauri, which underwent a fade from its maximum of 12.2 in 2011 and remains there now, varying between magnitudes 14 and 16.5 – in other words, virtually the same as V730 Cep. In this case the fade was caused by a warp in the circumstellar disc. Therefore, we may be seeing the same thing happening here.

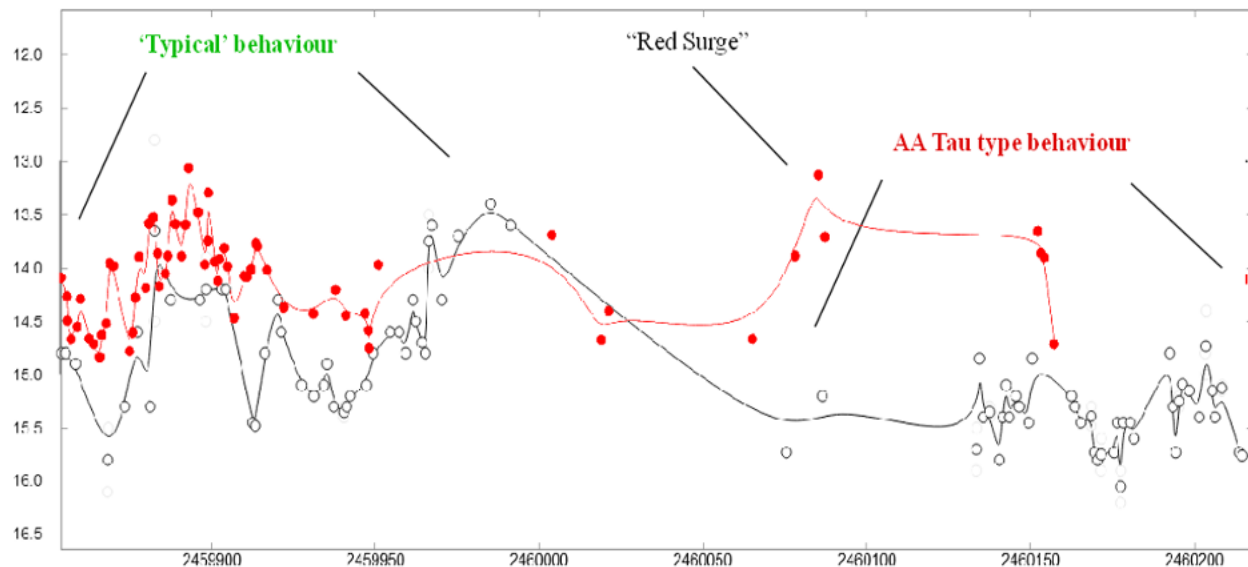


Figure 3. AAVSO lightcurve of V730 Cephei. Note the strong correlation between the times of brightening in R and the fade in Visual.

4. Conclusion

Dynamic past and ongoing activity of all kinds in the Cepheus Flare region shows this to be a part of the sky that AAVSO observers would do well to follow.

Acknowledgments

A huge dept of gratitude is owed to prof. Bo Reipurth, formerly of the University of Hawai'i. His helpful suggestions and unbounded knowledge in the field of YSO studies has proved invaluable in the creation of this article. Figures 1 and 2 are adapted from parts of a large pdf file he sent me

2 or 3 years ago when he heard I was interested in this region.

References

Hubble, E. 1934, ApJ, 79, 8

Potravnov, I., *et al.* 2017, ASP Conference Series, Vol. 508, p. 335

Imaging Stars with the CHARA Array

Gail H. Schaefer

CHARA Array of Georgia State University, Mount Wilson Observatory, Mount Wilson, CA,
91023; gschaefer@gsu.edu

Subject Keywords

Long baseline interferometry; Fundamental parameters of stars; Binary stars; Circumstellar disks; Novae; Supergiant stars

Abstract

The CHARA Array combines the light of six 1-meter telescopes at optical and near infrared wavelengths to achieve an angular resolution equivalent to a 300-meter telescope. The Array is located at Mount Wilson Observatory in southern California and operated by the Center for High Angular Resolution Astronomy (CHARA) at Georgia State University. With milli-arcsecond resolution, the CHARA Array can measure the sizes of stars, image stellar surfaces, map the orbits of close binary companions, resolve the inner structure of circumstellar disks, and peer into the early structure of novae explosions. This paper provides an overview of the CHARA Array, highlights recent science results, and discusses new opportunities for AAVSO members to collaborate with CHARA observers on targets of interest.

1. Introduction

The spatial resolution of a telescope is determined by the size of the mirror and the wavelength of light; the larger the aperture, the higher the spatial resolution. A stellar interferometer combines the light from multiple telescopes to achieve higher spatial resolution than a single telescope (Monnier et al. 2003). For an interferometer, the resolution is given by the separation between the telescopes and the wavelength of light.

The CHARA Array is a long baseline optical and near infrared interferometer located at Mount Wilson Observatory in Southern California and operated by Georgia State University (see Fig. 1). The Array combines the light of six 1-meter telescopes with baselines ranging from 34 to 331 meters (ten Brummelaar et al. 2005) to achieve sub-milliarcsecond resolution. The light from each telescope is transported across the mountain through vacuum pipes to a central beam synthesis facility. Inside the laboratory, the path length of each beam is equalized using delay line carts that track the motion of the star across the sky and correct for the geometric delay between the telescopes. The light is then sent to one of several instruments that combines the light together and records the interference fringes. Each telescope is equipped with an adaptive optics system to correct for fast atmospheric distortions and provide a stable beam of light to the science instruments. There is a second adaptive optics system in the laboratory for each

telescope line that corrects for slow distortions encountered between the telescope and the laboratory.

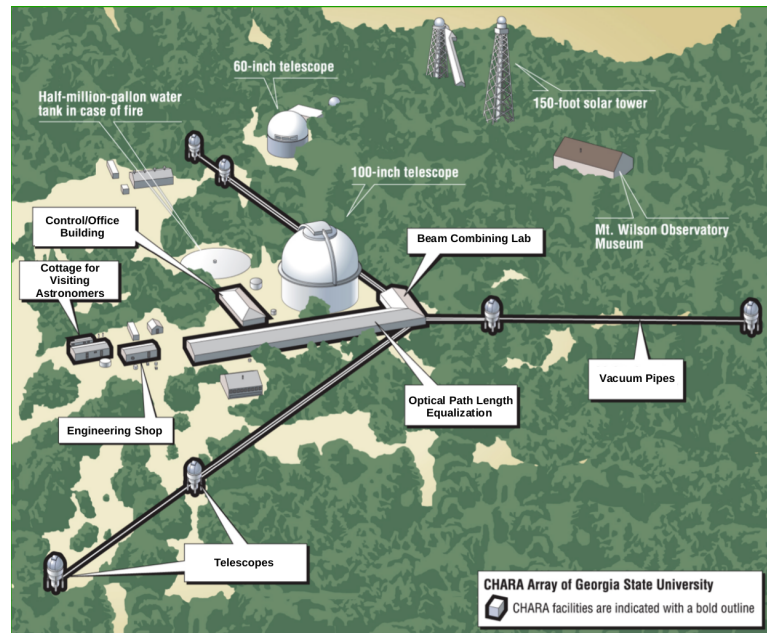


Figure 1. Layout of the CHARA Array at Mount Wilson Observatory. The light from the six CHARA telescopes is transported through vacuum pipes to the central beam combining lab. The location of the historic 60-inch and 100-inch Telescopes, as well as the Solar Towers, are shown in the schematic.

2. Science at High Spatial Resolution

The interference fringes are encoded with information about the size, shape, and brightness distribution on the surface of a star (Lawson 2000). An unresolved star will have strong, high contrast fringes, while the fringe pattern from a resolved star will be blurred out with lower contrast fringes. By measuring the visibility or contrast of the interference fringes, we can determine the size of the star. Multiple telescopes that are combined at the same time allow us to reconstruct images of the stellar surface and their circumstellar environments.

The CHARA Array can measure the angular diameter of stars all along the main sequence, from massive O-type stars to low mass M-type stars (von Braun & Boyajian 2017). The sizes of stars can be measured at different evolutionary stages as they evolve off the main sequence into the giant branch (Baines et al. 2010). Pulsating stars like Cepheid variables show cyclical changes in angular size (Merand et al. 2015). The stellar diameters measured with interferometry can be used to test models of stellar evolution, develop color-temperature relations to characterize stars that are too distant to be resolved, and estimate ages of stars based on their sizes compared with evolutionary models. The radii of exoplanet host stars can be used to refine the extent of the habitable zone around the star and characterize the properties of transiting exoplanets.

For stars that are large enough in angular size, the CHARA Array can reconstruct detailed stellar images revealing features on the stellar surfaces. Images of the magnetically active star zeta Andromedae show a persistent polar spot and lower latitude spots that change over time (Fig. 2 top left; Roettenbacher et al. 2016). Images of convection patterns on the supergiant AZ Cygnus show a complex surface with small bright features that vary on timescales of less than one year and larger features that persist for more than one year (Fig. 2 top right; Norris et al. 2021).

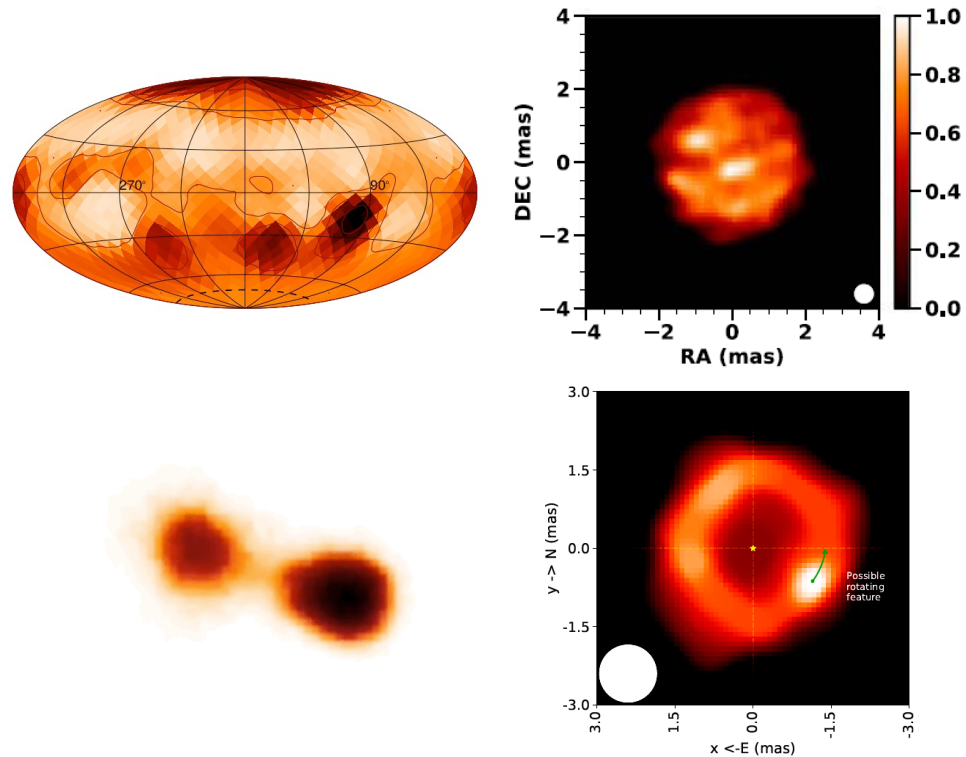


Figure 2. Examples of interferometric images from the CHARA Array. Top left: Starspots on the surface of the magnetically active star zeta Andromedae (Roettenbacher et al. 2016). Top right: Convection cells on the surface of the supergiant AZ Cygnus (Norris et al. 2021). Bottom left: Interacting binary beta Lyrae showing the tidal distortion of the mass donor and an elongated accretion disk around the mass gainer (Zhao et al. 2008). Bottom right: Circumstellar disk around the young star V1295 Aquilae showing a ring-like structure with a central cavity and a bright spot that appears to rotate around the disk over time (Ibrahim et al. 2023).

The CHARA Array is sensitive to detecting close binary companions with angular separations as small as 0.5 milli-arcseconds. Mapping the orbits of spatially resolved binary stars provides a way to measure precise dynamical masses of stars when combined with spectroscopic radial velocity measurements (Lester et al. 2022). Figure 2 (bottom left) shows a snapshot of the interacting binary beta Lyrae with an orbital period of 12.9 days (Zhao et al. 2008). In addition to mapping the orbital motion, the CHARA images reveal the tidal distortion of the mass donor and an elongated thick disk around the mass gainer. Multiplicity surveys conducted at the CHARA Array can reveal the frequency close companions around different populations of stars (DeFurio et al. 2022; Lanthermann et al. 2023).

Disks of gas and dust around young stars hold clues about the formation of planetary systems. Observations at radio wavelengths with facilities like the Atacama Large Millimeter/submillimeter Array (ALMA) yield exquisite images of the cooler, outer dust emission around young stars, while near-infrared interferometry probes the hotter, inner regions where terrestrial planet formation occurs. Figure 2 (bottom right) shows a CHARA image of the disk around the young, luminous star V1295 Aquilae that shows a ring-like structure with a central cavity where dust is destroyed and a bright asymmetry in the disk which appears to rotate between two images taken a few months apart (Ibrahim et al. 2023).

3. High Resolution Imaging of Photometrically Variable Targets

The CHARA Array can provide high resolution imaging of photometrically variable targets. A compelling example of the synergy between CHARA and AAVSO observations was the interferometric imaging (Kloppenborg et al. 2010, 2015) and photometric campaigns (Hopkins 2012; Kloppenborg, Hopkins, & Stencel 2012) to monitor the eclipse of epsilon Aurigae in 2009-2010. Epsilon Aurigae is a supergiant star that is eclipsed by a hidden companion every 27 years. The CHARA images directly confirmed the leading interpretation that the supergiant is eclipsed by a companion embedded in an opaque disk (Fig. 3, top row).

The CHARA Array can resolve the early structure of the expanding fireball stage during thermonuclear novae explosions. Nova Del 2013 was discovered by Koichi Itagaki on UT 14 August 2013 (Nakano et al. 2013). The CHARA Array began an intensive campaign to measure the size of the expanding fireball starting within 24 hours of the detonation (Schaefer et al. 2014). The angular expansion was measured as the outburst rose to peak brightness, and observations continued with extensive time coverage during the first 43 days. Changes in the apparent expansion rate (Fig. 3, middle row) can be explained by changes in the optical depth of the expanding ejecta as the material cools as it expands. The jump in the apparent angular size at later times coincides with an upturn in the near-infrared photometry compared with the visual light curve from AAVSO, suggesting that dust may have formed in the outermost layers. A slight elongation in the reconstructed images is detected as early as the first few days. A comparison of the angular expansion rate with the radial velocity of the outflow yields a distance to the nova of 4.5 kpc.

The cool hypergiant RW Cephei recently went through a great dimming episode initially reported by Vollmann & Sigismondi (2022) and monitored photometrically by AAVSO observers and the Kamogata/Kiso/Kyoto Widefield Survey (KWS; Maehara 2014). The reconstructed images of RW Cephei from the CHARA Array show a striking asymmetry in the disk illumination with a bright patch offset from the center and a darker zone to the west (Fig. 3, bottom row; Anugu et al. 2023), suggesting that the star's dimming is the result of a recent surface mass ejection event that created a dust cloud that partially blocks the stellar photosphere, similar to the interpretation of the great dimming of Betelgeuse (Dupree et al. 2022).

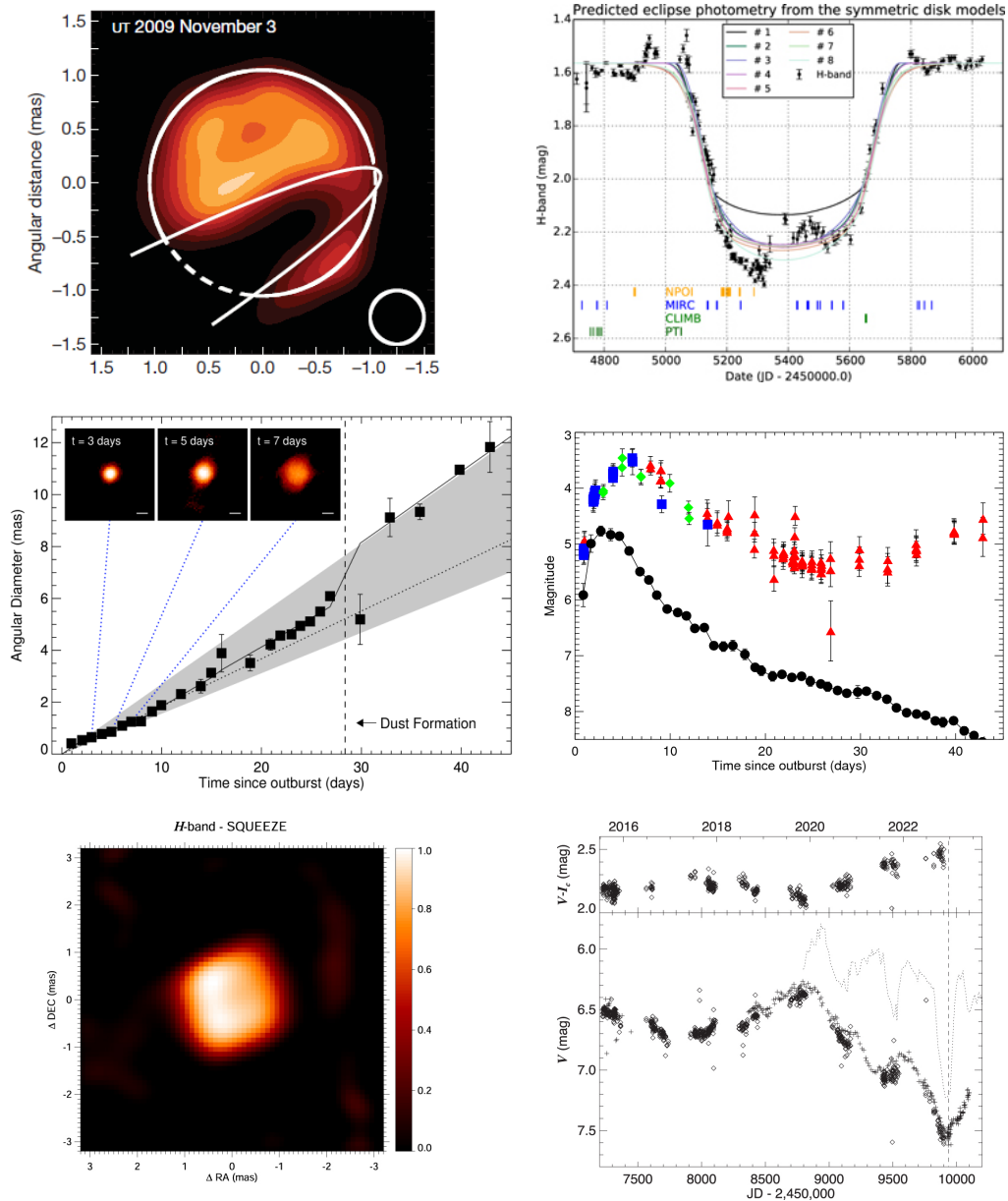


Figure 3. CHARA images (left) and AAVSO light curves (right) of time variable objects. Top row: Epsilon Aurigae in 2009 showing the supergiant star eclipsed by the opaque disk that enshrouds the companion (Kloppenborg et al. 2010, 2015). Middle row: Angular expansion and images of Nova Del 2013 (Schaefer et al. 2014). The light curve shows V-band photometry from AAVSO (black circles) and near-infrared photometry in the H and K-bands from CHARA (blue squares, green diamonds, red triangles). Bottom row: Great dimming of the cool hypergiant star RW Cepheii (Anugu et al. 2023).

4. Opportunities for Collaboration between CHARA and AAVSO

In collaboration with AAVSO Executive Director Brian Kloppenborg, CHARA began offering an opportunity during the 2023B Call for Proposals at the CHARA Array to foster collaborations

between AAVSO and CHARA observers to coordinate photometric observing campaigns on selected targets. Interest in participating in the program can be indicated on the CHARA observing proposal form. As a result of this effort, two AAVSO/CHARA observing campaigns will be initiated during the 2023B semester. Our goal is to build lasting collaborations between AAVSO observers and CHARA scientists by providing valuable photometric monitoring to complement CHARA's high resolution imaging.

Acknowledgements

This work is based upon observations obtained with the Georgia State University Center for High Angular Resolution Astronomy Array at Mount Wilson Observatory. The CHARA Array is supported by the National Science Foundation under Grant No. AST-1636624 and AST-2034336. Institutional support has been provided from the GSU College of Arts and Sciences and the GSU Office of the Vice President for Research and Economic Development. We acknowledge with thanks the variable star observations from the AAVSO International Database contributed by observers worldwide and used in this research.

References

- AAVSO. 2023, Observations from the AAVSO International Database (<http://www.aavso.org>).
- Anugu, N., Baron, F., Gies, D. R., et al. 2023, *AJ*, **166**, 78.
- Baines, E. K., Döllinger, M. P., Cusano, F., et al. 2010, *ApJ*, **710**, 1365.
- De Furio, M., Gardner, T., Monnier, J., et al. 2022, *ApJ*, **941**, 118.
- Dupree, A. K., Strassmeier, K. G., Calderwood, T., et al. 2022, *ApJ*, **936**, 18.
- Hopkins, J. L. 2012, *JAASO*, **40**, 633.
- Ibrahim, N., Monnier, J. D., Kraus, S. et al., 2023, *ApJ*, **947**, 68.
- Kloppenborg, B. K., Hopkins, J. L., & Stencel, R. E. 2012, *JAVSO*, **40**, 647.
- Kloppenborg, B. K., Stencel, R. E., Monnier, J. D., et al. 2010, *Nature*, **464**, 870.
- Kloppenborg, B. K., Stencel, R. E., Monnier, J. D., et al. 2015, *ApJS*, **220**, 14.
- Lanthermann, C., Le Bouquin, J. -B., Sana, H., et al. 2023, *A&A*, **672**, 6.
- Lawson, P. (ed.), 2000, *Principles of Long Baseline Stellar Interferometry* (JPL, Pasadena; <https://ecommons.cornell.edu/items/8892b20f-eeb0-4dae-a845-ab1c53a31d19>).
- Lester, K. V., Schaefer, G. H., Fekel, F. C., et al. 2022, *AJ*, **164**, 228.
- Maehara, H. 2014, *J. Space Science Informatics Japan*, **3**, 119.
- Mérand, A., Kervella, P., Breielfelder, J., et al. 2015, *A&A*, **584**, 80.
- Monnier, J. 2003, *Reports on Progress in Physics*, **66**, 789.
- Nakano, S., Itagaki, K., Denisenko, D., et al. 2013, *Central Bureau Electronic Telegrams*, **3628**, 1.
- Norris, R. P., Baron, F. R., Monnier, J, et al. 2021, *ApJ*, **919**, 124.
- Roettenbacher, R. M., Monnier, J. D., Korhonen, H., et al. 2016, *Nature*, **533**, 217.
- Schaefer, G. H., ten Brummelaar, T., Gies, D. R., et al. 2014, *Nature*, **515**, 234.
- ten Brummelaar, T. A., McAlister, H. A., Ridgway, S. T., et al. 2005, *ApJ*, **628**, 453.

Vollmann, W., & Sigismondi, C. 2022, *Astronomer's Telegram*, **15800**, 1.

von Braun, K. & Boyajian, T. 2017, *Extrasolar Planets and Their Host Stars* (Springer).

Zhao, M., Gies, D., Monnier, J. D., et al. 2008, *ApJ*, **684**, 95.

Analysis of the Blazhko Effect in the Star EY UMa

Emily Watson, Dr. Matthew Craig, Tanner Weyer, and Abigale Moen

Department of Physics and Astronomy, Minnesota State University Moorhead, 1104 7th Ave S,
Moorhead, MN 56563, USA; emily.watson@go.mnstate.edu

Subject Keywords

RR Lyrae variables; Blazhko effect; stars: individual (EY UMa)

Abstract

This study involved looking at an RR Lyrae star in Ursa Major, EY UMa. This star has long-term variability due to the Blazhko effect as well as the short-term variability characteristic of RR Lyrae stars. This project aims to better measure the short-term period of EY UMa and the longer-term period of the Blazhko effect. A Lomb-Scargle periodogram was used to measure the period and based on preliminary analysis of a subset of the data, the short-term period is 0.549 days. The calculated value of the short-term period is in line with the period given in VSX.

Throughout current analysis a few potential Blazhko frequencies were determined, 0.308/day, 0.017/day, and 0.1211/day, with corresponding periods of 32.5 days, 58.82 days, and 82.569 days, respectively. More analysis is needed to determine an accurate Blazhko period.

1. Introduction

Almost every year since 2012, the star EY UMa has been observed using the Paul P. Feder observatory. Initially this was done to try to accurately determine its period, as it was not precisely measured at the time. Now there is a more accurately known period listed in the AAVSO Variable Star Index (VSX). In past students' research on this star, they noticed the Blazhko effect. This is an effect seen in RR Lyrae variables where a change in the amplitude of the oscillation occurs over time. At the time they estimated the Blazhko period to be approximately 90 days. The goal with this project was to see if we could more accurately determine the Blazhko period as well as the overall period of this star.

2. Methods

All data for this project were collected at the Paul P. Feder Observatory, which is at the Minnesota State University Moorhead Regional Science Center. The telescope is a 16" Cassegrain and the current camera 2018 to present is an Andor Apogee Aspen CG16M. From 2011-2017 the camera was an Apogee Alta U9. All the analyzed data were taken in the Sloan r filter.

The data analyzed were calibrated using flat, dark, and bias images using standard calibration techniques using the package `ccdproc`¹ (Craig 2023). Aperture photometry was done using the `photutils`² package (Bradley 2023).

A Lomb-Scargle periodogram was used to analyze the data. Lomb-Scargle is an algorithm used for detecting periodic signals in unevenly sampled data (Lomb 1976; Scargle 1982).

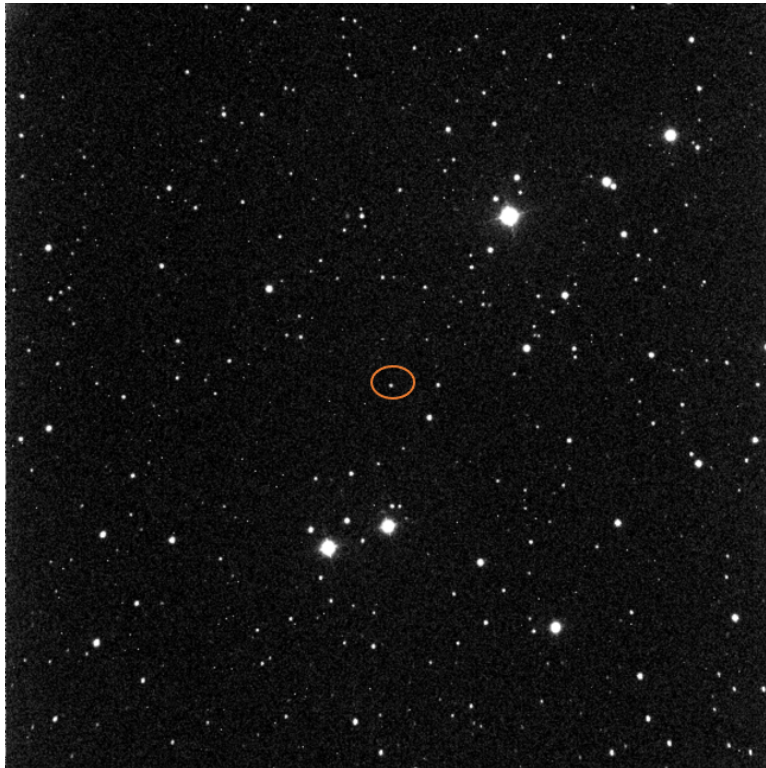


Image 1. Above is an image taken at the Paul P. Feder observatory, showing the starfield with EY UMa (circle). The field is located at: RA: $09^h 02^m 20.76^s$, Dec: $+49:49':09.2''$. The size of the field is 38.6×38.5 arcmin.

3. Results

In the Lomb-Scargle periodogram in Figure 1, a sine wave that best fits the frequency of EY UMa will have the highest peak, indicated by the orange dashed line. VSX stated that the current known period is 0.54909 days, which is close to our calculated value of 0.54907 days.

In the phase diagram in Figure 1, the model (solid line) fits the data reasonably well except near the minimum and maximum, where there is a lot of scattering. This is indicative of the Blazhko effect. In the residuals we saw variation, so we decided to try looking at a more complex model.

¹ `ccdproc.readthedocs.io`

² `photutils.readthedocs.io`

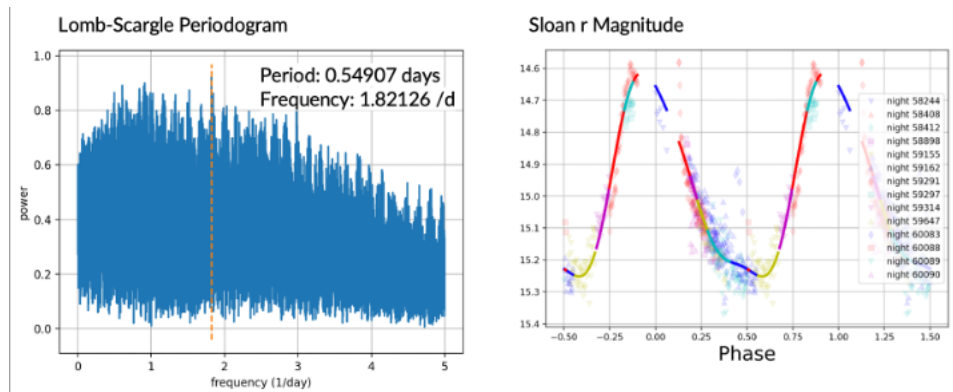


Figure 1. On the left is a Lomb-Scargle periodogram; the Y axis is normalized so that a perfect fit of a pure sine wave would have a power of 1. On the right is a phase diagram, with individual measurements as points and a fit with the primary frequency found in the periodogram along with the next two harmonics as lines. Data are color-coded by the night of observation.

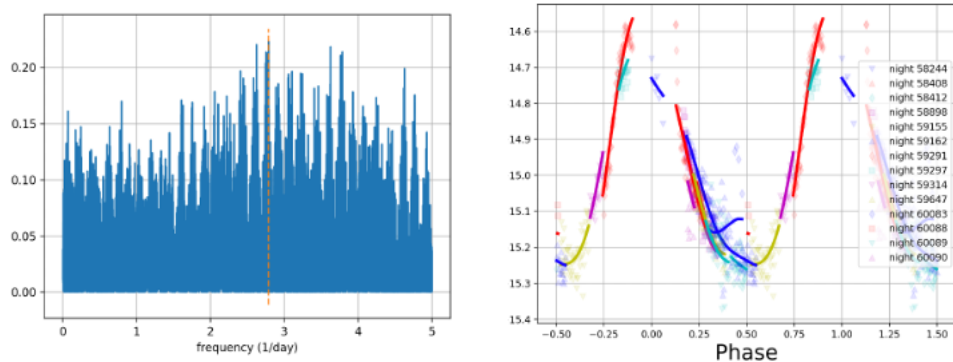


Figure 2. On the left is the Lomb-Scargle periodogram of the residual, normalized as in Figure 1. On the right is the corresponding phase plot as in Figure 1. In this case, the model includes several different frequencies, each determined by finding the maximum of the periodogram of the residuals.

A more complex model is shown in Figure 2. In that case, we found the residual by taking the difference between the model and the data. The periodogram of this residual is shown on the left. The highest peak was found again, a new residual calculated, and the process repeated a few times to get the phase plot on the right. Visually, this does a better job of fitting the data.

This method provided further evidence that multiple frequencies are needed to accurately plot the data. This led us to continue looking for the Blazhko effect.

One way to determine the Blazhko frequency is to look for peaks in the periodogram of the residual near the primary peak (Kaneshiro 2021), which is shown in Figure 3. The first high peak near the primary frequency is indicated by the green lines. The Blazhko frequency is the difference between the primary peak and the nearby peak, about 0.03/day. A model that includes these two frequencies (the primary frequency ± 0.03 /day) is shown in Figure 3. This model, like

the previous multi-frequency model, also more accurately fits the minima and maxima of the peaks than the primary frequency plus its harmonics.

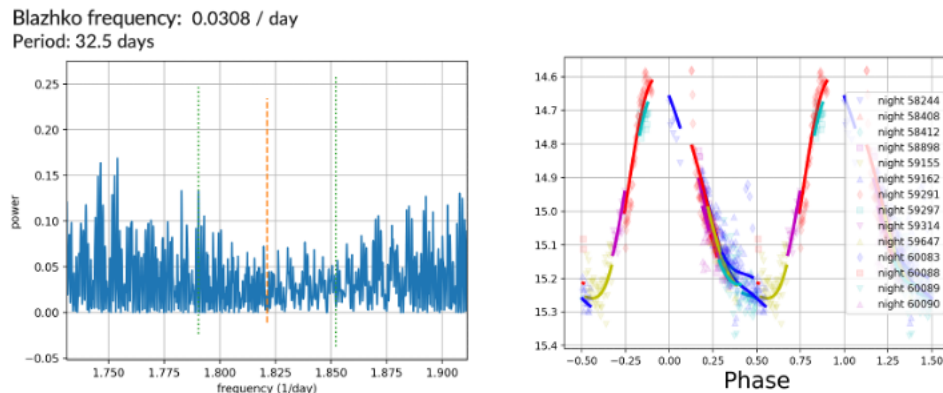


Figure 3. On the left, periodogram of the residual near the primary frequency, which is indicated by the dashed vertical line. The nearest tall peak to the primary frequency is indicated with the dotted vertical lines. On the right, a phase diagram that includes the primary frequency and the two additional frequencies indicated in the periodogram.

To verify whether this Blazhko period was correct, the region near twice the primary frequency was examined to see if the same side peaks were seen as around the primary frequency. As seen in Figure 4, the side peaks near twice the primary frequency correspond to a Blazhko frequency of 0.017/day, significantly different than near the primary frequency. Neither of these is close to the frequency of 0.011/day, which corresponds to the Blazhko period reported by previous students.

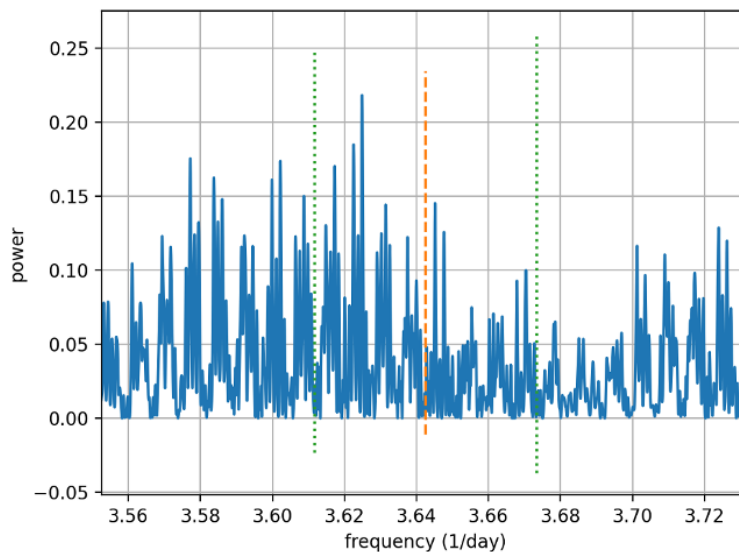


Figure 4. On the left, the periodogram of the residual after removing the primary frequency, in the vicinity of the twice the primary frequency, which is indicated by the vertical dash line. The green dotted lines show where peaks were expected based on the region around the primary frequency. Here, the clearest side peak is near 3.625/day, which gives a Blazhko frequency of 0.017/day.

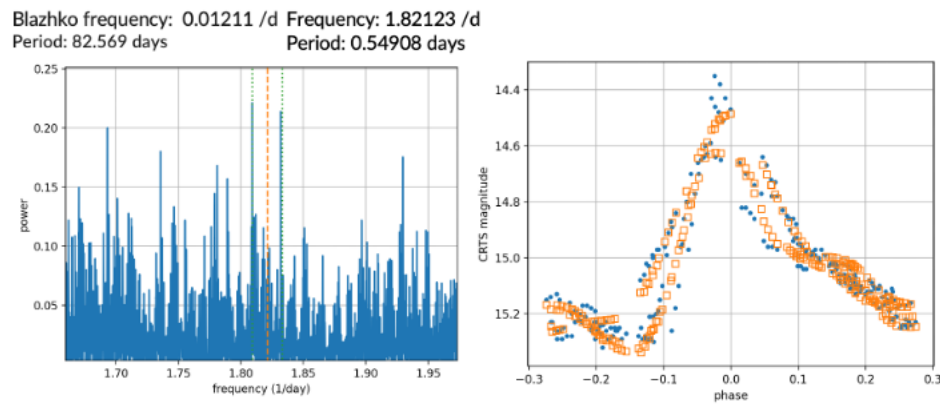


Figure 5. On the left is the periodogram of the CRTS data, having taken out the primary frequency, which is indicated by the vertical dashed line. The vertical dotted lines mark two distinct peaks close to the primary frequency to give that Blazhko frequency of 0.01211/day. On the right is a phase plot; the yellow boxes are the model, and the blue dots are the data.

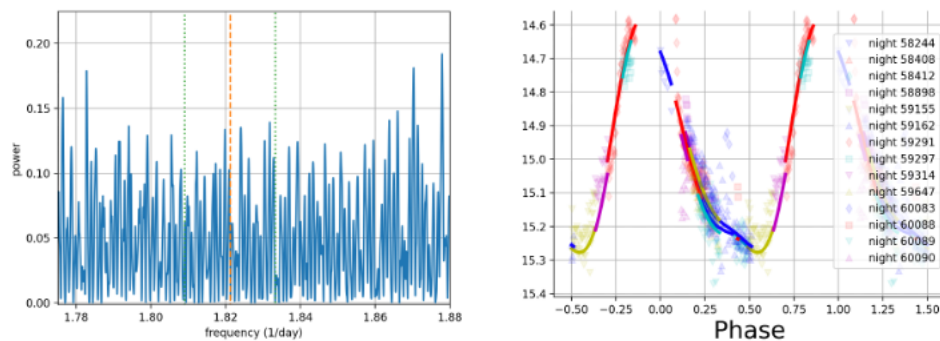


Figure 6. On the left is the periodogram of the residual after the CRTS primary frequency, marked in yellow, is removed from our data. The green dotted lines marks where the CRTS data had Blazhko peaks. On the right is a phase plot of the Paul P. Feder data and a model composed of the frequencies identified in the CRTS data.

As a cross-check, data from the Catalina Real Time Transient Survey (CRTS)(Drake, et. al. 2009) for EY UMa were downloaded and analyzed, as shown in Figure 5. The CRTS periodogram clearly has a Blazhko frequency of 0.01211/day. When the marked frequencies are included in a model, the fit to the CRTS data is reasonably good.

Finally, we then decided to take the primary and Blazhko frequencies found in the CRTS data and fit a model with those frequencies to the Feder data. Below, in Figure 6, are the results of that. The frequencies identified in the CRTS data are not present in the periodogram of our data. This phase plot includes a model with the CRTS frequencies fit to our data. It does not fit as well as the model constructed in Figure 3, which had a Blazhko frequency of 0.0308/day.

4. Conclusions

While it is clear that EY UMa exhibits the Blazhko effect, it is not clear what the Blazhko frequency is. There are two potential frequencies in the Feder data, 0.308/day and 0.017/day, corresponding to periods of 32.5 days and 58.82 days. In the CRTS data there is a clear Blazhko frequency of 0.1211/day, corresponding to a period of 82.569 days.

In the next steps of this analysis, the Feder data from 2011-2017 will be analyzed, along with Zwicky Transient Facility (ZTF) and CRTS data available on EY UMa. A joint analysis of those data sets may yield a more accurate model than can be obtained by analyzing each data source separately.

Acknowledgements

We acknowledge with thanks the Catalina Real-time Transient Survey for providing data for this project. We would like to acknowledge that the work of the three student authors was supported by the Strong Endowment at Minnesota State University Moorhead. Along with this, we would like to acknowledge Dr. Matthew Craig for both his guidance throughout this project and his stellar puns.

References

- Bradley, L; Brigitta Sipőcz, Thomas Robitaille, Erik Tollerud, Zé Vinícius, Christoph Deil, Kyle Barbary, Tom J Wilson, Ivo Busko, Axel Donath, Hans Moritz Günther, Mihai Cara, P. L. Lim, Sebastian Meßlinger, Simon Conseil, Zach Burnett, Azalee Bostroem, Michael Droettboom, E. M. Bray and Iskren Y. Georgiev. 2023, astropy/photutils: 1.10.0 (1.10.0). Zenodo.
<https://doi.org/10.5281/zenodo.1035865>
- Craig, M., Crawford, Michael Seifert, Thomas Robitaille, Brigitta Sipőcz, Josh Walawender, Steve Crawford, Zé Vinícius, Joe Philip Ninan, Michael Droettboom, Timothy Ellsworth Bowers, Jiyong Youn, Yash Gondhalekar, Erik Tollerud, P. L. Lim, E. M. Bray, Yoonsoo P. Bach, VSN Reddy Janga, and Benjamin Weiner. 2023, astropy/ccdproc: 2.4.1 (2.4.1). Zenodo.
<https://doi.org/10.5281/zenodo.7986923>
- Drake, A.J., et al., First Results from the Catalina Real-time Transient Survey. 2009, ApJ, 696, 870
- Lomb, N.R., Least-squares frequency analysis of unequally spaced data. 1976, Ap&SS 39, pp. 447-462
- Kaneshiro, D., Smith, H., and Samolyk, G., "An Update on the Periods and Period Changes of the Blazhko RR Lyrae Star XZ Cygni." 2021, JAAVSO, 49, 19
- Scargle, J. D. Studies in astronomical time series analysis. II - Statistical aspects of spectral analysis of unevenly spaced data. 1982, ApJ, 263, 835
- Stellarphot: <https://github.com/feder-observatory/stellarphot>

An Unfortunately Constant Star Field

Tanner Weyer, Dr. Matthew Craig, Mara DeRung, Emily Watson, Abigale Moen

Minnesota State University Moorhead, 600 11th St, Moorhead, MN 56563, USA;
tanner.weyer@go.mnstate.edu

Subject Keywords

AAVSO International Database; Photometry, CCD; Variable Stars

Abstract

During the spring of 2022 a star field in the constellation Boötes was found by researchers at MSUM that had no known variable stars in it. The following year more observations of the field were conducted in the hopes of finding and classifying variable stars in the field.

1. Introduction

In the spring of 2022, one of the authors was performing observations of a possible exoplanet transit for NASA's TESS mission when upon analysis of the data it was found that there were no known variable stars in the field of view. Center of the field is located at: RA: 13h 41m 57.008s, Dec: +17:17':59.971" and the size of the field is 38.6 x 38.5 arcmin. This raised interest in the field thus during the first half of 2023 the field was observed again totaling 8 nights. The follow-up observations of the field were plagued by various limiting factors such as large amounts of wildfire smoke and a physical bug becoming trapped in the telescope and obscuring a substantial portion of the sensor.



Figure 1. An image of the star field in question taken with the Paul P. Feder observatory. Center of the field located at: RA: 13^h 41^m 57.008^s, Dec: +17:17':59.971". Size of the field 38.6 x 38.5 arcmin.

2. Methods

Data were collected at Paul P. Feder Observatory at the Minnesota State University Moorhead Regional Science Center. The telescope is a 16" Cassegrain manufactured by DFM Engineering, with an Andor Alta CG16-M camera and photometric filters. All observations were done in a single filter, Sloan r, because the filter wheel was not functioning at the time.

Table 1. A list of the nights of data collected as well as noting if they were used and any issues with the night of data.

Night (YYYY-MM-DD)	Data Used	Issues
2022-03-09	Yes	None
2023-05-19	Yes	Smoke
2023-05-24	Yes	Smoke
2023-05-25	Yes	Smoke
2023-05-26	Yes	Smoke
2023-05-27	No	Dome Tracking
2023-05-30	Yes	Smoke
2023-06-12	No	Smoke/Bug
2023-06-13	No	Smoke/Bug
2023-06-18	No	Smoke/Bug

The data were calibrated utilizing dark, bias, and flat images using standard techniques with the package `ccdproc`¹ and then aperture photometry was performed using the package `photutils`². An ensemble differential magnitude and relative flux were calculated for each star initially. Stars identified as potentially variable also had a magnitude calculated using the AAVSO's comp/check star method, with comp and check stars chosen from the APASS catalog to have color and magnitude close to the potential variable. The data analysis presented several challenges as the nights of observation encountered several complications such as a large caddisfly becoming trapped in the telescope and obscuring a portion of the sensor. Another complication in this project was the unrelenting wildfire smoke that plagued the observatory during the majority of 2023.

Table 2. A list of the stars that all had very similar variability. The star ID is the internal ID that was used to designate them.

Star ID	RA	Dec
128	205.6321	17.12796
165	205.4529	17.56083
271	205.2699	17.40231
303	205.3445	17.03791
326	205.2925	17.12691
333	205.2766	17.11588

¹ `ccdproc.readthedocs.io`

² `photutil.readthedocs.io`

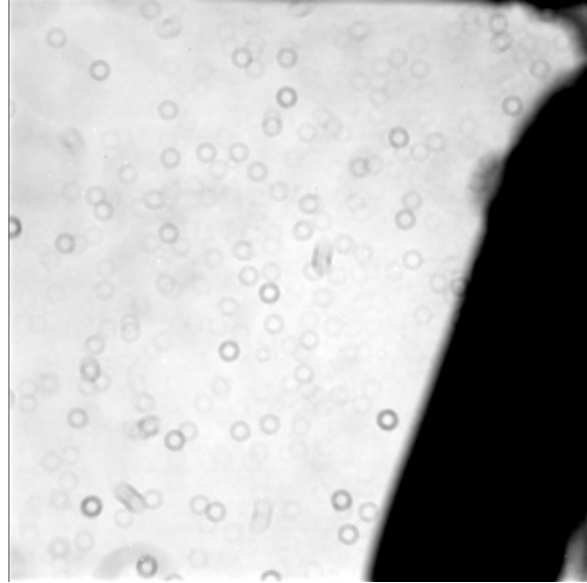


Figure 2. A flat image taken during the nights in which the Caddisfly was present in the optical train. As seen here the fly obstructed an appreciable portion of the sensor.

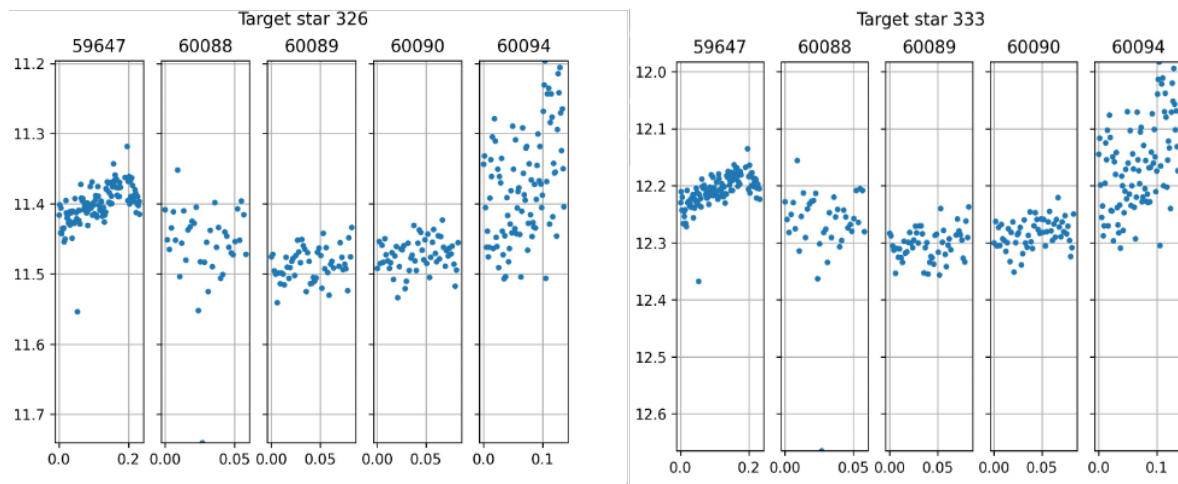


Figure 3. Pictured are two of the stars in which the variability resembled several other stars in the field. The magnitude was calculated using the AAVSO's method of one comparison and one check star and each segment of the graph represents a different night spread across 2022 and 2023.

3. Conclusions and Next Steps

As of time of writing there is not any confirmed variable stars in the field and the current data set from the Paul P. Feder observatory has not yielded concrete results, but the current plan is to continue observing the field during 2024 and continue work on the project. Along with more data from our own observatory, the search for variable stars from all-sky survey archives will also continue and be used to back up any findings from our observations. The data obtained during

2023 provided some possible candidates but due to the large impact of the wildfire smoke and the bug the confidence in the findings of that data was greatly diminished.

Acknowledgements

We acknowledge with thanks the Catalina Real-time Transient Survey as well as the All-Sky Automated Survey for Supernovae (ASAS-SN) for providing data for this project. We would also like to acknowledge that the work of the four student authors was supported by the Strong Endowment at Minnesota State University Moorhead. Also, we would like to acknowledge Dr. Matthew Craig for his great leadership and advising skills in helping to guide us through this project.

References

- Drake, A.J. et al. 2009, First Results from the Catalina Real-time Transient Survey, *ApJ*, 696, 870
- Astropy Collaboration. 2022, “The Astropy Project: Sustaining and Growing a Community-oriented Open-source Project and the Latest Major Release (v5.0) of the Core Package”, *ApJ*, 935, 167, doi:10.3847/1538-4357/ac7c74
- Masci, F. J., Laher, R. R., Rusholme, B., et al. 2018, The Zwicky Transient Facility: Data Processing, Products, and Archive, *PASP*, 131, 995
- Stellarphot: <https://github.com/feder-observatory/stellarphot>
- ccdproc: <https://github.com/astropy/ccdproc>
- photutils: <https://github.com/astropy/photutils>